RESEARCH ACTIVITIES IX
Laser Research Center for Molecular Science

IX-A Developments and Researches of New Laser Materials

Although development of lasers is remarkable, there are no lasers which lase in ultraviolet and far infrared regions. However, it is expected that these kinds of lasers break out a great revolution in not only the molecular science but also in the industrial world.

In this project we research characters of new materials for ultraviolet and far infrared lasers, and develop new lasers by using these laser materials.

IX-A-1 Terahertz Radiation Mechanism from Femtosecond-Laser-Irradiated InAs (100) Surface

TAKAHASHI, Hiroshi[1]; QUEMA, Alex; GOTO, Masahiro; ONO, Shingo; SARUKURA, Nobuhiko
([1]GUAS)

[*Jpn. J. Appl. Phys.* **42**, L1259 (2003)]

Terahertz (THz) radiation mechanism from femtosecond-laser-irradiated InAs surface is investigated by measuring the excitation-fluence dependence of THz-radiation power. It is found that the THz-radiation is mainly generated by the surge-current, which originates from the different diffusion velocities between photo-excited electrons and holes. Furthermore, it is also found that the excitation fluence dependence of THz-radiation is categorized into two regions depending on the excitation fluence. At low excitation fluence, a quadratic-dependent enhancement of the THz-radiation power is observed with increasing excitation fluence. In contrast, at high excitation fluence, the enhancement factor is gradually reduced, and the radiation power becomes proportional to a logarithm function of the excitation fluence. These results are explained by considering the photo-Dember field as the THz-radiation source.

IX-A-2 Broadband Terahertz Radiation Emitter Using Femtosecond-Laser-Irradiated *n*-Type InAs under Magnetic Field

TAKAHASHI, Hiroshi[1]; HASSELBECK, Michael[2]; QUEMA, Alex; GOTO, Masahiro; ONO, Shingo; SARUKURA, Nobuhiko
([1]GUAS; [2]Univ. New Mexico)

[*Jpn. J. Appl. Phys.* **43**, L221 (2004)]

We present the generation of broadband terahertz (THz) radiation using *n*-type InAs irradiated by ultrafast laser pulses. It is found that the high-frequency component of the THz-radiation spectrum originates from the hybrid modes of the plasmons and the longitudinal optical (LO) phonons, whose peak frequency shifts toward higher frequency with increasing doping density. For *n*-type InAs with a doping density of 3.1×10^{17} cm^{-3}, the high-frequency components of THz-radiation spectrum are observed at around 5.5 and 9 THz. Furthermore, the enhancement of THz-radiation power from these hybrid modes is achieved by applying an external magnetic field.

IX-A-3 Teflon Photonic Crystal Fiber as Terahertz Waveguide

GOTO, Masahiro; QUEMA, Alex; TAKAHASHI, Hiroshi; ONO, Shingo; SARUKURA, Nobuhiko

[*Jpn. J. Appl. Phys.* **43**, L317 (2004)]

We demonstrate the construction of reasonably long and non-polarization changing photonic fiber waveguide using Teflon which is a readily available and highly flexible material. Due to its relatively low loss coefficient, the possibility of preparing longer photonic fiber waveguide,which has the potential of guiding intense THz radiation, can be easily attained.

IX-A-4 Growth and Charge Transfer Luminescence of Yb^{3+}-Doped $YAlO_3$ Single Crystals

SHIM, Jan Bo[1]; YOSHIKAWA, Akira[1]; FUKUDA, Tsuguo[1]; PEJCHAL, J.[2]; NIKL, M.[2]; SARUKURA, Nobuhiko; YOON, D. H.[3]
([1]Tohoku Univ.; [2]Inst. Phys. ASCR; [3]Sungkyunkwan Univ.)

[*J. Appl. Phys.* **95**, 3063 (2004)]

Yb^{3+}-doped $YAlO_3$ single crystals have been grown by the Czochralski method with a radio-frequency heating system. Starting melt compositions of $Y_{1-x}Yb_xAlO_3$ were varied with x = 0.02, 0.1, 0.2, 0.3, and 0.45. The best Yb^{3+}-doped $YAlO_3$ single crystals were obtained for a growth rate of 1.0 mm/h. The grown crystals were transparent and almost colorless. To investigate the homogeneity, the effective segregation coefficient of the Yb ion was estimated. The absorption, photoluminescence, and luminescence decay kinetics of Yb^{3+}-doped $YAlO_3$ were investigated for the temperature range 4–300 K. Very fast charge transfer luminescence of Yb^{3+} from the near ultraviolet to visible spectral range and the high density of the Yb-rich $YAlO_3$ makes this material a promising candidate for fast scintillators.

IX-A-5 Terahertz Radiation from InAs with Various Surface Orientations under Magnetic Field Irradiated with Femtosecond Optical Pulses at Different Wavelengths

TAKAHASHI, Hiroshi[1]; SAKAI, Masahiro; QUEMA, Alex; ONO, Shingo; SARUKURA, Nobuhiko; NISHIJIMA, Gen[2]; WATANABE, Kazuo[2]
([1]GUAS; [2]Tohoku Univ.)

[*J. Appl. Phys.* **95**, 4545 (2004)]

We present the magnetic-field dependence of terahertz (THz)-radiation power from femtosecond-laser-irradiated InAs with various surface orientations. Under 800 nm optical excitation, the magnetic field that provides the maximum THz-radiation power is found to be affected by the surface orientation, and InAs(111) exhibits it at lower magnetic fields than that of the other surfaces. In contrast, under 1560 nm excitation, the dependence on the surface orientation almost disappeared, and saturation is observed at a much smaller magnetic field than that in the 800 nm excitation case. Additionally, from the results of magnetic-field dependence up to 14 T, the shift of the peak in the THz-radiation spectrum toward lower frequency is confirmed, depending on the magnetic field applied, which is possibly induced by the emergence of a magneto-plasma effect.

IX-A-6 Optical, Infrared and EPR Spectroscopy of CaF_2:Ce^{3+} Crystals Co-Doped with Li^+ or Na^+

YAMAGA, Mitsuo[1]; YABASHI, Satoshi[1]; MASUI, Yuki[1]; TAKAHASHI, Hiroshi; SAKAI, Masahiro; SARUKURA, Nobuhiko; WELLS, J. -P. R.[2]; JONES, G. D.[3]
([1]Gifu Univ.; [2]Univ. Sheffield; [3]Univ. Canterbary)

[*J. Lumin.* **108**, 307 (2004)]

Interconfigurational 4f ↔ 5d VUV absorption and luminescence, intra-4f[1] IR absorption and X-band EPR measurements have been carried out on CaF_2:Ce^{3+} crystals co-doped with Na^+ and Li^+ ions. For both Li^+ and Na^+ co-doping, cubic, new tetragonal and rhombic-symmetry centres are observed. Cubic centres, which are readily observable by their infrared transitions, could not be identified and remain elusive in the EPR spectra.

IX-A-7 Effect of Ultrafast Optical Pulses with Different Pulse Duration on the Terahertz Radiation Spectrum of *n*-Type InAs

TAKAHASHI, Hiroshi[1]; HASSELBECK, Michael[2]; QUEMA, Alex; GOTO, Masahiro; ONO, Shingo; SARUKURA, Nobuhiko
([1]GUAS; [2]Univ. New Mexico)

[*Jpn. J. Appl. Phys.* **43**, L746 (2004)]

Terahertz (THz) radiation from *n*-type InAs irradiated by ultrafast laser pulses is investigated under the existence of the magnetic field. It is found that the high-frequency component of the THz-radiation spectrum originates from the hybrid modes of the plasmons and the longitudinal optical (LO) phonons, and its intensity can be drastically enhanced by using the laser pulses with duration shorter than the oscillation period of the hybrid modes. Additionally, it is also found that the ratio of THz-radiation power from these two modes can be controlled by adjusting the pulse duration and the magnetic field strength.

IX-A-8 Physical Origin of Magnetically Induced Periodic Structure Observed in Terahertz Radiation Spectrum Emitted from InAs

TAKAHASHI, Hiroshi[1]; QUEMA, Alex; GOTO, Masahiro; ONO, Shingo; SARUKURA, Nobuhiko; NISHIJIMA, Gen[2]; WATANABE, Kazuo[2]
([1]GUAS; [2]Tohoku Univ.)

[*Jpn. J. Appl. Phys.* **43**, L1017 (2004)]

Terahertz (THz) radiation from femtosecond-laser-irradiated InAs(100) surface is investigated. It is found that THz-radiation spectrum exhibits two inter-related phenomena in a strong magnetic field under the Voigt configuration. The peak shift of THz-radiation spectrum toward lower frequency is observed with increasing magnetic field. Additionally, THz-radiation spectrum is found to posses a periodic structure owing to the interference of THz-radiation pulses from the front and back surfaces of the InAs substrate. The physical origin of the latter phenomenon is discussed by considering the magneto-plasma effect, which affects both real and imaginary parts of refractive index for THz-radiation propagating in a direction perpendicular to the magnetic field.

IX-A-9 Design Proposal of Light Emitting Diode in Vacuum Ultraviolet Based on Perovskite-Like Fluoride Crystals

OUENZERFI, El Riadh[1]; ONO, Shingo; QUEMA, Alex; GOTO, Masahiro; SARUKURA, Nobuhiko; NISHIMATSU, Takeshi[1]; TERAKUBO, Noriaki[1]; MIZUSEKI, Hiroshi[1]; KAWAZOE, Yoshiyuki[1]; YOSHIKAWA, Akira[1]; FUKUDA, Tsuguo[1]
([1]Tohoku Univ.)

[*Jpn. J. Appl. Phys.* **43**, L1140 (2004)]

The variation of band gap energy, band structure and lattice constant of mixed $LiBaF_3$, $LiCaF_3$ and $LiSrF_3$ perovskites is studied. The band structure and transition type of these fluorides is predicted by *ab initio* band calculation based on the local density approximation. The design principle of vacuum ultraviolet light emitting diode is proposed. The lattice-matched double-hetero structure of different perovskite-like fluorides is found to be sufficiently feasible to fabricate with direct-band-gap compounds $LiBa_xCa_ySr_{(1-x-y)}F_3$ on $LiSrF_3$.

IX-B Development and Research of Advanced Tunable Solid State Lasers

Diode-pumped solid-state lasers can provide excellent spatial mode quality and narrow linewidths. The high spectral power brightness of these lasers has allowed high efficiency frequency extension by nonlinear frequency conversion. Moreover, the availability of new and improved nonlinear optical crystals makes these techniques more practical. Additionally, quasi phase matching (QPM) is a new technique instead of conventional birefringent phase matching for compensating phase velocity dispersion in frequency conversion. These kinds of advanced tunable solid-state light sources, so to speak "Chroma Chip Lasers," will assist the research of molecular science.

In this projects we are developing Chroma Chip Lasers based on diode-pumped-microchip-solid-sate lasers and advanced nonlinear frequency conversion technique.

IX-B-1 Saturation Factors of Pump Absorption in Solid-State Lasers

SATO, Yoichi; TAIRA, Takunori

[*IEEE J. Quantum Electron.* **40**, 270–280 (2004)]

The precise formulation of the absorption coefficient is investigated, where the saturation factors of absorption for solid-state lasers are defined as depending on the pumping scheme. We also investigated theoretical and experimental evaluations of the pump saturation effect in Nd:YVO_4 as an example, and proved the accuracy of this model describing the saturation effect (Figure 1), and the clipping of this effect by laser oscillation (Figure 2). This paper points out the following: even in the case of 1 μm oscillation in neodymium lasers, the selection of pump wavelength results in not only the different absorption cross sections, but also the different characteristics in the saturation of the pump absorption. This influence is especially important in the laser media with a large cross section, such as Nd:YVO_4. For example, in the direct pumping into the emitting levels $^4F_{3/2}$, the electrons in the laser upper level also connect to the stimulated emission to the ground state, which should not be observed in the conventional pumping into $^4F_{5/2}$ because of little distribution of the electrons in the $^4F_{5/2}$.

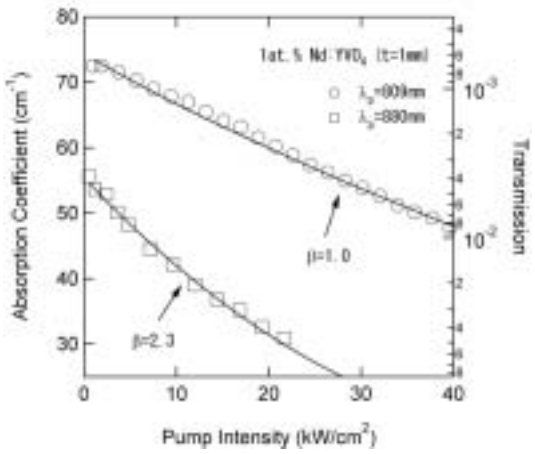

Figure 1. Absorption coefficient of 1 at.% Nd:YVO_4 in π-polarization as a function of pumping intensity.

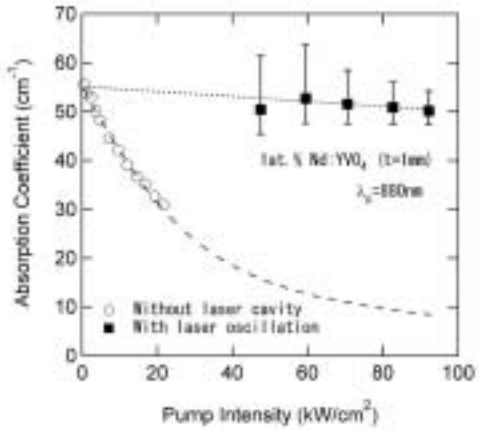

Figure 2. Absorption coefficient of 1 at.% Nd:YVO_4 in π-polarization under lasing condition.

IX-B-2 Spectroscopic Properties and Laser Operation of Nd:$Y_3ScAl_4O_{12}$ Polycrystalline Gain Media, Solid-Solution of Nd:$Y_3Al_5O_{12}$ and Nd:$Y_3Sc_2Al_3O_{12}$ Ceramics

SATO, Yoichi; SAIKAWA, Jiro; SHOJI, Ichiro; TAIRA, Takunori; IKESUE, Akio

[*J. Ceram. Soc. Jpn.* **112**, S313–S316 (2004)]

Transparent Nd^{3+}-doped $Y_3ScAl_4O_{12}$ (Nd:$Y_3ScAl_4O_{12}$) ceramics with up to 5.0-at.% Nd^{3+}-concentration (C_{Nd}) were fabricated by a solid-state reaction method using commercial 4N powders. Spectroscopic properties of this media, such as absorption and emission spectra, the fluorescence lifetime, and the influence of increasing C_{Nd} on these characteristics are discussed. It is shown that high absorption efficiency of the pump radiation that is necessary for efficient operation of a Nd:$Y_3ScAl_4O_{12}$ microchip laser can be obtained by increasing C_{Nd}. One-micron laser operation with 113-mW output power (7.7% optical-to-optical overall efficiency) and 9.6% slope efficiency was demonstrated from a 1.0-mm thick, 5.0-at.% Nd:$Y_3ScAl_4O_{12}$ uncoated sample under 808-nm pumping by a Ti:Sapphire laser (Figure 1). Further works are directed toward optimization of the fabricating process in order to reduce the optical losses that are found to increase with increasing C_{Nd}.

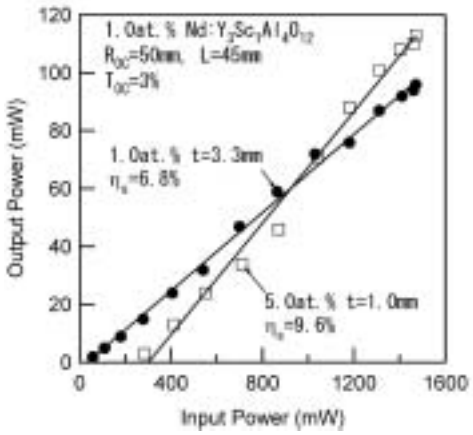

Figure 1. Output power versus pump power for the Nd:$Y_3Sc Al_4O_{12}$ ceramics with 1.0 and 5.0-at.% Nd under 808-nm Ti:Sapphire pumping.

IX-B-3 High Energy Optical Parametric Oscillation Using 3-mm-Thick Periodically Poled MgO:$LiNbO_3$

ISHIZUKI, Hideki; SHOJI, Ichiro; TAIRA, Takunori

[*Conf. Lasers Electro-Optics* CTuA3 (2004)]

We presented high energy optical parametric oscillation (OPO) using 3-mm-thcik periodically poled MgO:LN (PPMgLN) device. Multipulses of ~10 kV were applied to the crystal at elevated temperature of ~100 °C to fabricate the PPMgLN device.

For OPO experiments, a Q-switched Nd:YAG laser (Spectra-Physics, LAB-170-30) was used as a pump source. The repetition rate was 30 Hz with the pulse width of 15 ns. The cavity length of single resonant OPO was fixed to 35 mm. The $1/e^2$-diameter of pump beam was set to 2.2 mm. Figure 1 shows the dependence of OPO output energy on input pump energy. The pump threshold was ~3 mJ, and the slope efficiency was 51% for total output (signal of 1.82 μm, idler of 2.56 μm) and 28% for the signal wave only. The maximum total output energy of 22 mJ at the pump energy of 46 mJ was obtained without photorefractive damages. This is the highest energy obtained from QPM-OPO operation using a PPMgLN device even at room temperature. The large-aperture PPMgLN devices would enable us to realize high-energy wavelength conversion, short pulse amplification, and pulse compression.

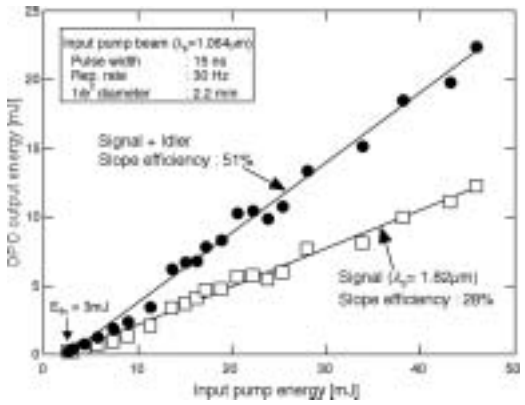

Figure 1. OPO output energy *vs.* input pump energy. Pump pulse width : 15 ns, Pump rep. rate : 30 Hz, Pump $1/e^2$-diameter : 2.2 mm.

IX-B-4 Basic Enhancement of the Overall Optical Efficiency of Intracavity Frequency-Doubling Devices for the One-Micron Continuous-Wave Nd:$Y_3Al_5O_{12}$ Laser Emission

LUPEI, Voicu[1]; PAVEL, Nicolaie[2]; TAIRA, Takunori
([1]IAP-NILPRP, Romania; [2]IMS and IAP-NILPRP, Romania)

[*Appl. Phys. Lett.* **83**, 3653 (2003)]

Frequency-doubling of the efficient one-micron $^4F_{3/2} \rightarrow {}^4I_{11/2}$ Nd^{3+} lasers is currently the most used method to obtain light into the green region. If the intracavity frequency-doubling method is considered, the laser active material and a nonlinear crystal designed for phase matching conditions are placed in a laser resonator that confines the beam at the fundamental frequency ω inside the resonator, passes it through the doubling crystal and out-couples the frequency-doubled 2ω beam. The second-harmonic (SH) power $P_{2\omega}$ is determined by the intracavity emission intensity of the active material $I_{\omega,\mathrm{int}}$ and by the characteristics of the doubling crystal

$$P_{2\omega} \sim I_{\omega,\mathrm{int}}^2 \cdot d_{eff}^2 \ell^2 / (n_1^2 n_2) \qquad (1)$$

where d_{eff} is the effective nonlinear coefficient along the phase matching direction, l is the length of the nonlinear crystal and n_1 and n_2 are the refractive indices at the fundamental and SH wavelengths, respectively. The overall optical-to-optical efficiency of such a laser, i.e. the output power $P_{2\omega}$ obtained for a given pump power $P^{(j)}$, where $j \equiv i$ denotes the pump power incident on the laser material and $j \equiv ab$ denotes the absorbed power, can be optimized acting on these factors. In this work we discuss the possibility of basic enhancement of the overall optical-to-optical efficiency of intracavity frequency-doubling devices for the one-micron continuous-wave Nd lasers by direct pumping into the emitting level and by using concentrated laser materials.

The continuous wave (CW) Nd lasers are usually pumped using the strong absorption Nd^{3+} lines to energy levels placed above the emitting level $^4F_{3/2}$ and the absorbed excitation relaxes to the emitting level through electron-phonon interactions. Thus, the upper

quantum defect between the pump level and the emitting level reduces the performances of the laser emission and contributes to the generation of heat. The upper quantum defect can be eliminated by pumping directly into the emitting level $^4F_{3/2}$: this modality of pumping was suggested in the first work on semiconductor diode excitation of Nd^{3+} emission[1] and it was used in the first diode laser pumped Nd:YAG both in transverse and end-pumped configurations.[2),3)] However, owing to the weak absorption into the level $^4F_{3/2}$ of Nd^{3+} in YAG, this was soon replaced by diode laser pumping at 808 nm into the strongly absorbing level $^4F_{5/2}$. The direct pumping of CW Nd lasers into the emitting level was reconsidered recently for Nd:YAG crystals and ceramics[4),5)] as well as for other laser materials, such as Nd:YVO_4[4),6)] or Nd:$GdCa_4O(BO_3)_3$.[7)]

A problem of concern in using the direct pumping into the emitting level is the low absorption η_a in some of the important laser materials, including Nd:YAG, for concentrations C_{Nd} around 1-at.% Nd that are traditionally used for construction of lasers. This could be overcome by using more concentrated materials. By estimating the quantum efficiency η_{qe} using the energy transfer data at low inversion, specific to the CW Nd:YAG lasers, it was shown that the product $\eta_a\eta_{qe}$ increases with C_{Nd} up to a critical value then decreases again.[5)] The range of CNd for which this product is larger than for 1-at.% Nd could be quite wide: up to 8.0-at.% for Nd:YAG and up to 3.0-at.% for Nd:YVO_4. Thus, working at the upper C_{Nd} limit would benefit both from a low threshold and from increased slope efficiency.

According to Eq. (1), the enhancement of the laser emission parameters at the frequency ω by direct pumping will be accentuated in the frequency-doubling device, resulting in a lower threshold for the SH emission and in a stronger dependence on the absorbed pump power. These concepts are investigated in this work by using 1.0-at.% and 2.4-at.% Nd:YAG crystals.

The frequency doubling is investigated with a V-type folded laser resonator (Figure 1). The 3-mm long Nd:YAG crystals were coated as anti-reflection for 1064 nm and high transmission for 808 and 885 nm. A Ti:Sapphire laser whose radiation was focused into the crystals in a spot of 50-μm diameter was used for pumping. The M1 to M2 resonator arm is 70-mm long and contains also a Brewster glass plate (BP) to polarize the beam. The length of the M2 to M3 frequency-doubling arm was 55 mm and houses a 10-mm long LBO nonlinear crystal designed for type I critical phase matching condition (θ = 90°, ϕ = 11.4°) at 25 °C.

The 532-nm output power for the 1.0-at.% Nd:YAG crystal is shown in Figure 2. The threshold of green radiation is greatly reduced at 885 compared to 808-nm pumping (26 and respectively 50 mW), while the dependence on the absorbed power is enhanced. Moreover, the emission under 808-nm pumping shows signs of saturation induced by thermal effects in Nd:YAG for green emission larger than ~14 mW. The 532-nm emission under 885-nm pumping does not show such behavior even at the 20 mW obtained for the available absorbed power. As indicated by Figure 3a, the use of a more concentrated (2.4-at.% Nd) active crystal improves the 885-nm pump absorption efficiency, but increases the emission threshold in absorbed power, without changing the slope efficiency. However, the SH power obtained with this sample for a given incident power is larger (Figure 3b). Further improvement could be obtained with a longer active laser crystal and/or a higher C_{Nd}.

In conclusion this work demonstrates the advantages of using direct pumping into the emitting level and of more concentrated laser materials in intracavity frequency-doubling devices based on the 1064-nm CW laser emission of Nd:YAG. The improvement of emission parameters is accompanied by a drastically reduction of generation of heat that could enable scaling to higher emission powers. This approach could be particularly important for laser materials with higher absorption cross-section for the direct pumping.

References

1) R. Newman, *J. Appl. Phys.* **34**, 437 (1963).
2) M. Ross, *Proc. IEEE* **56**, 196 (1968).
3) L. J. Rosenkrantz, *J. Appl. Phys.* **34**, 4603 (1972).
4) R. Lavi, S. Jackel, Y. Tzuk, M. Winik, E. Lebiush, M. Katz and I. Paiss, *Appl. Opt.* **38**, 7382 (1999).
5) V. Lupei, N. Pavel and T. Taira, *IEEE J. Quantum Electron.* **38**, 240 (2002).
6) V. Lupei, N. Pavel and T. Taira, *Opt. Commun.* **201**, 431 (2002).
7) V. Lupei, D. Vivien and G. Aka, *Appl. Phys. Lett.* **81**, 811 (2002).

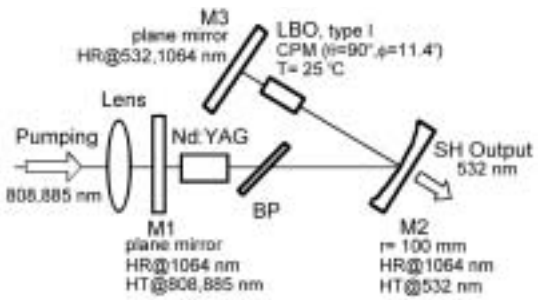

Figure 1. Schematic of the V-type resonator used in intracavity frequency-doubling experiments.

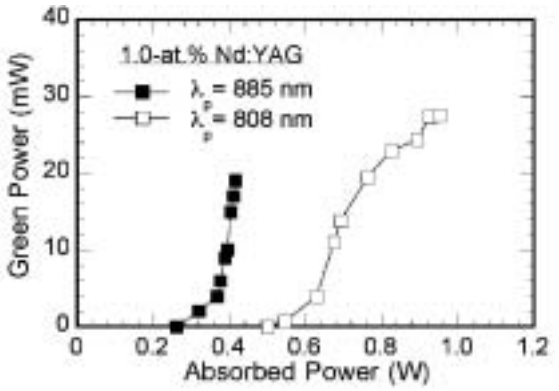

Figure 2. Green power *vs.* absorbed power for the 1.0-at.% Nd:YAG crystal under 808 and 885-nm pumping.

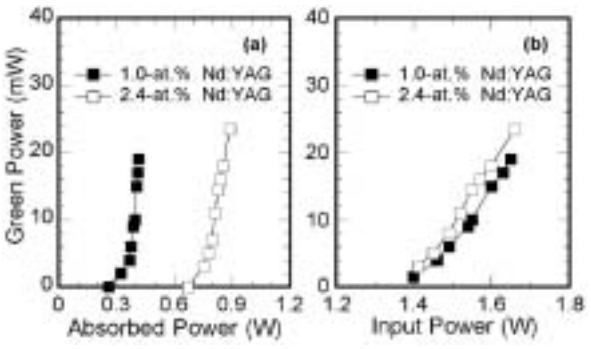

Figure 3. Green power for the 1.0 and 2.4-at.% Nd:YAG crystals under 885-nm pumping function of (a) absorbed, and (b) input power.

IX-B-5 High-Power Blue Generation from a Periodically Poled MgO:$LiNbO_3$ Ridge-Type Waveguide by Frequency Doubling of a Diode End-Pumped Nd:$Y_3Al_5O_{12}$ Laser

IWAI, Makato[1]; YOSHINO, Takeshi[1]; YAMAGUCHI, Shoichiro[1]; IMAEDA, Minoru[1]; PAVEL, Nicolaie[2]; SHOJI, Ichiro; TAIRA, Takunori

([1]NGK, Nagoya; [2]IMS and IAP-NILPRP, Romania)

[*Appl. Phys. Lett.* **83**, 3659 (2003)]

Continuous-wave (CW) blue laser radiation is of interest for various applications, such us display technologies, obtaining of high-density optical disk systems, high-resolution printing, or biological application. In order to obtain the blue light at 473 nm the second-harmonic generation (SHG) of the $^4F_{3/2} \rightarrow {}^4I_{9/2}$ transition at 946 nm of Nd^{3+}:$Y_3Al_5O_{12}$ (Nd:YAG) can be used. An attractive method to realize a compact blue-light source is SHG by quasi-phase matching (QPM) interaction: $LiNbO_3$ (LN), $LiTaO_3$ and $KTiOPO_4$ are in present widely known and used for fabricating of QPM devices. CW blue light at 473 nm of 81 mW was generated for a fundamental power of 1.13 W in a 15-mm-long periodically poled (PP) $LiNbO_3$ that operated at an elevated temperature of 140 °C.[1)] When using a PP $KTiOPO_4$ pumped at room temperature by a 946-nm Nd:YAG laser maximum blue power of 76 mW was obtained for 2.27 W of fundamental power.[2)]

Due to its high conversion efficiency, a waveguide-type QPM SHG device is a very promising solution for a compact blue-light source. The key points for obtaining efficient and high-power SHG waveguide devices include strong confinement of the fundamental light into the waveguide, good overlap of fundamental and second-harmonic modes, prevention of nonlinear properties degradation, maintaining of a high optical-damage resistance, particularly in the shorter wavelength region. MgO:$LiNbO_3$ (MgO:LN) was demonstrated to be a good nonlinear material for blue generation: compared with non-doped LN, it presents higher resistance to photorefractive damage, decreased coercive field and a large nonlinear coefficient $d_{33} \sim 25$ (±2.5) pm/V.[3),4)] CW blue power of 17.3 mW at 426 nm was demonstrated from a AlGaAs laser diode with 55-mW output power by using a MgO:LN proton-exchanged waveguide.[5)] However, these waveguides has some limitations, such as mode field mismatching caused by dispersion and refractive index profiles, a trade-off between index change and nonlinearity[6)] that degrades to about 90% of the original d_{33} value even after annealing.

In order to overcome these problems a fabrication process for realizing high efficiency and high power SHG waveguide devices by bonding and ultra-precision machining techniques was introduced by our group: thus, a ridge-type waveguide QPM-SHG MgO:LN device that preserves the original performances of the nonlinear crystal can be obtained. This research reports on our efforts toward scaling blue light obtained by frequency-doubling from a PP MgO:LN ridge-type waveguide using a diode end-pumped Nd:YAG laser operating at 946 nm as a fundamental source.

Based on the relation between the wavelength tuning of SHG and the periodicity of domain-inverted regions, a ridge-type MgO:LN waveguide of 4.6 μm periodicity was fabricated by ultra-precision machining to generate blue light at 473 nm. Figure 1 shows the procedure of fabrication. First, the periodically domain-inverted regions were formed on a MgO:LN substrate (3°-off X-cut) by the 2D high-voltage application technique (Figure 1a). Then a resin adhesive was used to glue the obtained comb-electrode-formed surface to a LN substrate (Figure 1b). In the next step (Figure 1c) the MgO:LN substrate was thinned by flat-grinding and surface finishing: thus, a 4 μm-thick planar waveguide was realized. In the final step (Figure 1d), the ridge-shaped structure was processed by machining to form a ridge-type waveguide.

A sketch of the experimental set-up is presented in Figure 2. The fundamental 946-nm radiation for frequency doubling was provided by a home-made Nd:YAG laser. For an absorbed pump power at 809 nm of 4.2 W the polarized output was 1.1 W in a Gaussian distribution ($M^2 = 1.05$); the slope efficiency was 38%. Three periodically poled MgO:LN ridge-type waveguides, each of 1.4 mm-width, were prepared. First one has 8.5-mm length and both the input and output surfaces were cut at an angle $\alpha = 10°$ and AR coated at 946 nm by SiO_2 monolayer. The second one of 6-mm length has the input and output surfaces cut at $\alpha = 10°$, while the third one has 12-mm length and only the input surface cut at $\alpha = 6°$; these two samples have no coating at 946 nm. No coating was provided at 473 nm for all the waveguides. The MgO:LN ridge-type waveguide was placed on an aluminum plate whose temperature was controlled within 0.1 °C accuracy.

The 473-nm power as a function of the 946-nm power coupled into the waveguide is presented in Figure 3. The maximum blue power of 189 mW was obtained for the 8.5-mm-long MgO:LN waveguide with a conversion efficiency of 49%. If the Fresnel loss on the waveguide output surface is considered, the maximum internal blue-light power is 222 mW, corresponding to a conversion efficiency of 58%. As the fundamental power before the waveguide was 670 mW the overall conversion efficiency is 28%; improving the 946 nm radiation coupling efficiency into the waveguide could increase the device overall efficiency. The maximum blue power for the 6-mm-long MgO:LN waveguide was 155 mW with 42% conversion efficiency (182-mW blue

internal power with 49% conversion efficiency), while 147 mW with a conversion efficiency of 48% (173-mW blue internal power with 56% conversion efficiency) were obtained for the 12-mm-long MgO:LN waveguide. The highest conversion efficiency of 63% (internal conversion efficiency of 74%) was obtained for a blue power of 99 mW from the longest waveguide used in experiments. During an hour measurement, the peak-to-peak fluctuations for the 946-nm maximum power were ±1.3%, while the blue power fluctuations were ±4.0%. The phase matching temperature was 36.3 °C and the measured acceptance bandwidth ΔT was 2.3 °C, in very good agreement with the predicted theoretical value of 2.35 °C.

In conclusion, CW blue-light generation from a periodically poled MgO:$LiNbO_3$ waveguide by frequency-doubling of a diode end-pumped Nd:YAG laser operating at 946 nm is reported. The maximum output power at 473 nm was 189 mW with 49% conversion efficiency (222 mW internal power with 58% conversion efficiency), indicating the potential for high-power SHG of the ridge-type waveguide fabricated by ultra-precision machining.

References

1) G. W. Ross, M. Pollnau, P. G. R. Smith, W. A. Clarkson, P. E. Britton and D. C. Hanna, *Opt. Lett.* **23**, 171 (1998).
2) S. Spiekermann, H. Karlsson and F. Laurell, *Appl. Opt.* **40**, 1979 (2001).
3) I. Shoji, T. Kondo, A. Kitamoto, M. Shirane and R. Ito, *J. Opt. Soc. Am. B* **14**, 2268 (1997).
4) A. Kuroda, S. Kurimura and Y. Uesu, *Appl. Phys. Lett.* **69**, 1565 (1999).
5) T. Sugita, K. Mizuuchi, Y. Kitaoka and K. Yamamoto, *Opt. Lett.* **24**, 1590 (1999).
6) K. Mizuuchi, H. Ohta, K. Yamamoto and M. Kato, *Opt. Lett.* **22**, 1217 (1997).

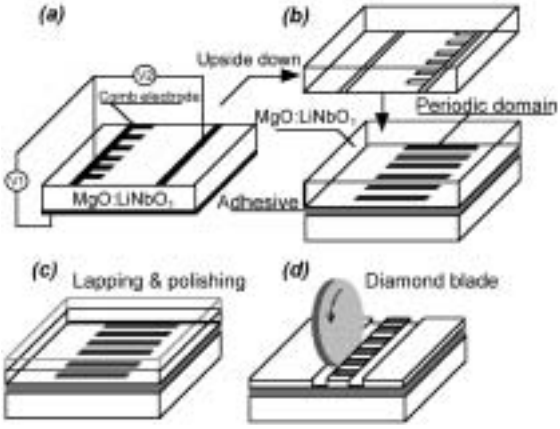

Figure 1. Fabrication steps of a periodically poled MgO:LN ridge-type waveguide by ultra-precision machining: (a) obtaining of the domain-inverted regions, (b) adhesion with a LN substrate, (c) flat grinding and polishing, and (d) ultra-precision grinding.

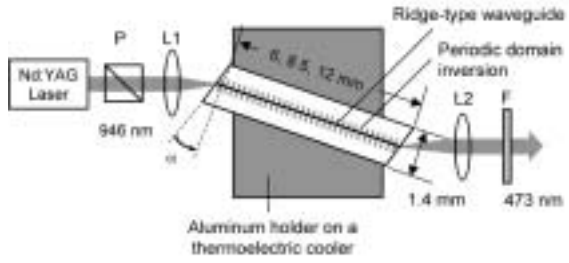

Figure 2. Schematic diagram of the experimental set-up. P: polarizer; L1: focusing lens; L2: collimating lens; F: 946-nm cut filter.

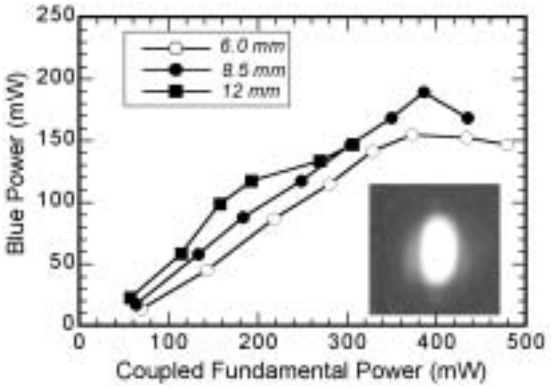

Figure 3. Output power at 473 nm versus the 946-nm power coupled into the waveguide. The inset shows a typical blue light far-field distribution.

IX-B-6 High-Power Continuous Wave Green Generation by Single-Pass Frequency Doubling of a Nd:$GdVO_4$ Laser in a Periodically Poled MgO:$LiNbO_3$ Operating at Room Temperature

MIZUUCHI, Kiminori[1]; MORIKAWA, Akihiro; SUGITA, Tomoya[1]; YAMAMOTO, Kazuhisa[1]; PAVEL, Nicolaie[2]; SHOJI, Ichiro; TAIRA, Takunori

([1]Matsushita Co., Ltd., Osaka; [2]IMS and IAP-NILPRP, Romania)

[*Jpn. J. Appl. Phys.* **42**, L1296 (2003)]

Due to its high effective nonlinear coefficient and the possibility of obtaining non-critical phase matching in single-pass continuous wave (CW) pumping scheme, the periodically poled $LiNbO_3$ (PPLN) crystal continues to attract a great interest as a QPM device for generation in blue, green, or violet ranges. Employing a 50-mm-long first-order PPLN sample, CW powers of 2.7-W green[1)] and 60-mW blue[2)] were demonstrated, respectively. It is known, however, that PPLN has significant problems for visible light radiation, such as green-induced infrared absorption and optical damage. Although phase matching at high temperature close of 200 °C was used,[2)] power instabilities and thermal lens effects could not be completely suppressed. Thus, to date, room temperature CW operation close or in excess of 1 W level was not obtained from a single-pass pumped PPLN crystal.

In order to overcome these problems, it was recently proposed[3)] to utilize periodically poled MgO:$LiNbO_3$

(PPMgLN). Due to its larger nonlinear susceptibilities, higher resistance against photorefractive damage and shorter wavelength transparency compared with PPLN, PPMgLN is a very attractive material for generation of visible light through SHG by QPM process. Moreover, because of its low coercive field,[4] it was demonstrated that PPMgLN could be fairly easily fabricated by means of electric field poling. Recently, a novel high-voltage multi-pulse poling technique that suppress the penetration of poled region and produces uniform PPMgLN with domain period (Λ) as short as 1.4 μm was developed by our group.[5] This letter reports CW SHG at room temperature in a first-order PPMgLN with Λ = 6.95 mm that was fabricated by this technique.

In order to improve the domain pattern quality for short periodic structure a special attention was paid to understand the domain formation processes in a z-cut MgLN crystal. A large resistance reduction was found in a 0.5-mm-thick z-cut MgLN during a conventional electric-field-poling process. Large leakage current was observed in the electric circuit after poling process, which was explained by the resistance reduction in the poled region from 6×10^{11} to 7×10^{5} Ω·mm. This large resistance reduction may cause irregular side growth and non-uniformity of polarization inversion that, in turn, interrupts the fabrication of short-periodic structures. Such local penetrations under the electrode may shorten the surface and bottom electrodes and cause large leakage current between electrodes, which degrade uniformity of electric field. Then, in order to realize uniform PPMgLN structure over large areas, local penetration of polarization-inverted regions must be suppressed: a thick crystal and the multi-pulse application method[6] are used to overcome this last problem. The penetration of polarization inversion to the bottom of the crystal could be suppressed by employing thick samples. Shortening the growth time by using short width pulse would control the forward growth, while multiple pulses should supply enough charge for realizing a relatively deep polarization-inverted structure. Figure 1 shows the cross-sectional of the PPMgLN with Λ = 6.95 mm for various depths: the structure presents 50% duty cycle from the +Z surface to a depth of ~300 μm and uniform periodicity was maintained from the surface to ~800-μm depth.

The 1063-nm radiation for frequency doubling was provided by a home-made diode end-pumped Nd:$GdVO_4$ laser that delivers CW 6.8 W output power (M^2 factor of 1.16) for an 808-nm pump power measured at the fiber end of 15.1 W; the slope efficiency was 57%. The output beam depolarization ratio was 1.2% and the power fluctuation during few hours of operation was ±1.1%. For SHG experiments a 10-mm length PPMgLN was used: the PPMgLN end-faces were optically polished and anti-reflection (AR) coated by SiO_2 monolayer for the 1063-nm fundamental wavelength; no coating was provided at 531 nm. The PPMgLN was placed on an aluminum plate whose temperature was controlled within 0.1 °C accuracy with a thermoelectric cooler. The 1063-nm radiation was focused into PPMgLN to a spot size of 17-μm radius.

Figure 2 shows the 531-nm green power after PPMgLN versus the 1063-nm fundamental power measured after the focusing lens. The maximum green power of 0.89 W was obtained for an infrared incident power of 6.23 W, resulting a conversion efficiency of 14.3%. If the Fresnel loss (determined as ~14%) on the output surface is considered the maximum internal green-light power results as 1.03 W, corresponding to a conversion efficiency of 16.5%. The effective nonlinear coefficient was determined as 14 pm/V and the normalized conversion efficiency including the Fresnel loss by reflection was 2.7%/W. Figure 2 shows by continuous line the theoretical modeling using a quadratic relation with this value: a good agreement with the experimental results is observed. The phase matching temperature was 29.5 °C, stable within ±0.3 °C on the entire pumping range.

In conclusion, irregular side growth of polarization inversion was suppressed in a 2-mm thick PPMgLN by using a multi-pulse application poling method. Uniform periodicity and 50% duty cycle with a 6.95-μm domain period was fabricated on 10-mm length of interaction. This structure was used to obtain perfect first-order QPM in the bulk PPMgLN at 1063 nm wavelength: CW 531-nm green light of 0.89 W with 14.2% power conversion efficiency was obtained (internal power of 1.03 W and 16.5% conversion efficiency) in a single-pass pumping with a Nd:$GdVO_4$ laser.

References

1) G. D.Miller, R. G. Batchko, W. M. Tulloch, D. R. Weise, M. M. Fejer and R. L. Byer, *Opt. Lett.* **22**, 1834 (1997).
2) R. G. Batchko, M. M. Fejer, R. L. Byer, D. Woll, R. Wallenstein, V. Y. Shur and L. Erman, *Opt. Lett.* **24**, 1293, (1999).
3) K. Mizuuchi, K. Yamamoto and M. Kato, *Electron. Lett.* **32**, 2091 (1996).
4) A. Kuroda, S. Kurimura and Y. Uesu, *Appl. Phys. Lett.* **69**, 1565 (1996).
5) K. Mizuuchi, A. Morikawa, T. Sugita and K. Yamamoto, *Jpn. J. Appl. Phys.* **42**, L90 (2003).
6) T. Sugita, K. Mizuuchi, Y. Kitaoka and K. Yamamoto, *Jpn. J. Appl. Phys.* **40**, 3B-222 (2001).

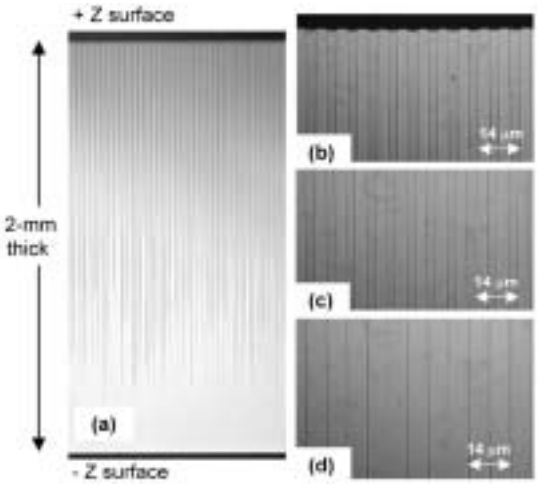

Figure 1. Cross-sectional view (Y face) of first-order PPMgLN with Λ = 6.95 μm: (a) general view, (b) near the surface, (c) at the depth of 300 μm, and (d) at 1-mm depth.

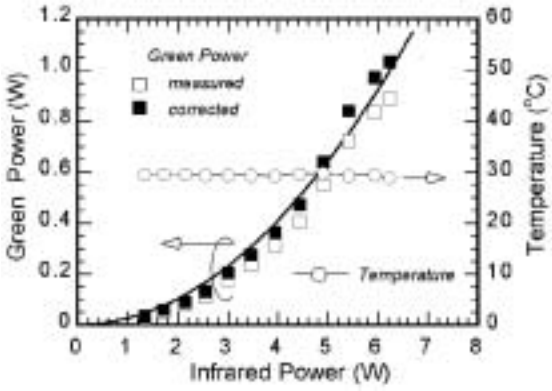

Figure 2. CW 531-nm output power (□- measured and ■- corrected with Fresnel losses) and phase matching temperature (○) *vs*. the 1063-nm incident power.

IX-B-7 Continuous-Wave High-Power Nd:YAG-$KNbO_3$ Laser at 473 nm

PAVEL, Nicolaie[1]; SHOJI, Ichiro; TAIRA, Takunori
([1]IMS and IAP-NILPRP, Romania)

[*Opt. Laser Tech.* **36**, 581 (2004)]

During the past few years much work has been done in order to obtain an efficient and simple solid-state blue laser source, this device being of interest for applications such as display technologies, production of high-density optical disk systems, high-resolution printing, or medical diagnostics. Although the blue semiconductor diode laser is expected to reach the power level necessary for these applications, the frequency-doubling of the 946-nm $^4F_{3/2} \rightarrow {}^4I_{9/2}$ transition in Nd:YAG is a practical and the most used way that leads to blue radiation at 473 nm. Various resonator configurations and nonlinear crystals could be used for frequency-doubling of a Nd:YAG laser operating at 946 nm. The first continuous-wave (CW) diode-pumped Nd:YAG laser that delivered 42-mW at 946 nm was reported by Risk and Lendth,[1)] whereas an attempt of intracavity frequency-doubling by a $LiIO_3$ nonlinear crystal yielded 100 μW of blue light. Dixon *et al.* developed the first 946-nm Nd:YAG laser intracavity frequency-doubled by a $KNbO_3$ crystal:[2)] 5-mW power at 473 nm with 2% optical-to-optical conversion efficiency with respect to the pump power, $\eta_0^{(i)}$, was obtained. A compact source of CW single-frequency radiation at 473 nm with 500 mW output power was developed, employing a diode-pumped miniature Nd:YAG ring laser as a pump source and an external semi-monolithic cavity with $KNbO_3$ crystal.[3)] The best result to date at 473 nm is an output power of 2.8 W with $\eta_0^{(i)}$ = 13.3%: the experimental set-up was a three-arms resonator and BiB_3O_6 nonlinear crystal operating at room temperature was employed for frequency-doubling.[4)]

Some disadvantages of $KNbO_3$ are a small temperature and spectral acceptance bandwidths, photorefractivity effect, and that its domain structure is easily disturbed. However, because of its high value of the nonlinear coefficient and due to its ability to be birefringently phase-matched for second harmonic generation of the 946-nm wavelength this crystal was our choice. This paper reports on our work toward scaling blue light obtained by intracavity frequency-doubling of a diode end-pumped 946-nm Nd:YAG laser, using a $KNbO_3$ nonlinear crystal.

A 1.0-at.% Nd:YAG crystal (3-mm thickness) whose surfaces were anti-reflection (AR) coated at the pumping wavelength of 809 nm and also at 946 and 1064 nm was used in experiments. To achieve efficient heat removal the Nd:YAG crystal was placed in a copper mount whose temperature was kept at 12 °C, and an indium foil was used to improve the thermal contact between the Nd:YAG and the copper heat sink. A 400-μm diameter, 0.22-NA fiber-coupled diode (HLU32 F400, LIMO Co., Germany) was used for CW pumping; the fiber was imaged into the Nd:YAG crystal in a 300-μm diameter spot. Two $KNbO_3$ crystals (Mitsui Chemicals Inc., Japan) of 1.0 and 2.0-mm thickness were cut for type I, critical-phase-matching condition (θ = 90°, ϕ = 59.2°) and placed in a copper holder whose temperature was controlled with 0.1 °C accuracy; the operation temperature was 29.2 °C. Both sides of each $KNbO_3$ were polished to parallel flat surfaces and AR coated at 473 and 946 nm.

The emission of a plane-concave resonator of 70-mm length that contains the Nd:YAG crystal, the polarizing glass plate and the $KNbO_3$ crystal was first investigated. The output mirror has 100-mm radius and it was coated as high-reflection at 946 nm and high-transmission at 473 nm. The maximum power at 473-nm for the 1.0-mm thick $KNbO_3$ crystal was 68 mW for an absorbed pump power of 3.1 W, as shown in Figure 1. The conversion of the available IR power was 10.5%. With the 2.0-mm thick $KNbO_3$ crystal the maximum blue power was 159 mW for an absorbed pump power of 3.3 W: thus $\eta_0^{(i)}$ was 2.7%, while the conversion of the IR power was determined as 21.4%. For these points of operation the transverse mode distribution was Gaussian ($M^2 < 1.05$), but a saturation of the blue power and decrease of the beam quality were obtained as the pump power was further increased.

In order to increase the blue power a V-type resonator, as shown in Figure 2, was designed. The distances M1 to M2 and M2 to M3 were 70 and 55 mm, respectively; the $KNbO_3$ nonlinear crystal was placed very close of mirror M3. Figure 3 shows the blue power versus the absorbed pump power. For the 1.0-mm thick $KNbO_3$ crystal a maximum blue power of 318 mW was obtained for an absorbed pump power of 3.8 W; the conversion efficiency of the IR power was 34.2%. An output power of 418 mW at 473 nm was recorded for the 2.0-mm thick $KNbO_3$ crystal with $\eta_0^{(i)}$ = 6.7%; the conversion of the available IR power was 50%. The 473-nm output beam was linearly polarized (> $1:10^3$) and orthogonal to the 946-nm radiation. Monitoring the maximum blue output power with a powermeter resulted in ±2% power fluctuations during few hours of operation. The stability on millisecond time scale was investigated with a fast photodiode: it shows no fluctuations, indicating no blue problem. No damage of the $KNbO_3$ crystals was observed during the experiments.

For modeling of blue power, the beam distribution inside the resonator was considered independent of the

active medium refractive power induced by optical pumping, with the laser operating far of the threshold.[5),6)] Experimentally we have determined the pump coupling coefficient K_c = 0.032 W^{-1} and the loss L as ~1.5% and ~2.0% for the resonators with the 1.0 and 2.0-mm thick $KNbO_3$, respectively. The beam radius in the Nd:YAG and in $KNbO_3$ were considered independent of the absorbed power, namely 140 and 100 μm, respectively. Figure 3 also shows by continuous lines the modeling of the blue power using this model, where d_{eff} = 13 pm/V was the parameter used for fitting. The agreement between the experimental data and modeling is satisfactory, if one considers that the model assumes that the resonator parameters are optimized for each pump power, which is not the experimental case.

In conclusion, a continuous-wave diode-pumped Nd:YAG laser that operates on the 946-nm $^4F_{3/2} \rightarrow {}^4I_{9/2}$ transition and that is intracavity frequency-doubled to 473 nm using $KNbO_3$ nonlinear crystal is described. The blue maximum power was 418 mW, with 50% conversion of the available IR power, and the optical-to-optical conversion efficiency with respect to the pump power was 6.7%. To the best authors knowledge these are the highest results to date for a diode pumped Nd:YAG rod laser frequency-doubled by a $KNbO_3$ nonlinear crystal.

References

1) W. P. Risk and W. Lenth, *Opt. Lett.* **12**, 993 (1987).
2) G. J. Dixon, Z. M. Zhang, R. S. F. Chang and N. Djeu, *Opt. Lett.* **13**, 137 (1988).
3) M. Bode, I. Freitag, A. Tunnermann and H. Welling, *Opt. Lett.* **22**, 1220 (1997).
4) C. Czeranowsky, E. Heumann and G. Huber, *Opt. Lett.* **28**, 432 (2003).
5) R. G. Smith, *IEEE J. Quantum Electron.* **6**, 215 (1970).
6) A. Agnesi, A. Guandalini and G. Reali, *J. Opt. Soc. Am. B* **19**, 1078 (2002).

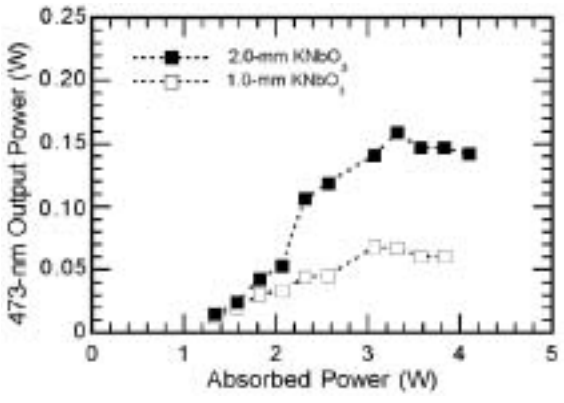

Figure 1. Blue output power *vs.* the absorbed pump power for the linear resonator.

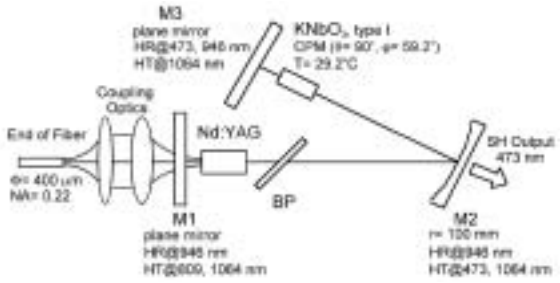

Figure 2. V-type resonator of the diode-pumped 946-nm Nd:YAG laser intracavity frequency-doubled by $KNbO_3$ crystal; BP: glass plate placed at the Brewster angle.

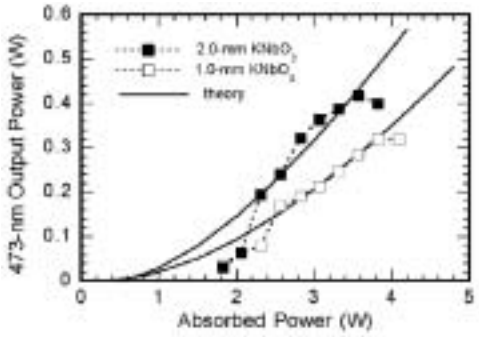

Figure 3. Blue output power *vs.* the absorbed pump power for the V-type resonator: signs for experiments and theory by the continuous lines.

IX-B-8 Room-Temperature, Continuous-Wave 1-W Green Power by Single-Pass Frequency Doubling in a Bulk Periodically Poled $MgO:LiNbO_3$ Crystal

PAVEL, Nicolaie[1]; SHOJI, Ichiro; TAIRA, Takunori; MIZUUCHI, Kiminori[2]; MORIKAWA, Akihiro; SUGITA, Tomoya[2]; YAMAMOTO, Kazuhisa[2]

([1]IMS and IAP-NILPRP, Romania; [2]Matsushita Co., Ltd., Osaka)

[*Opt. Lett.* **29**, 830 (2004)]

Due to its significant advantages of phase-matching an arbitrary wavelength and of accessing high nonlinear coefficient by using an appropriate period of polarization inversion, the second-harmonic generation (SHG) by quasi-phase-matching (QPM) interaction is an attractive method to obtain a compact and high power laser emitting into visible or ultraviolet spectral regions. Because of its simplicity, the single-pass SHG scheme is a solution to obtain continuous wave (CW) operation in blue, green, or ultraviolet ranges. This scheme requires a high nonlinear coefficient and long interaction length with noncritical phase matching: these conditions are well fulfilled by the periodically poled $LiNbO_3$ (PPLN) crystal. It is known, however, that PPLN has significant problems for visible light radiation, such as green- or blue-induced infrared absorption and optical damage. Although phase matching at high temperature of 200 °C[1)] or 140 °C[2)] was used, power instabilities and thermal lens effects could not be completely suppressed.

To overcome these problems, the use of periodically poled MgO:$LiNbO_3$ (PPMgLN) was proposed:[3] this crystal presents larger nonlinear susceptibilities, higher resistance against photorefractive damage and shorter wavelength transparency compared with PPLN. CW blue power of 17.3 mW at 426 nm was demonstrated from a PPMgLN waveguide that was single-pass pumped by a AlGaAs diode laser.[4] A novel high-voltage multi-pulse poling technique that suppress the penetration of poled region and produces uniform PPMgLN with domain period (Λ) as short as 1.4 μm was developed by our group: ultraviolet light at 341.5 nm with a normalized conversion efficiency of 5.4%/W was thus demonstrated.[5] In this letter we report high-power CW frequency-doubling at room temperature in a first-order PPMgLN of Λ = 6.95-μm fabricated by this technique and that was single-pass pumped with a Nd:$GdVO_4$ laser operating at one micron wavelength.

The experimental set-up is shown schematically in Figure 1. Taking into account the high thermal conductivity of Nd:$GdVO_4$ and the fact that the output beam is polarized, a diode-end pumped Nd:$GdVO_4$ laser (Z-type resonator) was build as a pump source: the laser delivers 6.8 W with 45% optical-to-optical efficiency, in a beam with M^2 factor of 1.15; the slope efficiency was 57%. The output beam depolarization ratio was 1.2% and the power fluctuation during few hours of operation was ±1.1%. The laser spectrum, which was investigated by a spectrum analyzer (Q8384 Advantest Co., Japan) with 0.01-nm resolution, was centered at 1062.9 nm and presented four peaks separated by 0.08 nm, each peak with FWHM of ~0.01 nm; the spectrum width was ~0.24 nm.

The fabrication process of PPMgLN with Λ = 6.95-μm and long interaction length was as follows: To obtain a uniform PPMgLN structure over large areas, local penetration of polarization-inverted regions was suppressed by using a thick crystal and the multi-pulse application method.[6] A Z-cut 5-mol% MgO doped LN crystals of 2-mm thickness were used. First, a 100-nm thick Ta film was sputtered on the +Z and –Z faces of the crystals. Next, the patterned electrodes were covered with a 200-nm thick sputtered SiO_2 film. The applied voltage and pulse width were 10 kV and 1 ms, respectively. During the poling process, to lower the coercive field, the samples were heated at ~ 140 °C. After poling the substrate was etched in a 1:2 HNO_3+HF solution at 60 °C for several minutes to reveal the polarization-inverted region on both surfaces of the crystal. The cross sections were examined by cutting samples along Y-faces, polishing and etching. It was found that the structure has 50% duty cycle from the +Z surface to a depth of ~300 μm and uniform periodicity was maintained from the surface to ~800-μm depth; however, the polarization-inverted regions were not realized near the –Z face.

For SHG experiments PPMgLN crystals of 10- and 25-mm length were cut from the poled samples and the end-faces were optically polished and antireflection (AR) coated by SiO_2 monolayer for the 1063-nm wavelength; the SiO_2 coating has no AR effect at 531 nm. The PPMgLN were placed on an aluminum plate whose temperature was controlled within 0.1 °C accuracy using a thermoelectric cooler. A dichroic mirror M, coated as high-reflectivity for 1063 nm and as high-transmission for 531 nm, was used to reflect the fundamental radiation left after PPMgLN.

A maximum CW green power of 0.89 W was measured for the 10-mm-long PPMgLN for an incident infrared power of 6.23 W. If the Fresnel loss (~14%) on the output surface of PPMgLN is considered the maximum internal green-light power results as 1.03 W, corresponding to a conversion efficiency of 16.5%. Figure 2a shows the internal green power and conversion efficiency versus the 1063-nm input power in PPMgLN. The effective nonlinear coefficient was determined as 14 pm/V; thus, the normalized conversion efficiency including the Fresnel loss by reflection was 3.0%/W. For the 25-mm long PPMgLN crystal a maximum green power of 1.18 W was measured. When the Fresnel loss is considered (Figure 2b) the internal power and conversion efficiency were 1.38 W and 19.6%, respectively, while the normalized conversion efficiency was ~3.3%/W; the continuous line of Figure 2b shows the expected results with this value.

The phase matching temperature was 29.5 °C, stable within ±0.3 °C on the entire pumping range. The experimental data for the acceptance bandwidth ΔT was 3.9 °C, while the theoretical value obtained by taking into account the Sellmeier equations for LN crystal[7] resulted as 3.4 °C; good agreement could be observed. During few hours of operation output power instabilities or variations of the green beam pattern that could be caused by thermal lens effects or optical damage of PPMgLN were not observed. Then, the strong resistance against photorefractive damage of MgO:$LiNbO_3$ enables achieving this green power level and highly efficient SHG efficiency in a CW single-pass pumping scheme.

In conclusion, CW power of 1.18 W at 531 nm with 16.8% power conversion efficiency was obtained from a 25-mm-long uncoated bulk PPMgLN in a single-pass frequency doubling scheme using a Nd:GdVO4 laser as pumping source; the PPMgLN internal power of and conversion efficiency were 1.38 W and 19.6%, respectively. To the authors best knowledge this is the highest power ever reported by quasi-phase matching at room temperature. The present result supports the prospect of obtaining compact and high power visible source based on bulk periodically poled MgO:$LiNbO_3$.

References

1) G. D. Miller, R. G. Batchko, W. M. Tulloch, D. R. Weise, M. M. Fejer and R. L. Byer, *Opt. Lett.* **22**, 1834 (1997).
2) G. W. Ross, M. Pollnau, P. G. R. Smith, W. A. Clarkson, P. E. Britton and D. C. Hanna, *Opt. Lett.* **23**, 171 (1998).
3) K. Mizuuchi, K. Yamamoto and M. Kato, *Electron. Lett.* **32**, 2091 (1996).
4) T. Sugita, K. Mizuuchi, Y. Kitaoka and K. Yamamoto, *Opt. Lett.* **24**, 1590 (1999).
5) K. Mizuuchi, A. Morikawa, T. Sugita and K. Yamamoto, *Jpn. J. Appl. Phys.* **42**, L90 (2003).
6) T. Sugita, K. Mizuuchi, Y. Kitaoka and K. Yamamoto, *Jpn. J. Appl. Phys.* **40**, 1751 (2001).
7) G. J. Edwards and M. Lawrence, *Opt. Quantum Electron.* **16**, 373 (1984).

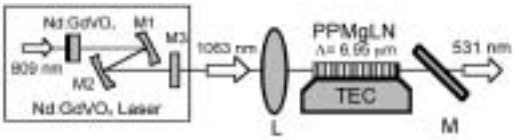

Figure 1. The experimental set-up used for SHG generation. L: focusing lens, TEC: thermoelectric cooler, M1, M2, M3, M: mirrors.

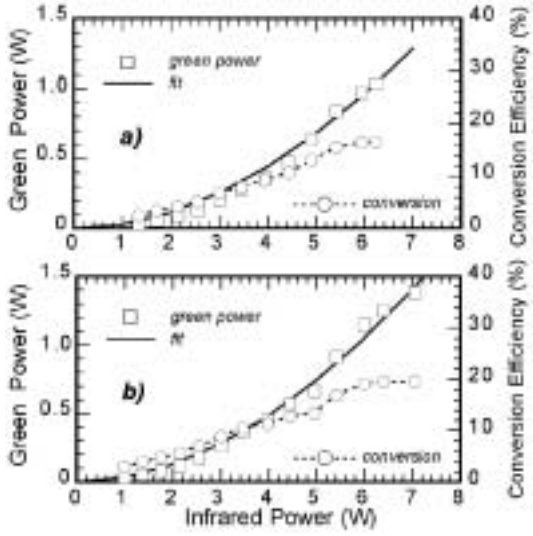

Figure 2. Internal cw 531-nm output power and internal conversion efficiency versus the 1063-nm incident power for a) 10-mm and b) 25-mm long PPMgLN. Continuous lines shows the modeling with a quadratic dependence.

Research Center for Molecular-Scale Nanoscience

IX-C Nano-science and Nano-Technology toward Molecular Scale Electronics

Studies on electric properties of organic and in-organic nano structures are challenging field in material science. Those of aggregates, crystals, or polymers which are made from a large number of molecules or atoms have been already established. In contrast, electronics of nano scale materials which are constructed from small number or single molecules are the forefront of science and technology, and have been revealed gradually to show their diverse phenomena such as quantum conductance, the Kondo effect, the Coulomb blockade, and resonance tunneling. In order to promote this field further, we are studying preparation or fabrication of new organic and in-organic nano materials, and developing new methods to measure their physical properties.

IX-C-1 Bridging Nano-Gap Electrodes by *In Situ* Electropolymerization of a Bis-Terthiophenylphenanthroline Ruthenium Complex

ARAKI, Koiti[1,3]; ENDO, Hiroaki[1,2]; MASUDA, Gou[2]; OGAWA, Takuji[1]
([1]IMS, JST; [3]Ehime Univ.; [3]Univ. São Paulo)

[*Chem. Eur. J.* **10**, 3331–3340 (2004)]

A novel 3,8-bis-terthiophenyl-(1,10-phenanthroline) coordinated to [Ru(bpy)$_2$] was synthesized and characterized by electrochemical and spectroscopic techniques, and shown to be a suitable starting material for the electrodeposition of functionalized molecular wires in between nano-gap electrodes, generating stable molecular nano-devices. Temperature dependent non-linear *I-V* curves were obtained in the 80 to 300 K range. The material can be deposited on ITO also, forming compact electrochromic films at surface concentrations lower than about 1×10^{-8} mol·cm^2, but a more loosely bond fibrous form is preferentially deposited at higher surface concentrations.

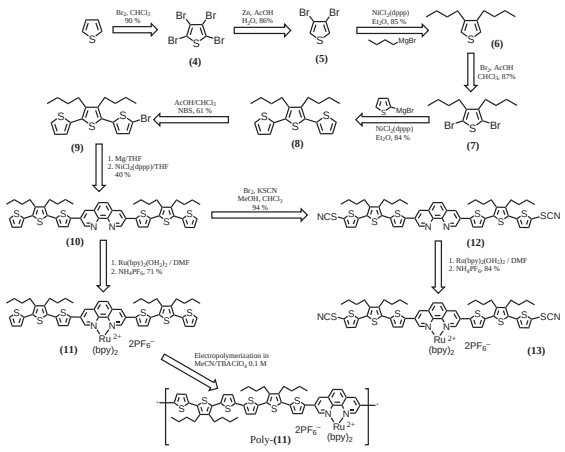

Scheme 1.

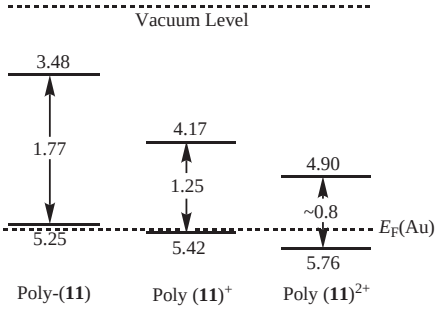

Scheme 2.

IX-C-2 Multi Curve Fitting Analysis of Temperature Dependent *I-V* Curves of Poly-Hexathiophenephenanthroline Bridged Nano-Gap Electrodes

ARAKI, Koiti[1,3]; ENDO, Hiroaki[1,2]; TANAKA, Hirofumi[1]; OGAWA, Takuji[1]
([1]IMS, JST; [2]Ehime Univ.; [3]Univ. São Paulo)

[*Jpn. J. Appl. Phys.* **43**, L634–L636 (2004)]

Stable junctions were obtained by preparing poly-hexathienylphenanthroline coordinated wires to [Ru(bpy)$_2$] complexes directly in the Au electrode nano-gaps by electropolymerization. Reproducible non-linear and strongly temperature dependent curves, similar to that found for π-conjugated dithiols and diisocyanides self-assembled inside nano-holes, were obtained rather than a tunneling behavior commonly found in alkane-thiol self-assembled monolayers. This is the first time that such a consistent series of data are collected for a polymer and interpreted based on a multi curve fitting method using a linear combination of tunneling, Frankel-Pool and hopping mechanism, suggesting that various independent conduction pathways may be present.

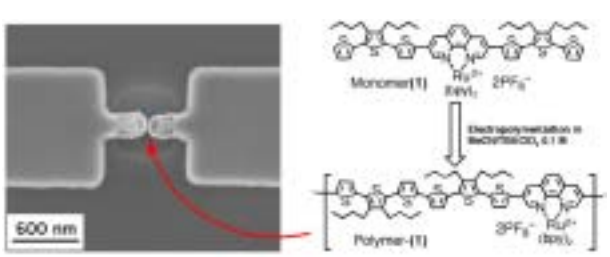

Figure 1.

IX-C-3 Position-Selected Molecular Ruler

TANAKA, Hirofumi; ANDERSON, Mary E.[1]; HORN, Mark W.[1]; WEISS, Paul S.[1]
([1]Pennsylvania State Univ.)

[*Jpn. J. Appl. Phys.* **43**, L950–L953 (2004)]

The molecular ruler method allows the precise control of the gap between a parent gold structure and a deposited daughter structure using a conveniently grown self-assembled molecular multilayer as a lithographic mask. However, we cannot choose a position where the gap should be placed, since the ruler attaches to all exposed gold surfaces. In this work, a convenient method of selecting the position of nano-gaps by further patterning the molecular multilayer using low-energy electron beam irradiation and piranha etchant is described.

The development of a convenient technique to fabricate precise nanostructures in large quantity is required for many types of application, such as electric devices, micromachines and biological equipment, since the "top-down" approach like electron lithography will reach its physical limit soon. Accordingly, it is urgently required to develop "bottom-up" techniques such as molecular self-assembly in order to achieve this goal.

Recently, many researchers have tried to create nano-gaps between electrodes to measure the electronic property of a single molecule or several molecules. For example, shadow evaporation, the break junction method and e-beam lithography have been investigated for this purpose. One of the most convenient approaches coupling the top-down and bottom-up approaches was developed as the molecular ruler method. This is based on the use of compact self-assembled molecular multilayers grown on a parent gold structure as a convenient photoresist. Gap width is precisely controlled by the length of the molecular ruler and the number of monolayers deposited on the top of parent structures, for example, prepared by conventional lithography techniques. One of the advantages of this method is that both sides of the gap are vertically parallel and the desired gap sides can be formed precisely. Another advantage is the position of the gap can be controlled. Multilayers are grown by the successive sequential deposition of monolayers of α,ω-mercaptoalkanoic acid ($HS(CH_2)_xCOOH$) and Cu^{2+} ions, until desired thickness is achieved.

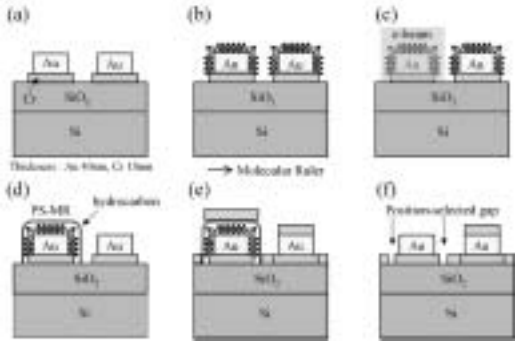

Figure 1.

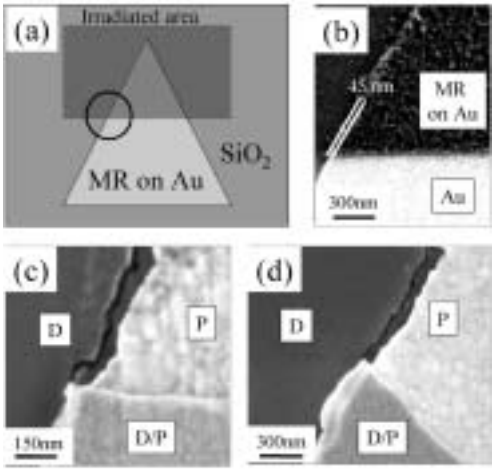

Figure 2.

IX-C-4 Advances in Nanolithography Using Molecular Rulers

ANDERSON, Mary E.[1]; TAN, L. P.[1]; TANAKA, Hirofumi[2]; MIHOK, M.[1]; LEE, H.[1]; HORN, Mark W.[1]; WEISS, Paul S.[1]
([1]Pennsylvania State Univ.; [2]IMS and Pennsylvania State Univ.)

[*J. Vac. Sci. Technol. B* **21**, 3116–3119 (2003)]

The combination of conventional lithographic techniques with chemical self-assembly allows for the creation of nanostructures whose spacing and edge resolution reach nanometer-scale precision. The controlled placement and thickness of self-assembled multilayers composed of alternating layers of α,ϖ-mercaptoalkanoic acids and coordinated metal ions form precise molecular ruler resists that enable the production of tailored and lithographically defined metal patterns. Initial structures created by conventional techniques are referred to as parents and subsequent structures generated by the molecular ruler process are identified as daughters. We report the further creation of subsequent generation structures ~granddaughters! that have sub-100 nm dimensions. The granddaughter structures are created by forming molecular rulers on parent and daughter structures, and can be isolated by removing sacrificial parent and/or daughter structures. This process has also been utilized in combination with parent structures created by the process of nanosphere lithography to produce arrays

of metal features with 10 nm spacings. Since our original report, we have improved the throughput and reproducibility of the molecular ruler process by automating its iterative nature and by utilizing appropriate chemical lift-off solutions.

IX-C-5 Reactive Ligand-Protected Nano-Particles

ARAKI, Koiti[1,3]; MIZUGUCHI, Eisuke[1,2]; TANAKA, Hirofumi[1]; OGAWA, Takuji[1]
([1]IMS, JST; [2]Ehime Univ.; [3]Univ. São Paulo)

Gold nano-particles exhibit interesting bonding and electronic properties and have been proposed for many applications such as in photoelectrochemical devices, drug delivery systems and sensors. Such applications exploit the molecule-like electronic properties and the particle like behavior of such materials, behaving as highly dispersed solids possessing an exceedingly high functionalizable surface area. In fact, a very significant number of atoms constituting small nano-particles are in the surface and can bond species containing coordinating groups such as thiols, disulphides, phosphines, ammines, *etc.* This means that almost any molecular species can be anchored in the surface imparting their physico-chemical properties to them or leading to the appearance of new properties. On the other hand electronic properties such as light absorption, excited state and electron-transfer characteristics can be controlled by changing the size and the nature of the surface anchored species.

As pointed out above, the preparation of nano-particles with narrow size distribution is a very important issue and some methods have being developed. For example, Brust et al developed a general method for the preparation of thiol-protected gold-nanoparticles with a narrow size distribution, based on the reduction of $AuCl_4^-$ in toluene with an aqueous $NaBH_4$ solution. The toluene solution also contains protecting species such as *n*-dodecanethiol, essential for the stabilization of the metal clusters, and tetraoctylammonium bromide (phase transfer agent). Teranishi *et al.* have shown that *n*-dodecanethiol protected Au-nanoparticles with very narrow size distribution can be obtained by controlled thermal treatment of previously prepared solid samples.

Another main issue for the widespread use of gold-nanoparticles is the sluggishness of the functionalization reactions, which in the case of *n*-dodecanethiol protected material generally can take more than a couple of days. To overcome such drawback more weakly binding protecting groups such as triphenylphosphine, amines and *terc*-dodecanethiol have being proposed. However, in the first case only very small (~1–2 nm diameter) nanoparticles can be obtained and the reactivity are not so much higher in any case. For this reason, even very unstable gold-nanoparticle solutions, obtained in the absence of coordinating organic protecting groups, have been employed. This starting material is quite unstable and should be used soon after its preparation, making almost impossible its proper characterization before use. This is a main issue since can compromise their applications. We disclosed a method for the preparation of highly reactive ligand-protected nanoparticles.

IX-D Development of Organic Semiconductors for Molecular Thin-Film Devices

Organic light-emitting diodes (OLEDs) and organic field-effect transistors (OFETs) based on π-conjugated oligomers have been extensively studied as molecular thin-film devices. Organic semiconductors with low injection barriers and high mobilities are required for highly efficient OLEDs and OFETs. Radical cations or anions of an organic semiconductor have to be generated easily at the interface with an electrode (or a dielectric), and holes or electrons must move fast in the semiconducting layer. Compared with organic *p*-type semiconductors, organic *n*-type semiconductors for practical use are few and rather difficult to develop. Recently, we found that perfluorinated oligomers are efficient electron-transport materials for OLEDs.

IX-D-1 Organic Thin-Film Transistors Based on Anthracene Oligomers

INOUE, Youji[1]; TOKITO, Shizuo[1]; ITO, Kaname; SUZUKI, Toshiyasu
([1]NHK Sci. Tech. Res. Labs.)

[*J. Appl. Phys.* **95**, 5795–5799 (2004)]

OFETs with an active layer based on the organic semiconducting anthracene oligomers, 2,2'-bianthracene (**2A**), 2,6-trianthracene (**3A**), and their dihexyl derivatives (**DH-2A** and **DH-3A**), were fabricated. It was found that thin films of anthracene oligomers deposited by thermal evaporation had lamellar structures with a high degree of molecular ordering. Consequently, the OFETs based on anthracene oligomers showed high field-effect mobilities. The mobility of the OFETs was increased by the oligomerization and the substitution of alkyl groups. **DH-2A** on a SiO_2/Si substrate showed the highest mobility of 0.13 cm^2/V s. It was also found that the electrical characteristics of the OFETs were improved by using a Ta_2O_5 gate insulator.

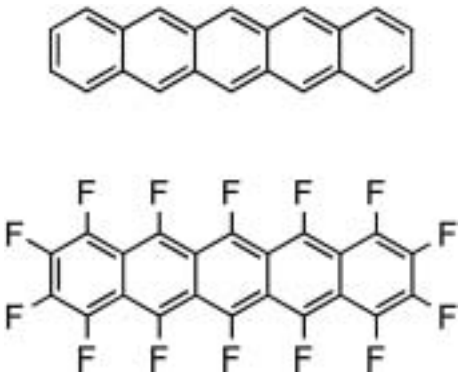

Figure 1. Structures of pentacene and perfluoropentacene.

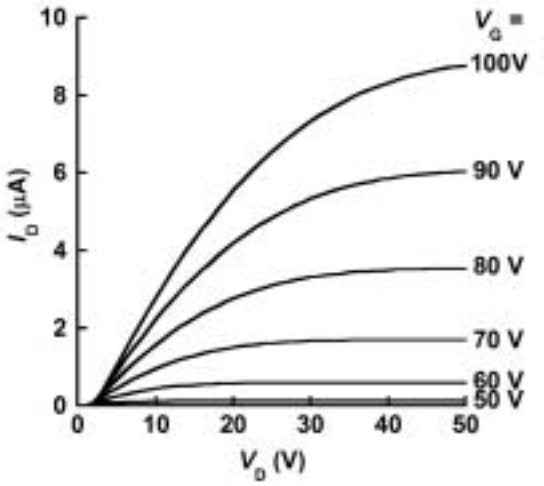

Figure 2. Drain current (I_D) versus drain voltage (V_D) characteristics as a function of gate voltage (V_G) for a perfluoropentacene OFET.

IX-D-2 Perfluoropentacene: High-Performance *p-n* Junctions and Complementary Circuits with Pentacene

SAKAMOTO, Youichi; SUZUKI, Toshiyasu; KOBAYASHI, Masafumi[1]; GAO, Yuan[1]; FUKAI, Yasushi[1]; INOUE, Youji[2]; SATO, Fumio[2]; TOKITO, Shizuo[2]
([1]Kanto Denka Kogyo; [2]NHK Sci. Tech. Res. Labs.)

[*J. Am. Chem. Soc.* **126**, 8138–8140 (2004)]

We report the synthesis and characterization of perfluoropentacene as an *n*-type semiconductor for OFETs. Perfluoropentacene is a planar and crystalline material that adopts a herringbone structure as observed for pentacene. OFETs with perfluoropentacene were constructed using top-contact geometry, and the electron mobility of 0.11 cm^2/V s was observed. Bipolar OFETs with perfluoropentacene and pentacene function at both negative and positive gate voltages. The improved *p-n* junctions are probably because of the similar d-spacings of both acenes. Complementary inverter circuits were fabricated, and the transfer characteristics exhibit a sharp inversion of the output signal with a high voltage gain.

IX-E Field-Effect Transistors with Organic Semiconductors

Considerable attention has recently focused on organic field-effect transistors (OFET) because of their potential use in low-cost flexible electronic devices. We have studied output characteristics of OFET devices based on newly synthesized organic compounds.

IX-E-1 Field-Effect Transistors Based on Dicyanopyrazinoquinoxaline Derivatives

NISHIDA, Jun-ichi[1]; NARASO[1]; MURAI, Shiro[1]; FUJIWARA, Eiichi; TADA, Hirokazu; TOMURA, Masaaki; YAMASHITA, Yoshiro[1]
([1]Tokyo Inst. Tech.)

[*Org. Lett.* **6**, 2007–2010 (2004)]

Dicyanopyrazinoquinoxaline derivatives (Figure 1) have been prepared and characterized by using single-crystal X-ray structure analysis and redox potential measurements. They have strong electron-accepting properties due to the pyrazinopyrazine skeletons as well as the cyano groups. Substituents can be easily introduced at the benzene ring and control the HOMO-LUMO energy gap and the molecular packing. Figure 2 shows output characteristics of a bottom-contact OFET based on compound 1a. It was found that the compound **1a** exhibited *n*-type semiconducting behavior with carrier mobility of 3.6×10^{-6} cm^2/Vs. The compounds examined operated as N-type OFETs. The mobility and on/off ratio of the devices are summarized in Table 1.

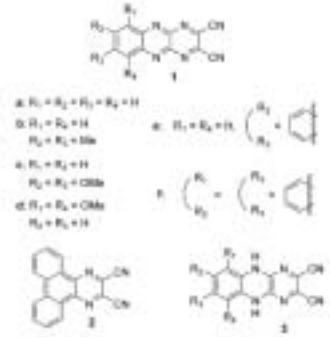

Figure 1. Molecular structures of dicyanopyrazinoquinoxaline derivatives.

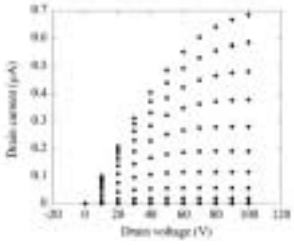

Figure 2. Output characteristics of the OFET based on compound **1a**. Gate voltages were varied from 0 to 100 V with an increment of 10 V.

Table 1. Field-effect mobilities and on/off current ratios of FETs based on dicyanopyrazinoquinoxaline derivatives.

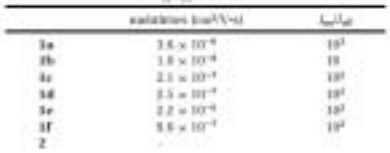

IX-E-2 Low-Voltage Organic Field-Effect Transistors Based on Ta_2O_5 as Gate Insulator Material

SAKAI, Heisuke[1]; FURUKAWA, Yukio[1]; FUJIWARA, Eiichi; TADA, Hirokazu
([1]Waseda Univ.)

[*Chem. Lett.* in press]

A thin film of Ta_2O_5 was prepared by sputtering on heavily-doped silicon substrates and used as a gate insulator of field-effect transistors. Poly(2-methoxy-5-(2'-ethylhexyloxy)-1,4-phenylenevinylene) (MEH-PPV) and pentacene were used as active semiconductors. Interdigital Au electrodes, which consisted of 25 pairs with 25 μm in spacing, 4 mm in width, and 50 nm in thickness, were prepared on the organic layer and used as the source and drain electrodes. Clear saturation in drain currents was observed at low drive voltage of about –3 V as shown in Figure 1. MEH-PPV and pentacence exhibited *p*-type semiconducting behaviors with mobilities of 4.6×10^{-4} cm^2/V s and 0.8 cm^2/V s, respectively.

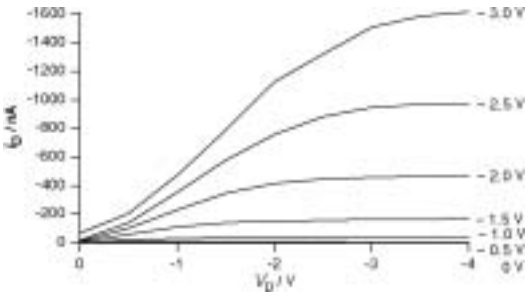

Figure 1. Output characteristics of an FET based on MEH-PPV with a Ta_2O_5 gate insulator.

IX-E-3 Visible Light Emission from Polymer-Based Field-Effect Transistors

SAKANOUE, Tomo[1]; FUJIWARA, Eiichi; YAMADA, Ryo; TADA, Hirokazu
([1]GUAS)

[*Appl. Phys. Lett.* **84**, 3037–3039 (2004)]

Field-effect transistors (FETs) based on poly [2-methoxy, 5-(2'-ethyl-hexoxy)-1,4-phenylenevinylene] (MEH-PPV) were prepared with bottom-contact type interdigital electrodes of Cr/Au and Al/Au on the SiO_2/Si substrates. MEH-PPV exhibited a *p*-type semiconducting behavior and orange light emission was observed when the devices were operated in vacuum. It was found that the luminescence efficiency of the FETs with Al/Au electrodes was higher than that of Cr/Au electrodes, as shown in Figure 1. The simultaneous injection of holes and electrons into MEH-PPV occurred efficiently with the application of Al/Au heteroelectrodes.

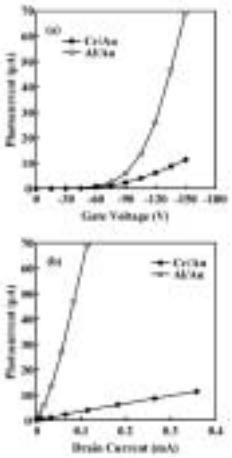

Figure 1. Luminescence intensity detected with a Si photodiode as a function of the gate voltage (a) and the drain current (b). The drain voltage was set at –150 V.

IX-F Molecular Assemblies on Silicon Surfaces *via* Silicon–Carbon Covalent Bonds

Preparation of molecular assemblies on inorganic semiconductors such as silicon and germanium has received a growing interest because of their potential application to stable regist for nano-patterning. We have prepared organic monolayers on silicon by wet process and studied film structures with IR and AFM.

IX-F-1 Temperature Dependence of the Structure of Alkyl Monolayers on Si(111) Surface *via* Si–C Bond by ATR-FT-IR Spectroscopy

YAMADA, Ryo; ARA, Masato[1]; TADA, Hirokazu
([1]GUAS)

[*Chem. Lett*. **33**, 492–493 (2004)]

The temperature dependence of C–H stretching modes of alkyl monolayer formed on Si(111) surface was investigated by an attenuated total reflection Fourier transform infrared spectroscopy from room temperature up to 540 K. Continuous disordering of the monolayer was indicated from the gradual peak shifts toward higher frequency in C–H stretch modes upon heating. The irreversible conformational disorder was introduced in the monolayer above 440 K.

IX-F-2 Non-Contact Atomic Force Microscopy Using Silicon Cantilevers Covered with Organic Monolayers *via* Silicon–Carbon Covalent Bonds

ARA, Masato[1]; SASAHARA, Akira[2]; OHNISHI, Hiroshi[2]; TADA, Hirokazu
([1]GUAS; [2]KAST)

[*Nanotechnology* **15**, S65–S68 (2004)]

Silicon cantilevers covered with dodecyl monolayers anchored *via* silicon–carbon covalent bonds were prepared by a wet process and used for non-contact atomic force microscopy (NC-AFM) of TiO_2(110)–(1×1) surfaces. Figure 1 shows an AFM image of the surface taken with the dodecyl-coated cantilevers. Clear images of atomic rows on atomically flat terraces were observed when the substrate was biased around 2.0 V with respect to the cantilevers. The bias voltage required to give clear images for alkyl-coated cantilevers was higher than that for uncoated ones. Since the cantilevers are thermally and chemically stable, they are applicable to various force microscopy to distinguish chemical species on surfaces.

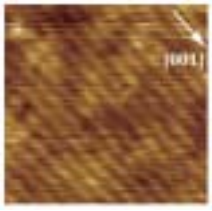

Figure 1. NC-AFM image of the TiO_2 surface (10 nm × 10 nm). The frequency shift and sample bias voltage were set at –186 Hz and 2 V, respectively.

IX-G Low Temperature Scanning Tunneling Microscopy and Spectroscopy of Organic Molecules on Metal Surfaces

The electronic structure of molecules adsorbed by metal surfaces is of growing interest in the field not only of surface science but also of molecular-scale electronic devices. Scanning tunneling microscopy and spectroscopy are powerful tool to investigate molecular arrangements and electronic structure with atomic resolution. We have prepared epitaxial films of phathalocyanine molecules on clean metal surfaces and studies there structures by scanning tunneling microscopy and spectroscopy at low temperature.

IX-G-1 Low Temperature Scanning Tunneling Microscopy of Phthalocyanine Multilayers on Au(111) Surfaces

TAKADA, Masaki[1]; TADA, Hirokazu
([1]GUAS)

[*Chem. Phys. Lett.* **392**, 265–269 (2004)]

We have studied epitaxial trilayer films of cobalt-phthalocyanine (CoPc) on Au(111)-22×√3 surfaces using a scanning tunneling microscope at 78 K. Figure 1 shows an STM image of a CoPc monoleyer on the Au(111) surface. Molecules in each layer were found to form square lattices and stacked along the [1$\bar{1}$0] axis of the Au(111) surface. While CoPc molecules in the first layer were observed at bias voltages of –2.5 to +2.5 V, there were certain ranges of bias voltage in which molecules in the upper layers were invisible. The electronic structures of molecules in upper layers are more localized than those of the first layer, which is affected by the substrate surface.

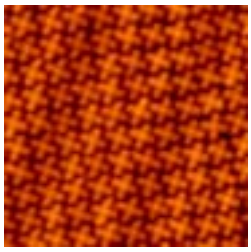

Figure 1. STM image of CoPc molecules on the Au(111) surface (14.6 nm × 14.6 nm).

IX-H Development of New Transport Mechanism Based on Wetting Gradients

Construction and control of wetting gradients on surfaces are of growing interest since the spatiotemporal control of wetting leads to non-mechanical pumping systems in micro-fluidic devices. The imbalance of surface tensions is known to play an important role in the movement of droplets on surfaces. We have succeeded in the reversible control of the direction, magnitude and position of the wetting gradient by in-plane regulation of the electrochemical potential of the thin-film substrate covered with a redox-active self-assembled monolayer. A small droplet of organic liquid was shown to move under the cyclic shift of wetting gradient in aqueous solutions.

IX-H-1 Electrochemically Generated Wetting Gradient and Its Application for the Transport of Droplets

YAMADA, Ryo; TADA, Hirokazu

The in-plane voltage (V_{bias}) was applied to the gold thin film substrate covered with 11-Ferrocenyl-1-undecanethiol (FcC11SH) in addition to the conventional potentiostatic regulation of the potential of the substrate with respect to the reference electrode (RE) (Figure 1a). The current flowing through the substrate causes a continuous potential drop in it. The surface covered with FcC11SH monolayer is known to be hydrophobic and hydrophilic when Fc is reduced and oxidized, respectively. When the potential in the substrate crosses the oxidation potential of the FcC11 HS monolayer, a gradient in the extent of oxidation of the ferrocene, and thus, the wetting across the surface is generated (Figure 1b). The generation and regulation of wetting gradient by this method was confirmed by observing the shape of three droplets of nitrobenzene aligned in the biased direction. The one (Figure 2a; left was more negative) and two (Figure 2b) of the droplets got wet as the V_{bias} was increased. Since the electrochemical reaction of ferrocene is reversible, the observed wetting transition was reversible. Position of the wetting gradient can be moved by E_{offset} and direction and magnitude of it are controlled by V_{bias} in Figure 1a. The spatiotemporal control of the wetting gradient enabled us to manipulate a droplet on a substrate. Figure 3 shows the droplet moved in inchworm-like manner. Initially, the wetting gradient was positioned in the left of the picture and the left side of the substrate was wetting in Figure 3a. As wetting region reached the droplet, droplet spread into left, *i.e.*, wetting area as

shown in Figure 3b. When the position of the wetting gradient was reversed, the droplet shrunk from the right side in Figure 3c. As a result, a net transport of the droplet took place.

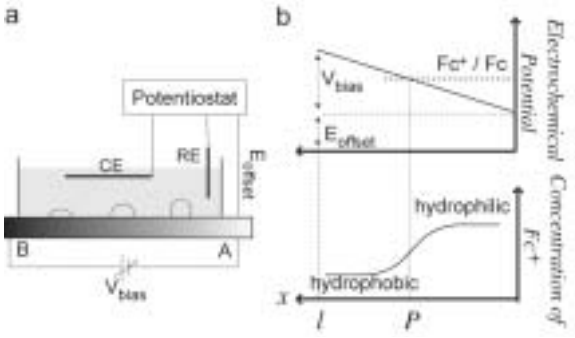

Figure 1. (a) Schematic drawing of the experimental configuration. (b) Potential profile and wetting distribution on the substrate under the biased condition.

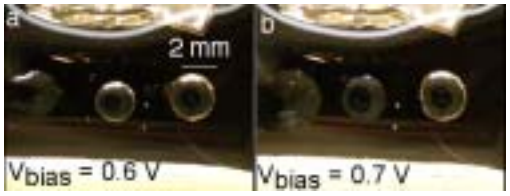

Figure 2. The formation of the wetting gradient by V_{bias}. V_{bias} was –0.6 V(a) and –0.7 V (b). E_{offset} was –300 mV *vs.* AuO_x.

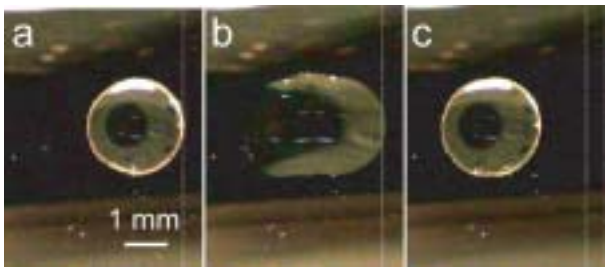

Figure 3. Inchworm motion of the droplet in the solution. See text for details. E_{offset} = (a) –300 mV, (b) –340 mV and (c) –300 mV.

IX-I Development of Precisely-Defined Macromolecules and Their Organization on Substrate Surfaces for Planar Molecular-Scale Electronics Circuits

The concept of molecular-scale electronics is now realized for individual components such as wire, diode, switch, and memory cell, but the fabrication of complete molecular-scale circuits remains challenging because of the difficulty of connecting molecular modules to one another. Molecular monolithic technology, which integrates the wiring, transistors and the required passive elements on a single macromolecule, has been proposed as a promising solution to this problem. In this project we have been trying to establish both the architecture of this novel class of macromolecules and the protocols for their purposive organization on metal/semiconductor substrate surfaces.

IX-I-1 Partially Insulated Molecular Wire as Components for Planar Molecule-Metal Junctions

TANAKA, Shoji

We have developed a series of "partially-insulated" multi-nanometer oligothiophenes to investigate systematically the nature of planar molecule-metal junctions as shown in Figure 1. Charge transport at planar junctions will be controlled by the degree of face-to-face interactions between π-system of conjugated molecules and electrode substrate. Therefore, to define exactly the areas of interactions, we have designed these molecules; the main chain consists of bare π-system as "charge-transfer interface" and insulated π-system possessing electron-donating amino groups as "positive charge-retention sites." Here we describe the electrochemical characterization of these molecules.

Figure 2 shows the cyclic voltammograms of the partially insulated oligothiophenes and the related molecules. In general multi-scan voltammogram of long oligothiophenes (> α-**6T**) is well known to be ill defined as shown in the voltammogram of oligomer **1**. The complicated electrochemical behavior can be attributed to severe interchain interactions among the charged long oligomers that induce molecular aggregation and deposition on the electrode. During these processes, charges on an oligomer are dispersed and lost. In contrast, partially insulated oligothiophenes **3**,**4**,**6** as well as the fully insulated one **2** afforded reversible steady-state voltammograms. These findings suggest that only a one third coverage of the main chain of the α-**9T-18T** is enough to reduce the interchain interactions between the charged species and prevent the aggregation. In the case of oligomer **5**, slight voltammogram deformation, a symptom of aggregation, was observed. This indicates that the steric hindrance of the alkyl substituents on the interchain interactions is minor but not negligible.

Figure 3 shows the differential pulse voltammograms of partially insulated oligothiophenes **2**-**4**. Judging from the potential difference between the first and second peak, the magnitude of on-site Coulomb repulsion in these oligomers was found to decrease in this order: **4** > **2** > **3**. This result may be explained based on the spatial arrangement of the insulated mantle. This component has electron-donating amino groups and tends to attract positive charges. Therefore, separate arrangement of them in the main chain is expected to isolate positive charges from each other resulting in reduction of on-site Coulomb repulsions as illustrated in Figure 3.

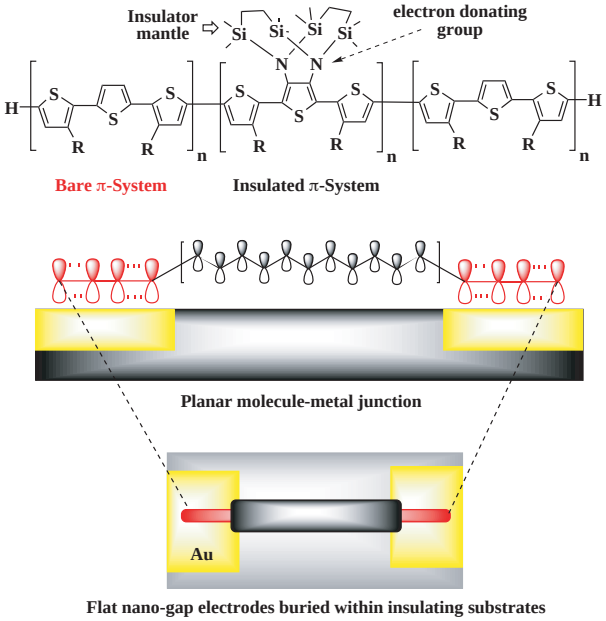

Figure 1. Molecular structure of partially insulated oligothiophenes.

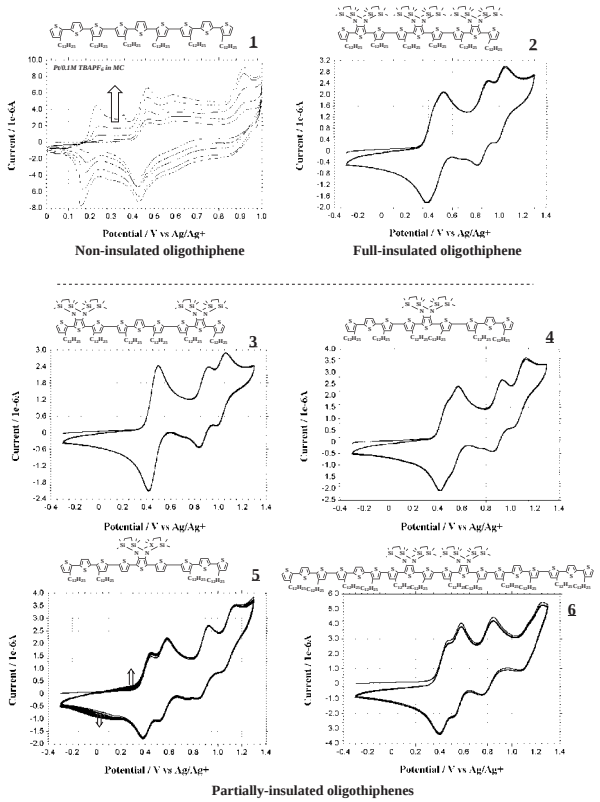

Figure 2. Cyclic voltammograms of oligothiophenes.

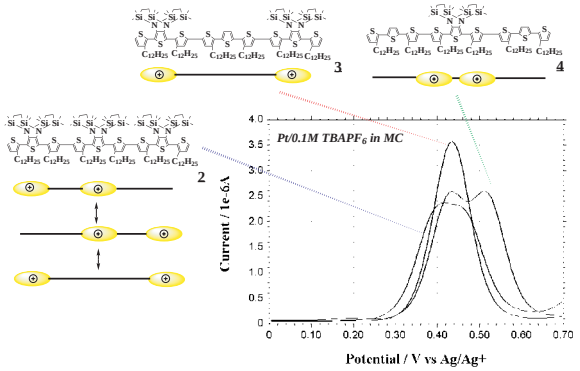

Figure 3. Differential pulse voltammograms of oligothiophenes.

IX-J Development of Novel Heterocyclic Compounds and Their Molecular Assemblies for Advanced Materials

Heterocycles containing sulfur and/or nitrogen atoms are useful as components of functional materials since heteroatoms in their rings are helpful to stabilize ions or ion-radical species, and extended π-conjugation decreases Coulombic repulsion. In addition intermolecular interactions caused by heteroatom contacts can be expected to form novel molecular assemblies. In this project new electron acceptors, donors, and donor-acceptor compounds based on heterocycles such as 1,2,5-thiadiazole and 1,3-dithiole were synthesized and their properties including those of the charge-transfer complexes or ion-radical salts were investigated. Unique crystal structures were constructed by using weak intermolecular interactions such as hydrogen bonding or heteroatom contacts.

IX-J-1 Preparation, Structures and Properties of Novel 1,3-Dithiol-2-Ylidene Derivatives Containing Bis(ethynylpyridine) Units

KUMAGAI, Tsutomu[1]; TOMURA, Masaaki; NISHIDA, Jun-ichi[1]; YAMASHITA, Yoshiro[2]
([1]Tokyo Inst. Tech.; [2]IMS and Tokyo Inst. Tech.)

[*Tetrahedron Lett.* **44**, 6845–6848 (2003)]

1,3-Dithiol-2-ylidene derivatives containing bis(ethynylpyridine) units were synthesized using a Pd-catalyzed reaction of the corresponding dibromide. X-Ray crystal analysis revealed unique crystal structures depending on the aromatic groups. The absorption spectra and redox properties indicated intramolecular charge-transfer interactions between the 1,3-dithiole unit and the pyridyl parts.

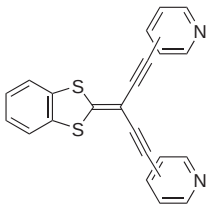

2-dipyridyl, 3-dipyridyl, 4-dipyridyl

IX-J-2 (1,3-Dithiol-2-ylidene)propanedinitrile

TOMURA, Masaaki; YAMASHITA, Yoshiro[1]
([1]IMS and Tokyo Inst. Tech.)

[*Acta Crystallogr., Sect. E* **59**, o1941–o1943 (2003)]

In the crystal structure of the title compound, C_6H_2

N_2S_2, there is a tape structure, as a result of C–H···N hydrogen bonds is found. The molecules stack along the [120] direction in a head-to-tail fashion.

Figure 1. Packing diagram of the title compound viewed along the *c* axis. Dashed lines show the intermolecular S···N and C–H···N contacts.

IX-J-3 Crystal Structure of 4,7-Dibromo-2,1,3-Benzothiadiazole, $C_6H_2Br_2N_2S$

TOMURA, Masaaki; YAMASHITA, Yoshiro[1]
([1]IMS and Tokyo Inst. Tech.)

[*Z. Kristallogr. NCS* **218**, 555–556 (2003)]

The title compound crystallizes in a centrosymmetric $P2_1/c$ space group with two crystallographically independent molecules in the asymmetric unit. The considerable shortenings of the C1–C6, C4–C5, C7–C12 and C10–C11 bonds are observed. Such double bond fixation suggests the quinonoid character of the 2,1,3-benzothiadiazole ring. Short S···N and Br···Br intermolecular heteroatom contacts are found in the crystal. The S···N [3.226(4) and 3.238(4) Å] and the Br···Br [3.542(1) and 3.662(1) Å] distances are 3.4–3.7% and 1.0–4.3% shorter than the sum of the corresponding van der Waals radii, respectively.

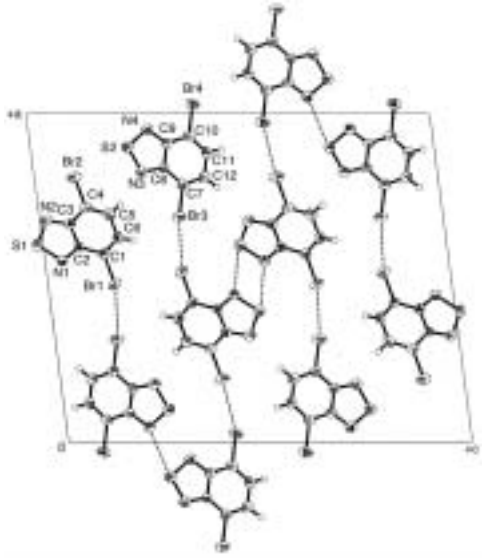

Figure 1. Packing diagram of the title compound viewed along the *b* axis. Dashed lines show the short intermolecular S···N and Br···Br contacts.

IX-J-4 4,5-Diiodo[1,2,5]thiadiazolotetrathiafulvalene

TOMURA, Masaaki; YAMASHITA, Yoshiro[1]
([1]IMS and Tokyo Inst. Tech.)

[*Acta Crystallogr., Sect. E* **60**, o63–o65 (2004)]

In the crystal structure of the title compound, 5-(4,5-diiodo-1,3-dithiol-2-ylidene)-1,3-diaza-2,4,6-trithiapentalene, $C_6I_2N_2S_5$, a large number of short intermolecular heteroatom contacts, such as S···N, S···S, S···I, N···I, and I···I, are observed. The molecules, which are planar within 0.051 Å, stack along the *b* axis in a head-to-head fashion.

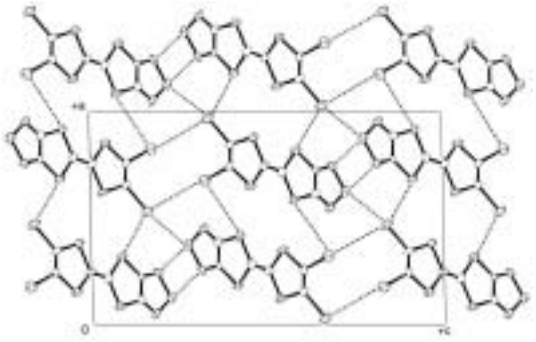

Figure 1. Packing diagram of the title compound viewed along the *b* axis. Dashed lines indicate the short intermolecular S···N, S···I and I···I contacts.

IX-J-5 Synthesis and Characterization of Novel Dipyridylbenzothiadiazole and Bisbenzothiadiazole Derivatives

AKHTARUZZAMAN, Md.[1]; TOMURA, Masaaki; NISHIDA, Jun-ichi[1]; YAMASHITA, Yoshiro[2]
([1]Tokyo Inst. Tech.; [2]IMS and Tokyo Inst. Tech.)

[*J. Org. Chem.* **69**, 2953–2958 (2004)]

Novel dipyridyl compounds containing a mono- and bisbenzothiadiazole unit were synthesized using the Stille coupling reaction. Their pyridinium salts, viologen analogues, were also prepared by the N-alkylation. The X-ray crystallographic analysis of the compounds containing a benzothiadiazole ring revealed nonplanar molecular structures and unique crystal structures depending on the nitrogen positions. The dipyridyl compounds are efficient fluorophores with high electron affinity. The derivative afforded complexes with chloranilic acid and cyanuric acid composed of hydrogen bonding networks. The methyl viologen analogues showed two-stage one-electron reduction waves.

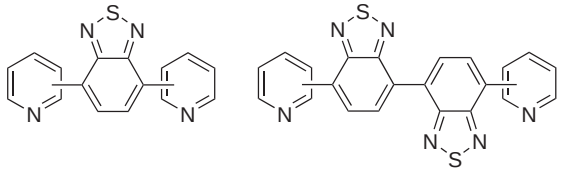

2,2'-dipyridyl, 3,3'-dipyridyl, 4,4'-dipyridyl

IX-K Aquacatalysis

Catalytic organic transformations under mild, safe, and green conditions are important goals in synthetic organic chemistry. We recently reported that several palladium-catalyzed reactions, including π-allylic substitution, carbonylation, the Heck reaction, and Suzuki-Miyaura cross-coupling, took place in water by use of palladium-phosphine complexes bound to an amphiphilic polystyrene-poly(ethylene glycol) graft copolymer (PS-PEG) resin. Rhodium-catalyzed hydroformylation, cyclotrimerization of alkynes, and Michael-type addition of arylboronic acids were also found to proceed smoothly in water. Here we wish to report recent progress in this subject.

IX-K-1 Catalytic Oxidation of Alcohols in Water under Atmospheric Oxygen by Use of an Amphiphilic Resin-Dispersion of Nano-Palladium Catalyst

UOZUMI, Yasuhiro; NAKAO, Ryu

[*Angew. Chem., Int. Ed.* **42**, 194–197 (2003); *Angew. Chem.* **115**, 204–207 (2003)]

An amphiphilic polystyrene-poly(ethylene glycol) resin-dispersion of palladium nanoparticles was designed and prepared with a view toward use for catalysis in water. The catalytic aerobic oxidation of various alcohols forming aldehydes, ketones, and carboxylic acids was achieved in water under atmospheric pressure conditions by use of the PS-PEG supported nano-palladium catalyst.

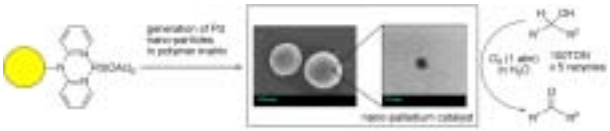

IX-K-2 PS-PEG Resin-Supported Palladium-MOP Complexes. Application in Asymmetric π-Allylic Reduction

UOZUMI, Yasuhiro; HOCKE, Heiko

Homochiral palladium complexes of polymeric 2'-, 6-, and 6'-anchored 2-diphenylphosphino-1,1'-binaphthyl (MOP) ligands were prepared on polystyrene-poly(ethylene glycol) (PS-PEG) resin. The PS-PEG resin-supported palladium-MOP complexes exhibited high catalytic activity, stereoselectivity (up to 80% ee), and recyclability (6 times) in the asymmetric allylic reduction of 1-vinyl-1,2,3,4-tetrahydronaphth-1-yl benzoate to give 1-vinyl-1,2,3,4-tetrahydronaphthalene.

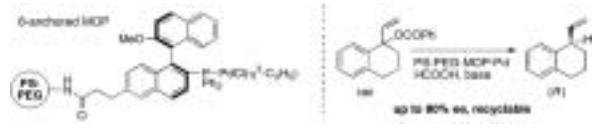

IX-L Development of New Nanomaterials as Components in Advanced Molecular Systems

Nanometer-sized materials exhibit unique electronic behavior. In the quest of advanced redox catalysis, we are currently interested in combining nanometer-sized materials into molecular redox systems. As a basic architecture, a new type of dendrimers were synthesized and their dynamic behavior was examined.

IX-L-1 Synthesis and Properties of New, Spatially Relaxed Dendrons Containing Internal Carboxyl Groups

KIKUZAWA, Yoshihiro; NAGATA, Toshi

[*Bull. Chem. Soc. Jpn.* **75**, 993–1000 (2004)]

We synthesized a series of new dendrons with up to fourteen internal carboxyl groups. These dendrons are made from a branching unit and a spacer unit with a carboxyl group. The growth reactions (formation of the benzylic ether bonds) completed within a few hours, which suggests the high reactivity at the "focal" point of the dendritic framework. The final deprotection of the internal ester groups also proceeded smoothly. These high reactivities were attributed to the presence of the spacer units, which caused spatially relaxed conformations of these molecules. The carboxylate salt form of the dendron produced both normal and reverse micelles in a THF/water mixed solvent according to the fraction.

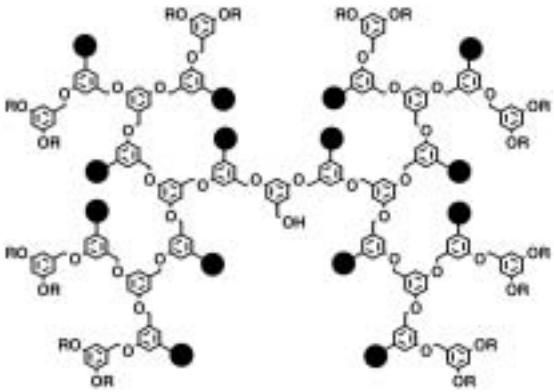

Figure 1. The chemical structure of the dendron (generation 3).

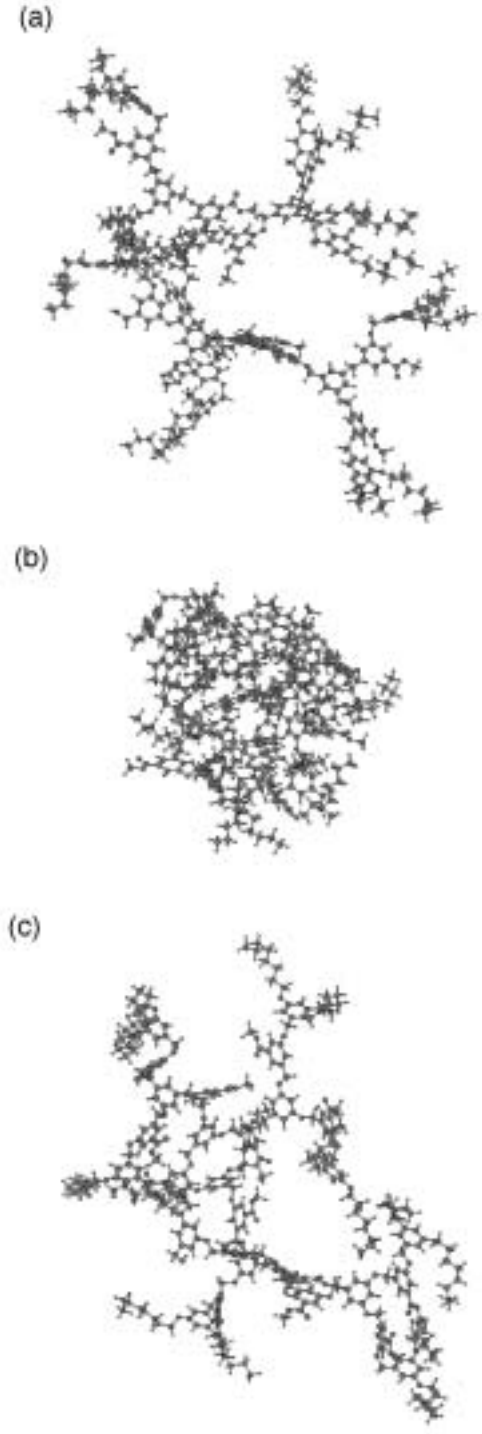

Figure 2. Ball-and-stick representations of the dendron, (a) before the molecular dynamics (MD) run, (b) after 100-ps MD without solvent, (c) after 100-ps MD with explicit solvent ($CHCl_3$).

IX-M Designing Artificial Photosynthesis at Molecular Dimensions

Photosynthesis is one of the finest piece of molecular machinery that Nature has ever created. Its ultrafast electron transfer and following well-organized sequence of chemical transformation have been, and will continue to be, challenging goals for molecular scientists. Our ultimate goal is to design artificial molecular systems that effect multiple chemical reactions triggered by light on the basis of molecular rationale.

IX-M-1 Synthesis of Dendrimer-Linked Porphyrins Bearing Multiple Quinone Moieties at Internal Positions

KIKUZAWA, Yoshihiro; ITO, Hajime; HINO, Takami; NAGATA, Toshi

By use of dendrons described above, we synthesized dendrimer-linked porphyrins bearing up to fourteen quinone moieties at internal positions of the dendrimer. The CV (cyclic voltammetry) and DPV (differential pulse voltammetry) measurements revealed that all the quinone moieties were simultaneously reduced at –1.18 V. The steady-state fluorescence spectra showed reduced emissions (10–15%), which recovered by chemical reduction of quinones by sodium dithionite.

The quinones in these compounds were quantitatively converted to hydroquinone disilyl ethers by irradiation of these compounds in the presence of $PhSSiMe_3$. This suggests that even the quinones at the third-generation positions may accept electrons from the photoexcited porphyrin.

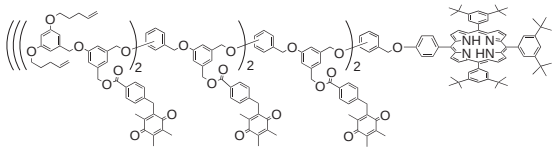

P-G^3(Q)$_{14}$

Figure 1. The structure of the quinone-dendrimer-linked porphyrins.

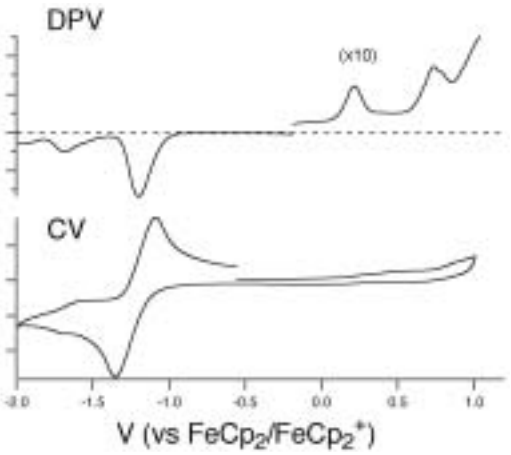

Figure 2. The CV and DPV voltammograms of the quinone-dendrimer-linked porphyrin zinc complex.

IX-N Photochemistry on Well-Defined Surfaces

Upon the irradiation of light in the wavelength range from visible to ultraviolet, a number of adsorbed molecules on metal surfaces reveal variety of photochemical processes, including photo-stimulated desorption, rearrangement of adsorbed states, photodissociation, and photo-initiated reactions with coadsorbates. A central and fundamental question in the surface photochemistry is to clarify how adsorbate-substrate systems are excited by photon irradiation. In addition, since photo-initiated reactions can be induced without any thermal activation of reactants, they may provide good opportunities for studying a new class of surface reactions that may not be induced thermally. We have studied photochemistry of various adsorption systems on well-defined metal and semiconductor surfaces mainly by temperature-programmed desorption (TPD), infrared reflection absorption spectroscopy (IRAS), x-ray photoelectron spectroscopy (XPS), work function measurements, near edge x-ray absorption fine structure (NEXAFS) and angular-resolved time-of-flight (TOF) mass spectrometry of photodesorbed species associated with pulsed laser irradiation. In this year, the photochemistry of alkane on Pt(111) and Cu(111) surfaces was studied mainly by TPD, XPS, and IRAS.

IX-O Ultrafast Dynamics at Well-Defined Surfaces

To understand the mechanism of surface photochemistry, it is vital to know how photoinduced electronic excitation induces adsorbate nuclear motions that ultimately lead to chemical reactions. We demonstrate the real-time observations of surface phonons and adsorbate-substrate vibrational modes by fs time-resolved second harmonics generation (TRSHG). If an excitation light pulse has a duration sufficiently shorter than a period of a vibrational mode or a phonon mode, it can excite the mode with a high degree of temporal and spatial coherence. This coherent nuclear motion modulates the second-order susceptibility $\chi^{(2)}$. Thus, by monitoring the intensity modulation of the second harmonics (SH) generation of a probe pulse, we can observe the evolution of the coherent nuclear motion subsequent to the electronic excitation at the surfaces.

IX-O-1 Direct Time-Domain Observation of Ultrafast Dephasing in Adsorbate-Substrate Vibration under the Influence of a Hot Electron Bath: Cs Adatoms on Pt(111)

WATANABE, Kazuya[1]; TAKAGI, Noriaki[1]; MATSUMOTO, Yoshiyasu
([1]GUAS)

[*Phys. Rev. Lett.* **92**, 57401 (4 pages) (2004)]

Femtosecond time-resolved second harmonic generation has been used to observe vibrational wavepacket dynamics at a Cs-covered Pt(111)surface. The creation and dephasing of vibrational coherence are monitored *via* the intensity modulations in the second harmonic of probe pulses as a function of pump-probe delay. The TRSHG trace obtained from the clean surface shows an instantaneous sharp rise right after the excitation. This is followed by a fast decaying component (t < 1 ps) and a slowly decaying one persistent to the longest delay (t = 6 ps) of the measurements. When the surface is covered with Cs, SH signals are enhanced by about 70 times and strongly modulated waveforms are superimposed on the TRSHG traces. The oscillatory signals are found in TRSHG signals upon the excitations at 580 and 800 nm, which are the manifestation of nuclear wavepacket dynamics on the surface. The Cs-coverage dependence studied in detail indicates that the wavepacket dynamics of Cs–Pt stretching modes and Pt surface phonon modes are responsible for the TRSHG signals. The cos-like initial phase of the oscillatory signals and the coverage dependence of the initial amplitude suggest that the vibrational coherence is associated with the resonant excitation between Cs-derived states in the quantum well of the Cs overlayer. The rate of Cs–Pt vibrational dephasing increases with the surface temperature. This behavior cannot be accounted for by the increasing contribution from hot bands of low frequency modes. Instead, pure dephasing caused by anharmonic coupling between Cs-Pt stretching and parallel modes in the Cs overlayer is likely the dominant mechanism for the vibrational dephasing.

IX-P Multiphoton Photoelectron Spectroscopy of Electronic States of Nano-Structured Materials on Surfaces

Electronic structure and excited state dynamics of nano-structured materials on surfaces are very important for

exploring their properties, thermal reactivity and nonthermal processes including photochemistry and photo-induced charge transfer. For this purpose, we performed multiphoton photoelectron spectroscopy with the fs time resolution. In this year we applied this method to thin films of 3,4,9,10-perylene tetracarboxylic dianhydride (PTCDA).

IX-P-1 Ultrafast Excited State Dynamics in 3,4,9,10-Perylene Tetracarboxylic Dianhydride (PTCDA) Thin Films

INO, Daisuke[1]; WATANABE, Kazuya[1]; TAKAGI, Noriaki[1]; MATSUMOTO, Yoshiyasu
([1]GUAS)

[*Chem. Phys. Lett.* **383**, 261–265 (2003)]

Ultrafast decay dynamics of the excited state in the thin films of 3,4,9,10-perylene tetracarboxylic dianhydride (PTCDA) have been directly observed by using fs time-resolved two-photon photoelectron spectroscopy. The lifetimes were measured up to the excess energy of 2 eV above the S_1 state. The highly excited state presumably S_2 decays with τ = 70 fs and S_1 with τ = 360 ± 12 fs. The lifetime in the S_1 manifold decreases with increase of excess energy, which manifests itself in a time-dependent energy shift of the photoelectron peak originated from the S_1 state.

IX-Q Chemistry of One-Dimensional Nano-Surface Compounds Studied by Scanning Tunneling Microscopy

The fluctuating configurations of low-dimensional structures can be thermodynamically favorable at finite temperatures, because the energy gain overcomes the energy cost that accompanies local structural fluctuation. In particular, one-dimensional (1D) systems have a propensity to be sensitive to these fluctuations as described by one of the maxims of condensed matter physics, *i.e.*, one chain does not make a crystal. Thus, the dynamical formation of active species and sites by these fluctuations is a key factor in establishing a microscopic model for chemical reactions at surfaces and nano-structured compounds.

IX-Q-1 Dynamic Formation of Reaction Sites at Nano-Structured One-Dimensional Surface Compounds

MATSUMOTO, Yoshiyasu; NAKAGOE, Osamu[1]; WATANABE, Kazuya[1]; TAKAGI, Noriaki[1]
([1]GUAS)

[*Proc. SPIE* **5223**, 232–240 (2003)]

It is well known that the adsorption of O on Ag(110) results in the formation of quasi-1D structures, AgO chains, accompanied by the mass transfer of substrate atoms.

AgO chains arrange periodically to form (n×1) (n = 2 ~ 7) depending on the fractional O coverage due to repulsive inter-chain interactions. Scanning tunneling microscopy is utilized to investigate the structural changes of AgO chains on clean and carbidic-carbon containing Ag(110) surfaces under UV photoirradiation and CO exposure. Although AgO chains are arranged with the (2×1) structure on both of the surfaces, AgO chains are bundled to make the (2×1) bands on the C-containing surface, whereas they make much larger domains on the entire surface of clean Ag(110). The photo-induced elimination of O in AgO chains occurs only on the C-containing surface. Kinetics of oxygen elimination by CO exposure are very different between the two surfaces. Oxygen coverage decreases steadily on the C-containing surface with CO exposure, whereas the reaction is accelerated in the lower O coverage range where AgO chains with (n×1) ($n \geq 4$) configurations show significant structural fluctuation. Comparison between the two surfaces and simulations based on the Ising model indicate that the acceleration of the reaction originates from the dynamical formation of active O adatoms by fluctuation of AgO chains.

IX-R Adsorbate Structure and Surface Chemistry on Well-Defined Surfaces

Surface reactions have been playing an important role in production of many useful compounds and also fabrication of electronic devices. In particular, investigations on the structures of adsorbates and their reactivity are the first step for understanding more complicated catalytic reactions. We investigate surface reactions and kinetics

by means of various techniques including temperature-programmed desorption (TPD), x-ray photoelectron spectroscopy (XPS), ultraviolet photoelectron spectroscopy (UPS), work function measurements, Auger electron spectroscopy (AES), infrared reflection absorption spectroscopy (IRAS) and scanning tunneling microscopy (STM).

IX-R-1 Reactivity of Molecular Oxygen: Conversion of Methanol to Formate at Low Temperatures on Pt(111)

SAWADA, Takeshi[1]; LIU, Zhengxin[2]; TAKAGI, Noriaki[1]; WATANABE, Kazuya[1]; MATSUMOTO, Yoshiyasu
([1]GUAS; [2]System Engineers' Co.)

[*Chem. Phys. Lett.* **392**, 334–339 (2004)]

The oxidation of methanol by molecular oxygen on a Pt(111) surface has been investigated by infrared reflection absorption spectroscopy and X-ray photoelectron spectroscopy. Formate is produced when the surface coadsorbed with molecular oxygen and methanol is annealed to 70 K; the temperature is far much lower than the dissociation temperature of molecular oxygen on a clean Pt(111) surface. The attractive interaction between the coadsorbates is postulated to lower a dissociation barrier of molecular oxygen. When a methanol-precovered Pt(111) surface is exposed to O_2, the sticking probability of O_2 decreases with increase of surface temperature and the major product of methanol oxidation is changed from formate to CO.

IX-S Structures, Stabilities and Physicochemical Properties of Organometallic Hybrid Clusters

Recently, metal clusters have gained much attention because they exhibit novel physicochemical properties that are beyond the prediction made by a dimensional scaling of those of the corresponding bulk. In this regard, metal clusters protected by thiolates or stabilized by polymers are promising candidates for elementary units of nano-scale devices. Our interests are focused on the following issues on the organometallic hybrid clusters: (1) a large-scale preparation of the subnanometer-sized clusters, (2) development of size–selection method, (3) determination of chemical compositions of size-selected clusters (*i.e.* the numbers of metal atoms and organic molecules), and (4) elucidation of effect of the core size, core shape, and interaction with organic molecules on stabilities, electronic structures, and chemical properties.

IX-S-1 Magic-Numbered Au_n Clusters Protected by Glutathione Monolayers (n = 18, 21, 25, 28, 32, 39): Isolation and Spectroscopic Characterization

NEGISHI, Yuichi; TAKASUGI, Yoshimitsu[1]; SATO, Seiichi[1]; YAO, Hiroshi[1]; KIMURA, Keisaku[1]; TSUKUDA, Tatsuya
([1]Univ. Hyogo)

[*J. Am. Chem. Soc.* **126**, 6518–6519 (2004)]

Small gold clusters (< 1 nm) protected by glutathione (GSH) monolayer were fractionated into six components by polyacrylamide gel electrophoresis (PAGE) and their chemical compositions were investigated by electrospray ionization (ESI) mass spectroscopy. The results demonstrate isolation of a series of magic-numbered gold clusters, $Au_{18}(SG)_{11}$, $Au_{21}(SG)_{12}$, $Au_{25\pm1}(SG)_{14\pm1}$, $Au_{28}(SG)_{16}$, $Au_{32}(SG)_{18}$, and $Au_{39}(SG)_{23}$. Their optical absorption spectra are highly structured with clear absorption onsets, which shift toward higher energies with reduction of the core size. These molecular-like gold clusters exhibit visible photoluminescence. The results reported herein provide helpful guidelines or starting points for further experimental and theoretical studies on structures, stabilities and optical properties of small gold MPCs.

IX-S-2 Effect of Thiolate Ligation on Stabilization and Electronic Structures of Subnanometer-Sized Gold Clusters

NEGISHI, Yuichi; NOBUSADA, Katsuyuki; TAKASUGI, Yoshimitsu[1]; SATO, Seiichi[1]; YAO, Hiroshi[1]; KIMURA, Keisaku[1]; TSUKUDA, Tatsuya
([1]Univ. Hyogo)

Small gold clusters protected by *N*-(2-mercaptopropionyl)glycine (MPG) and mercaptosuccinic acid (MSA) were prepared and isolated into several components by high-resolution PAGE. Mass analysis shows that the core sizes of the monolayer-protected gold clusters (gold MPCs) preferentially formed are dependent on the thiolate structures. This finding suggests the completion of the protecting shell plays an important role in stabilizing the gold MPCs with specific core sizes. In other words, it may be possible to prepare gold MPCs with any desired core size by proper design of the thiolate structures. Remarkable effect of thiolate ligation on the optical properties offers a new strategy toward fine-tuning of the fundamental properties of the MPCs through the degree of thiolate ligation as well as core size.

IX-S-3 Construction of Apparatus for Photodissociation and Surface-Induced Dissociation Studies of MPCs

NEGISHI, Yuichi; TSUKUDA, Tatsuya

Photo-dissociation and surface-induced dissociation of MPCs provide direct information on their thermodynamic stabilities. Such information also helps in the understanding of the origin of the preferential formation of certain-sized MPCs. Thus, we have improved our ESI-TOF mass spectrometer by introducing two components: a quadrupole ion trap and a reflectron coupled with an in-line MCP detector with a center hole. The continuous beam of the MPC ions formed in the ESI source is guided to the quadrupole ion trap. The ions accumulated in the trap are extracted into a primary TOF mass spectrometer typically operated at 10 Hz. The mass-selected cluster ions are irradiated by a pulsed laser or allowed to collide with the solid surface mounted at the end of the reflectron. The fragment ions generated are detected by a secondary TOF mass spectrometer.

IX-S-4 Construction of Low-Temperature Optical Spectroscopy System

NEGISHI, Yuichi; TSUNOYAMA, Hironori; TSUKUDA, Tatsuya

We have demonstrated that subnanometer-sized gold clusters exhibit clear structures in their optical spectra even at room temperature. In order to minimize the influence from vibration excitation of internal modes and/or isomers (if present), the measurement at low temperature is required. The system under construction is composed of a sample holder supported on a cold head (~22 K), a vacuum chamber, and a turbo-molecular pump. The system can be coupled to a spectrophotometer (HITACHI, U-2010) or a spectrofluorometer (JASCO, FP-6600) to obtain optical data of the neat film of the clusters.

IX-S-5 Heat Induced Long-Range Ordering of Small Gold Nanoparticles with Tunable Interparticle Spacings

KANEHARA, Masayuki[1]; KODZUKA, Etsushi[1]; NEGISHI, Yuichi; TSUKUDA, Tatsuya; TERANISHI, Toshiharu[1]
([1]Univ. Tsukuba)

The monodisperse Au nanoparticles smaller than 2 nm were prepared by the reduction of $HAuCl_4 \cdot 4H_2O$ in DMF/H_2O in the presence of a series of ligands, 2,6-bis(1'-(*n*-thioalkyl)benzimidazol-2-yl)pyridine (TC_nBIP, n = 8, 10, 12), and formed hexagonal close packed (*hcp*) two-dimensional (2D) superlattices with tunable interparticle spacings from 1.9 to 2.5 nm by the ligand length. Then we present the new methodology to fabricate the long range ordered 2D superlattices of 1.5-nm Au nanoparticles at the air-water interface, which includes a heat-induced rearrangement of *hcp* domains into long range ordered *hcp* superlattices stabilized by interligand π-π interaction. The large-scale *hcp* 2D superlattices of 1.5-nm Au nanoparticles were obtained, and advantageously transferable onto any substrate.

IX-S-6 Colloidal Gold Nanoparticles as Catalyst for Carbon–Carbon Bond Formation: Application to Aerobic Homocoupling of Phenylboronic Acid in Water

TSUNOYAMA, Hironori; SAKURAI, Hidehiro; ICHIKUNI, Nobuyuki[1]; NEGISHI, Yuichi; TSUKUDA, Tatsuya
([1]Chiba Univ.)

[*Langmuir* **20**, 11293–11296 (2004)]

Gold nanoparticles (ϕ < 2 nm) stabilized by poly(*N*-vinyl-2-pyrrolidone) (Au:PVP NPs) were prepared by reduction of $AuCl_4^-$ with $NaBH_4$ in the presence of PVP and characterized via array of methods including optical absorption spectroscopy, TEM, XRD, XANES, EXAFS, and XPS. It is found for the first time that the Au:PVP NPs act as catalyst toward homocoupling reactions of phenylboronic acid in water under aerobic conditions. Suppression of the biphenyl formation under anaerobic condition indicates that molecular oxygen dissolved in water is intimately involved in the coupling reactions. Effect of the particle size and the PVP coordination upon the catalytic activity is discussed.

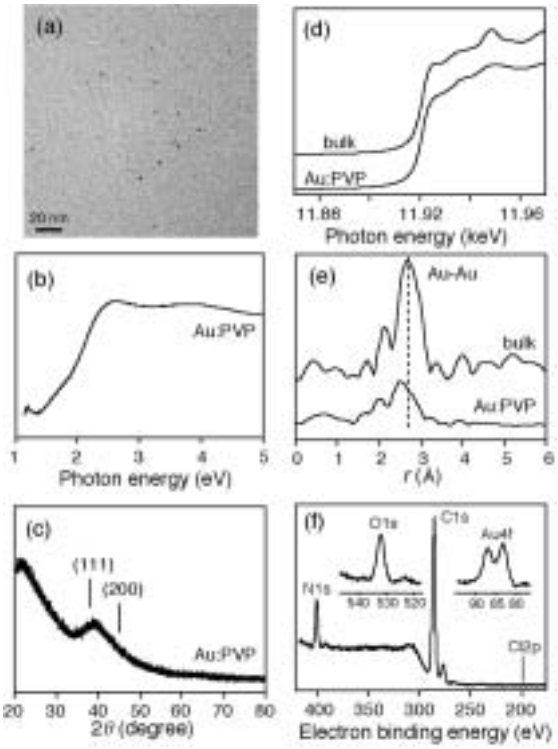

Figure 1. (a) TEM image, (b) optical absorption spectrum, (c) XRD profile, (d) Au L_3-edge XANES, (e) FT-EXAFS, (f) XPS of Au:PVP(K-30).

Table 1. Homocoupling Reactions of Phenylboronic Acid in Water Catalyzed by Au:PVP NPs[a].

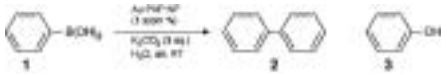

entry	catalyst	yield (%)[b]			d (nm)[d]
		1[c]	**2**	**3**	
1	Au:PVP(K-15)	16	62	22	3.1±0.7
2	Au:PVP(K-30)	3	72	23	2.9±0.4
3	Au:PVP(K-90)	trace	64	35	3.1±0.5
4[e]	Au:PVP(K-30)	>99	trace	trace	–
5	recovered from #2[f]	26	61	13	3.4±0.5
6	recovered from #5[f]	43	49	8	3.4±0.6

[a]The reactions were carried out at room temperature under air for 24 h. [b]Estimated from NMR analysis. [c]Detected as anhydride. [d]Particle diameter after the reaction determined by TEM measurement. [e]The reaction was carried out under nitrogen. [f]The Au:PVP NPs were collected by centrifugal ultrafiltration by a filter with10 kDa cutoff.

IX-S-7 Fabrication of Model Catalytic System by Use of Monolayer-Protected Metal Clusters as Precursor

TSUNOYAMA, Hironori; NEGISHI, Yuichi; TSUKUDA, Tatsuya

Metal clusters supported on a surface have been regarded as an ideal model for the study of heterogeneous catalysts.[1)] In these studies, metal clusters with a given size were softly deposited on the surface, and

the catalytic activity was investigated as a function of the cluster size. However, following difficulties are encountered in this approach: (1) the clusters tend to aggregate at high coverage, (2) the structures of the clusters deposited on a surface may not be uniform because of isomers present in the beam or surface-induced structural rearrangement. In order to circumvent these difficulties, we have been developing a new scheme to fabricate an ordered array of size-selected metal clusters. An ordered array of size-selected MPCs is transferred to a solid substrate by using a Langmuir-Brodgett technique. As an initial step, we prepared the monolayer of alkanethiolate-protected gold clusters on a carbon-coated copper grid. In the monolayer obtained, the gold MPCs are arranged regularly with interparticle distance determined by the thickness of the thiolate monolayer.[2)] The substrate is subsequently transferred into a UHV chamber which accommodates a magnetron-type plasma source. The organic layer of the MPCs is etched by exposure of the oxygen and/or hydrogen plasma. The structures of the resulting clusters are characterized by XPS and AFM. The activity of the model catalysts thus prepared is investigated in situ by means of thermal desorption spectroscopy.

References

1) A. Sanchez, S. Abbet, U. Heiz, W. -D. Schneider, H. Hakkinen, R. N. Barnett and U. Landman, *J. Phys. Chem. A* **103**, 9573 (1999).
2) P. Liljeroth, D. Vanmaekelbergh, V. Ruiz, K. Kontturi, H. Jiang, E. Kauppinen and B. M. Quinn, *J. Am. Chem. Soc.* **126**, 7126 (2004).

IX-T Fundamental Study on Electrostatic Manipulation of Biomolecules and Its Application to Gene Analysis

Since conventional DNA sequencing method can determine up to 1000 base pairs at one time, longer DNA must be cut into small fragments. However, order information among these fragments is inevitably lost resulting in tremendous post sequencing process to do a puzzle. To cope with the problem, we have studied DNA sequencing method based on one-by-one DNA handling. The method includes (1) electrostatic manipulation of genomic DNA, (2) fixation in a stretched from, (3) cut from the terminus, (4) recovery and amplification of the fragments.

IX-T-1 On-Demand Mixing Droplet Spotter for Preparing Picoliter Droplets on Surfaces

YOGI, Osamu[1]; KAWAKAMI, Tomonori[1]; MIZUNO, Akira
([1]Hamamatsu Photonics K. K.)

[*Anal. Chem.* **76**, 2991–2996 (2004)]

An on-demand mixing droplet spotter for generating and mixing picoliter droplet has been developed for ultrasmall reaction vessels. The droplets were generated by appling a ~500 V, ~2 ms pulsed voltage to the tips of capillary tubes (o.d. ~20 μm; i.d. ~12 μm) filled with solution. The mixing process was achieved using electrostatic force. The initial droplet was formed by applying the pulsed voltage between one capillary and the substrate, and the second jet of the other solution was generated from the other capillary and collided with the initial droplet automatically because the electric field lines concentrated on the initial droplet. Using this mixing process, a microarray having a concentration gradient was obtained by spotting ~6 pL droplets on a surface with a density of one spot per 75 × 75 μm^2.

IX-T-2 Ice-Water Interface Migration by Temperature Controlling for Stretching of DNA Molecules

KOMATSU, Jun[1]; NAKANO, Michihiko[1]; KURITA, Hirofumi[1]; TAKASHIMA, Kazunori[1]; KATSURA, Shinji[1]; MIZUNO, Akira[2]
([1]Toyohashi Univ. Tech.; [2]IMS and Toyohashi Univ. Tech.)

[*J. Biomol. Struct. Dyn.* accepted]

This report shows a new DNA stretching method using migration of an ice-water interface. DNA molecules were stretched accompanying the migration of the solid-liquid interface and immobilized in frozen area. This simple method needs no chemical modification to keep DNA in the stretched form. For full stretching of DNA molecules, one terminus of the DNA molecules were anchored on silanized substrate. The anchored DNA molecules were stretched by freezing the DNA solution. The stretched DNA molecules were observed after sublimation of the frozen solution keeping its stretched form on silanized surface which had no attractive interaction with DNA molecules except for the SH-modified terminus in solution. An infrared (IR) laser beam was introduced to a frozen DNA solution through an objective lens for local area melting of the solution. Scanning of the laser irradiation caused stretching and enclosing of DNA molecules in the frozen area followed by migration of the solid-liquid interface.

IX-T-3 Activation of Restriction Enzyme by Electrochemically Released Magnesium Ion

KATSURA, Shinji[1]; HARADA, Noriaki[1]; MAEDA, Yukihiro[1]; KOMATSU, Jun[1]; MATSUURA, Shunichi[1]; TAKASHIMA, Kazunori[1]; MIZUNO, Akira[2]
([1]Toyohashi Univ. Tech.; [2]IMS and Toyohashi Univ. Tech.)

[*J. Biosci. Bioeng.* accepted]

Observation and cutting of DNA molecules at intended positions permit several new experimental methods that are completely different from conventional molecular biology methods; therefore several cutting methods have been proposed and studied. In this paper, a new cutting method for a DNA molecule by localizing the activity of a restriction enzyme is presented. Since most restriction enzymes require magnesium ions for their activation, local restriction enzyme activity can be controlled by the local concentration of magnesium ions. Applying a dc voltage to a needle electrode of metallic magnesium made it possible to control the local magnesium ion concentration at the tip of the needle. The restriction enzyme was activated only when magnesium ions were electrochemically supplied.

IX-U Electronic Structure and Collision Dynamics of Atoms and Molecules Studied by Electron Impact at Large Momentum Transfer

Binary (e,2e) or electron momentum spectroscopy (EMS) is a high-energy electron-impact ionization experiment in which kinematics of all the electrons are fully determined by coincident detection of the two outgoing electrons. The method enables us to look at individual molecular orbitals in momentum space, based on the so-called electron Compton scattering. However, EMS has long been plagued by the fact that the present experiments measure averages over all orientations of gaseous targets. The spherical averaging results in enormous loss of versatile information on electronic structure, in particular that on anisotropy of the target wavefunction. Consequently, one must be content to use EMS only as a stringent test for the target wavefunction model employed. Under these historical circumstances, we have successfully developed an electron-electron-fragment ion triple coincidence apparatus that makes it possible to carry out molecular frame EMS experiments for the first time, opening up the possibilities for detailed studies of bound electronic wavefunctions of molecules.

IX-U-1 (e,2e) Ionization-Excitation of H_2

TAKAHASHI, Masahiko[1]; KHAJURIA, Yugal; UDAGAWA, Yasuo[2]
([1]IMS and Tohoku Univ.; [2]Tohoku Univ.)

[*Phys. Rev. A* **68**, 042710 (7 pages) (2003)]

Binary (e,2e) measurements are reported for simultaneous ionization-excitation processes of H_2. The experiments were performed at impact energies of 1200, 1600 and 2000 eV using an energy- and momentum-dispersive spectrometer. Momentum profiles for transitions to the $2s\sigma_g$ and $2p\sigma_u$ excited final ion states are presented as normalized intensities relative to the cross section of the primary ionization to the $1s\sigma_g$ ground ion state. The results are compared with theoretical calculations of Lermer *et al*. [*Phys. Rev. A* **56**, 1393 (1997)] using the first-order plane-wave impulse approximation. Certain features of the discrepancies between experiment and theory can be explained by incorporating contributions from the second-order two-step mechanisms into the (e,2e) cross sections. Furthermore, the present results suggest that $2s\sigma_g$ and $2p\sigma_u$ cross sections approach their high-energy limits in different ways.

IX-U-2 Electron Momentum Spectroscopy of N_2O

KHAJURIA, Yugal; TAKAHASHI, Masahiko[1]; UDAGAWA, Yasuo[2]
([1]IMS and Tohoku Univ.; [2]Tohoku Univ.)

[*J. Electron Spectrosc. Relat. Phenom.* **133**, 113–121 (2003)]

An electron momentum spectroscopy study of the outer valence orbitals of N_2O is reported. The experiments were performed at impact energies of 1000, 1200, 1600 and 1800 eV by using a recently developed multichannel (e,2e) spectrometer. The experimental momentum profiles are compared with each other to examine their impact energy dependence. The results are used for comparisons with Hartree-Fock (HF) and density functional theory (DFT) calculations using various basis sets. The DFT and HF calculations with large basis sets are in good agreement with the measured electron momentum profiles, with the exception of that of the 6σ orbital for which the HF method underestimates the cross sections in the low momentum region.

IX-U-3 Triple Differential Cross-Section of $Ne(2s^2)$ in Coplanar to Perpendicular Plane Geometry

CHEN, Li Q.[1] ; KAHJRIA, Yugal; CHEN, Xian J.[1]; XU, Ka Z.[1]
([1]USTC)

[*Eur. Phys. J. D* **26**, 141–146 (2003)]

The distorted wave Born approximation (DWBA) with spin average static exchange potential has been used to calculate the triple differential cross sections (TDCSs) for $Ne(2s^2)$ ionization by electron impact in the coplanar to perpendicular plane geometry at 110.5 eV incident energy. The present theoretical results at gun angles $\Psi = 0°$ (coplanar symmetric geometry) and $\Psi = 90°$ (perpendicular plane geometry) are in satisfactory agreement with the available experimental data. A deep interference minimum appears in the TDCS in the coplanar symmetric geometry and a strong peak at a scattering angle $\xi = 90°$ caused by the single collision mechanism has been observed in the perpendicular plane geometry. The TDCSs at the gun angles $\Psi = 30°$, and $\Psi = 60°$ are predicted.

IX-U-4 A High Sensitivity Electron Momentum Spectrometer with Two-Dimensional Detectors and Electron Momentum Distributions of Several Simple Molecules

TAKAHASHI, Masahiko[1]; UDAGAWA, Yasuo[2]
([1]IMS and Tohoku Univ.; [2]Tohoku Univ.)

[*J. Electron Spectrosc. Relat. Phenom.* **137-40**, 387–391 (2004)]

Electron momentum spectroscopy (EMS) makes it

possible to examine orbital patterns of individual molecular orbitals in momentum space. A new spectrometer for electron-electron coincidence experiments for EMS has been developed to obtain orbital patterns quantitatively. Using a spherical analyzer and position-sensitive two-dimensional detectors combined with fast electronics, simultaneous measurements of energy and angular correlations between the two outgoing electrons can be made. This spectrometer features high sensitivity and an ease of changing impact energies. Details of the apparatus are described and impact energy dependence of electron momentum distributions of the HOMO of H_2 and biacetyl are compared.

IX-U-5 Practical Means for the Study of Electron Correlation in Atoms

VAN BOEYEN, Roger W.[1]; WATANABE, Noboru[2]; DOERING, John P.[1]; MOORE, John H.[3]; COPLAN, Michael A.[3]
([1]Johns Hopkins Univ.; [2]IMS and Tohoku Univ.; [3]Univ. Maryland)

[*Phys. Rev. Lett.* **92**, 223202 (4 pages) (2004)]

Electron correlation is basic to the understanding of a diverse range of physical and chemical phenomena, yet, there have been no direct measurements of the correlated motion of electrons. Measurement of the correlated momenta of atomic electrons is possible via electron-impact double ionization provided that the ionizing collisions are both impulsive and binary, and the three-body scattering mechanism is known. The results reported here satisfy these conditions, and a practical means for the study of atomic electron correlation through measurement of two-electron momentum densities is presented.

IX-U-6 Development and Use of a Multichannel (e,2e) Spectrometer for Electron Momentum Densities of Molecules

TAKAHASHI, Masahiko[1]; UDAGAWA, Yasuo[2]
([1]IMS and Tohoku Univ.; [2]Tohoku Univ.)

[*J. Phys. Chem. Solids* **65**, 2055–2059 (2004)]

We have developed an (e,2e) spectrometer with the introduction of modern multiparameter techniques. In particular, the high sensitivity achieved by simultaneous detection in energy and momentum is remarkable, opening up the possibilities of more precise and more advanced studies on the electronic structure of atoms and molecules. To illustrate some of the features, an overview of our recent results is presented. Highlights are applications to collision dynamics of H_2 and development of a method for a complete three-dimensional mapping of electron momentum densities in gaseous molecules. Both of these studies are based on the high sensitivity of the spectrometer.

IX-U-7 Electron Momentum Spectroscopy of Valence Satellites of Neon

WATANABE, Noboru[1]; KHAJURIA, Yugal; TAKAHASHI, Masahiko[1]; UDAGAWA, Yasuo[2]
([1]IMS and Tohoku Univ.; [2]Tohoku Univ.)

[*J. Electron Spectrosc. Relat. Phenom.* in press]

Electron momentum spectroscopy (EMS) study of the neon valence satellites is reported. The experiments were performed at impact energies of 1250, 1450 and 1670 eV using a multichannel spectrometer that features high sensitivity. Binding energy spectra up to 100 eV and momentum profiles for the $2p^{-1}$ and $2s^{-1}$ primary transitions as well as the satellites are presented. The results are used to examine impact energy dependence of the relative intensities and shapes of the satellite momentum profiles. The results are also used to determine symmetries and spectroscopic factors of the satellites, and are compared with the previous experiments by EMS and photoelectron spectroscopy and sophisticated theoretical calculations. The present study has largely resolved controversies in the previous studies.

IX-U-8 Observation of Molecular Frame (e,2e) Cross Section Using an Electron-Electron-Fragment Ion Triple Coincidence Apparatus

TAKAHASHI, Masahiko[1]; WATANABE, Noboru[1]; KHAJURIA, Yugal; NAKAYAMA, Kazuya[2]; UDAGAWA, Yasuo[2] ; ELAND, John H. D.[3]
([1]IMS and Tohoku Univ.; [2]Tohoku Univ.; [3]IMS and Oxford Univ.)

[*J. Electron Spectrosc. Relat. Phenom.* **141**, 83–93 (2004)]

An apparatus for electron-electron-fragment ion triple coincidence experiments has been developed to examine binary (e,2e) scattering reaction in the molecular frame. In the axial recoil limit of fragmentation of the residual ion, measurements of vector correlations among the three charged particles are equivalent to (e,2e) experiments with fixed-in-space molecules. Details and performance of the apparatus are reported, together with preliminary result of collision dynamics study on ionization-excitation processes of fixed-in-space H_2 molecules. We believe that this is the first observation of molecular frame (e,2e) cross sections.

IX-U-9 (e,3e) Collisions on Mg in the Impulsive Regime Studied by Second Born Approximation

WATANABE, Noboru[1]; COOPER, John W.[2]; VAN BOEYEN, Roger W.[3]; DOERING, John P.[3]; MOORE, John H.[2]; COPLAN, Michael A.[2]
([1]IMS and Tohoku Univ.; [2]Univ. Maryland; [3]Johns Hopkins Univ.)

[*J. Phys. B: At., Mol. Opt. Phys.* submitted]

Five-fold differential cross sections for electron-impact double ionization of the 3s electrons of magnesium have been calculated in the second Born approximation in the impulsive regime. Comparing

these results with calculations carried out in the first Born approximation demonstrates the dominant contribution of the second Born term. The second Born calculation shows that contribution of the two-step 2 (TS2) process becomes large under the condition where sequential binary collisions on the Bethe ridge can occur. The effect of electron correlation in the initial target state is also examined by using a configuration interaction wavefunction.

IX-U-10 Molecular Frame (e,2e) Cross Sections Observed for Ionization-Excitation Processes of H_2

TAKAHASHI, Masahiko[1]; WATANABE, Noboru[1]; KHAJURIA, Yugal; UDAGAWA, Yasuo[2]; ELAND, John H. D.[3]
([1]IMS and Tohoku Univ.; [2]Tohoku Univ.; [3]IMS and Oxford Univ.)

[*Phys. Rev. Lett.* submitted]

We report on first kinematically complete experiment of (e,2e) scattering by molecules using the electron-electron-fragment ion triple coincidence technique. Vector correlations among the two outgoing electrons and the fragment ion have been measured for ionization-excitation processes of H_2. The results are used to obtain (e,2e) cross section in the molecular frame and to observe the collision stereodynamics, the phenomenon that has never been explored so far.

IX-U-11 Double Ionization of He by (e,3-1e) at Large Momentum Transfer

KHAJURIA, Yugal; WATANABE, Noboru[1]; TAKAHASHI, Masahiko[1]; UDAGAWA, Yasuo[2]; POPOV, Yuri V.[3]; KOZAKOV, Konstantin A.[3]; VINITSKY, Pavel S.[3]; CHULUUNBAATAR, Ochbadrakh[4]
([1]IMS and Tohoku Univ.; [2]Tohoku Univ.; [3]Moscow State Univ.; [4]JINR)

[*Phys. Rev. A* to be submitted]

The present (e,3-1e) experiment aims at investigating double ionization at large momentum transfer that would provide direct information on electron correlation in the target initial state. The (e,3-1e) method involves coincident detection of the two fast outgoing electrons while keeping the slow outgoing electron undetected. It has been found from comparison between experiment and theory that (e,3-1e) momentum profile is very sensitive to the target electron correlation, as expected. In fact, the experimental profile shape is reproduced well by first Born calculations using highly correlated wavefunctions. However, there is noticeable intensity difference between experiment and theory. The calculation underestimates the experimental cross sections significantly by a few times of magnitude, suggesting need of incorporating higher Born terms and/or more accurate description of correlated electron pair in helium.

IX-U-12 (e,2e) Study on Distorted Wave Effects in the Xe $4d^{-1}$ Ionization Process

KHAJURIA, Yugal; WATANABE, Noboru[1]; YOSHINO, Tae[2]; SAKAI, Yasuhiro[2]; TAKAHASHI, Masahiko[1]; UDAGAWA, Yasuo[3]
([1]IMS and Tohoku Univ.; [2]Toho Univ.; [3]Tohoku Univ.)

[*J. Phys. B: At., Mol. Opt. Phys.* to be submitted]

Momentum profiles for the Xe $4d^{-1}$ ionization process have been studied by means of binary (e,2e) at various impact energies. The results are found to exhibit considerable intensity near the momentum origin that the plane-wave impulse approximation (PWIA) theory can not predict. The discrepancy from PWIA is substantially reduced by distorted-wave theory. Furthermore, momentum profiles for the core $4d_{3/2}$ and $4d_{5/2}$ orbitals of Xe are compared with associated theoretical momentum profiles generated using Dirac-Fock wavefunctions to investigate relativistic effects in the ionization process.

IX-U-13 The Impact Energy Dependence of Momentum Profile of Acetone and Comparison with Theory at Its High-Energy Limit

CHO, Tegyon[1]; KHAJURIA, Yugal; WATANABE, Noboru[2]; TAKAHASHI, Masahiko[2]; UDAGAWA, Yasuo[1]
([1]Tohoku Univ.; [2]IMS and Tohoku Univ.)

[*J. Phys. B: At., Mol. Opt. Phys.* to be submitted]

We report an electron momentum spectroscopy study of the outermost orbital of acetone. The experiments were performed at impact energies of 800, 1200, 1600 and 2000 eV by using a recently developed multichannel (e,2e) spectrometer. The results at 2000 eV are compared with plane-wave impulse approximation calculations using Hartree-Fock (HF) and density functional theory (DFT). While the DFT calculations reproduce the observations better than HF, noticeable discrepancy between experiment and theory still remains.

IX-V Electronic Structure and Collision Dynamics of Atoms and Molecules Studied by Photon Impact

The group takes another, photon-impact, approach to issues of electronic structure and collision dynamics, since photon-impact and electron-impact or photoelectric effects and Compton scattering are complementary to each other.

IX-V-1 N 1s Photoionization Cross Sections of the NO Molecules in the Shape Resonance Region

HOSAKA, Kouichi[1]; ADACHI, Junichi[1,2]; TAKAHASHI, Masahiko[3]; YAGISHITA, Akira[1,2]
([1]Univ. Tokyo; [2]KEK-PF; [3]IMS and Tohoku Univ.)

[*J. Phys. B: At., Mol. Opt. Phys.* **36**, 4617–4629 (2003)]

The N 1s partial photoionization cross sections of NO leading for the $^3\Pi$ and $^1\Pi$ ionic states have been measured in the shape resonance region for the first time. The twin local maxima in the cross sections have been tentatively assigned, based on the simple models for the photoabsorption intensities and for the branching ratio of the $^3\Pi$ and $^1\Pi$ ionic states from the σ^* shape resonance state.

IX-V-2 Shape-Resonance-Enhanced Vibrational Effects in the Angular Distributions of C 1*s* Photoelectrons from Fixed-in-Space CO Molecules

ADACHI, Junichi[1,2]; HOSAKA, Kouichi[1]; FURUYA, Shuusaku[3]; SOEJIMA, Kouich[3]; TAKAHASHI, Masahiko[4]; YAGISHITA, Akira[1,2]; SEMENOV, Sergei K.[5]; CHEREPKOV, Nikolai A.[5]
([1]Univ. Tokyo; [2]KEK-PF; [3]Niigata Univ.; [4]IMS and Tohoku Univ.; [5]State Univ. Aerospace Instrum.)

[*Phys. Rev. Lett.* **91**, 163001 (4pages) (2003)]

Angular distributions of C1*s* photoelectrons from fixed-in-space CO molecules have been measured with vibrational resolution. A strong dependence of the angular distributions on the vibrational states of the residual molecular ion has been found for the first time in the region of the shape resonance. Calculations in the relaxed core Hartree-Fock approximation have reproduced the angular distributions fairly well in the general shapes of the angular distributions due to the correct description of nuclear motion as an average of the internuclear-distance-dependent dipole amplitudes.

IX-V-3 Photoelectron-Photoion-Photoion Coincidence in Ar Dimers

FANIS, Albert De[1,2]; OURA, Masaki[3]; SAITO, Norio[4]; MACHIDA, Masatake[3,5]; NAGOSHI, Mitsuru[5]; KNAPP, Alexandra[6]; NICKLES, Jurgen[6]; CZASCH, Achim[6]; DÖRNER, Reinhard[6]; TAMENORI, Yusuke[1]; CHIBA, Hisashi[7]; TAKAHASHI, Masahiko[7]; ELAND, John H. D.[8]; UEDA, Kiyoshi[2]
([1]JASRI; [2]Tohoku Univ.; [3]RIKEN; [4]Natl. Metrology Inst.; [5]Himeji Inst. Tech.; [6]Univ. Frankfurt; [7]IMS and Tohoku Univ.; [8]Oxford Univ.)

[*J. Phys. B: At., Mol. Opt. Phys.* **37**, L1–L8 (2004)]

Photoelectron-photoion-photoion coincidence momentum imaging was applied to study 2p photoemission from Ar dimers. We present measurements of the kinetic energy released in fragmentation of Ar_2^{++}, angular distributions of energetic fragments, angular distributions of photoelectrons in the laboratory frame and in the molecular frame. The mean kinetic energy of fragment Ar^+ ions, 2.2 eV, is larger than the value estimated from the Coulomb explosion model with the equilibrium Ar–Ar distance. No significant differences between the photoelectron angular distributions of monomers and dimers can be found in the laboratory frame. The photoelectron angular distributions of dimers in the molecular frame show a minimum for electron emission along the dimer axis at low energies (1.2 and 3.4 eV) and become isotropic at higher kinetic energies.

IX-V-4 Multiplet-Specific N 1*s* Photoelectron Angular Distributions from the Fixed-in-Space NO Molecules

HOSAKA, Kouichi[1]; ADACHI, Junichi[1,2]; TAKAHASHI, Masahiko[3]; YAGISHITA, Akira[1,2]; LIN, Ping[4]; LUCCHESE, Robert R.[4]
([1]Univ. Tokyo; [2]KEK-PF; [3]IMS and Tohoku Univ.; [4]Texas A&M Univ.)

[*J. Phys. B: At., Mol. Opt. Phys.* **37**, L49–L55 (2004)]

Angular distributions of multiplet-specific N 1*s* photoelectrons from the fixed-in-space NO molecules have been measured for the first time. The dynamics of the σ^* shape resonance appeared in the channel leading to the $^3\Pi$ and $^1\Pi$ ionic states has been made clear from the analyses of the angular distributions. Multiplet-specific multichannel calculations have reproduced the observed angular distributions fairy well.

IX-V-5 Angular Distributions of Vibrationally Resolved C 1*s* Photoelectrons from Fixed-in-Space CO Molecules: Vibrational Effect in the Shape-Resonant C 1*s* Photoionization of CO

ADACHI, Junichi[1,2]; HOSAKA, Kouichi[1]; FURUYA, Shuusaku[3]; SOEJIMA, Kouich[3]; TAKAHASHI, Masahiko[4]; YAGISHITA, Akira[1,2];

SEMENOV, Sergei K.[5]; CHEREPKOV, Nikolai A.[5]
([1]Tokyo Univ.; [2]KEK-PF; [3]Niigata Univ.; [4]IMS and Tohoku Univ.; [5]State Univ. Aerospace Instrum.)

[*J. Electron Spectrosc. Relat. Phenom.* **137-40**, 243–248 (2004)]

We have measured molecular-frame photoelectron angular distributions (MF-PAD) for the vibrationally resolved C1*s* photoelectron from CO molecule in the σ shape resonance region. The MF-PAD's for the v_f = 0, 1, and 2 levels in the C1*s* → εℓσ channel are apparently different each other at each incident photon energy. These MF-PAD's agree with the present theoretical results from the averaging the nuclear distance dependent dipole matrix elements with the relaxed core Hartree-Fock calculations. The present results show that the internuclear distance dependences of the phase and of the magnitude of the dipole matrix element play a crucial role in the C1*s* photoionization of CO.

IX-V-6 Coulomb Hole in N_2, CO and O_2 Deduced from X-Ray Scattering Cross Sections

WATANABE, Noboru[1]; KAMATA, Yohei[2]; YAMAUCHI, Kota[2]; UDAGAWA, Yasuo[2]; MÜLLER, Thomas[3]
([1]IMS and Tohoku Univ.; [2]Tohoku Univ.; [3]Res. Cent. Jülich)

[*Mol. Phys.* **102**, 649–657 (2004)]

Accurate total (elastic + inelastic) x-ray scattering cross sections $\sigma_{ee}(q)$ of N_2, CO and O_2 were measured by the use of the energy dispersive method up to a momentum transfer of q = 12 a.u. The radial electron pair distribution function $P(r_{12})$ was extracted from the cross sections. The Coulomb hole, defined as the difference between the exact $P(r_{12})$ and the corresponding function evaluated at Hartree-Fock limit, has been derived from experimental data for the first time. Comparison of multi reference configuration interaction (MRCI) and averaged quadratic coupled cluster (MR-AQCC) calculations indicate substantial shortcomings of MRCI due to the lack of size extensivity. The overall agreement with experiment is good but some differences between the theoretical and experimental results remain.

IX-V-7 Absolute Surface Coverage Measurement Using a Vibrational Overtone

PIPINO, Andrew C. R.[1]; HOEFNAGELS, Johan P. M.[2]; WATANABE, Noboru[3]
([1]Natl. Inst. Standards Tech.; [2]Eindhoven Univ. Tech.; [3]IMS and Tohoku Univ.)

[*J. Chem. Phys.* **120**, 2879–2888 (2004)]

Determination of absolute surface coverage with sub-monolayer sensitivity is demonstrated using evanescent-wave cavity ring-down spectroscopy (EW-CRDS) and conventional CRDS by employing conservation of the absolute integrated absorption intensity between gas and adsorbed phases. The first C–H stretching overtones of trichloroethylene (TCE), *cis*-dichloroethylene, and *trans*-dichloroethylene are probed using the idler of a seeded optical parametric amplifier having a 0.075 cm^{-1} line width. Polarized absolute adsorbate spectra are obtained by EW-CRDS using a fused-silica monolithic folded resonator having a finesse of 28500 at 6050 cm^{-1}, while absolute absorption cross sections for the gas-phase species are determined by conventional CRDS. A measure of the average transition moment orientation on the surface, which is utilized for the coverage determination, is derived from the polarization anisotropy of the surface spectra. Coverage measurement by EW-CRDS is compared to a mass-spectrometer-based surface-uptake technique, which we also employ for coverage measurements of TCE on thermally grown SiO_2 surfaces. To assess the potential for environmental sensing, we also compare EW-CRDS to optical waveguide techniques developed previously for TCE detection.

IX-V-8 Direct Observation of a Symmetry Lowering in Core-Electron Ionization for Highly Symmetric Molecules

HOSAKA, Kouichi[1]; ADACHI, Junichi[1,2]; GOLOVIN, Alexander V.[2]; TAKAHASHI, Masahiko[3]; TERAMOTO, Takahiro[1]; WATANABE, Noboru[3]; YAGISHITA, Akira[1,2]
([1]Tokyo Univ.; [2]KEK-PF; [3]IMS and Tohoku Univ.)

(*Nature* to be submitted)

The Jahn-Teller theorem governs stable structures of crystalline solids and molecules with an element of symmetry. This is because electro-vibrational (vibronic) coupling splits degenerate adiabatic-states by lowering the symmetry. The symmetry lowering occurs quite often in the ionization of a core electron of equivalent constituent-atoms for highly symmetric molecules since the core-hole states of those molecules are generally quasi-degenerate and therefore couple over non-totally symmetric vibrational modes. Such couplings, referred as quasi-Jahn-Teller couplings, have been clearly investigated for the most basic example of CO_2; the relation between the symmetry lowering and core-hole localization has been proved. The symmetry lowering which removes the equivalence of two oxygen atoms causes a fundamental quantum mechanical question; is it possible to decide whether the core hole is localized on the right oxygen atom or on the left? Here we report the direct observation of the symmetry lowering of the CO_2 induced by O1*s* photoionization.

IX-W Study of Electronic Structure of Organic Thin Film and Organic/Inorganic Interface

Organic semiconductors have gained increasing interest because of their highly potential uses in various molecular devices. To clarify the electronic processes at the organic/inorganic interface, various characterization techniques such as high-resolution ultraviolet photoemission spectroscopy (UPS) and near-edge x-ray absorption fine structure (NEXAFS) have been performed for organic thin film systems, because the origin of the energy position and the bandwidth of UPS spectra are keys to understand the interface properties such as the energy level alignment at the interface, intermolecular or molecule-substrate interactions, and carrier transport process. Energy, vibronic coupling and lifetime of a hole created in the highest occupied molecular orbital (HOMO) state in the organic thin film play a crucial role in the hole transport through the film and the electron injection from an electrode to the ionized molecule. The HOMO band in UPS spectra in principle involves such information about the hole, and thus offers a variety of key information that is necessary to unravel fundamental mechanism in carrier transport properties in organic devices.

IX-W-1 Impact of an Interface Dipole Layer on Molecular Level Alignment at an Organic-Conductor Interface Studied by UPS

KERA, Satoshi; YABUUCHI, Yousuke[1]; YAMANE, Hiroyuki[1]; SETOYAMA, Hiroyuki[1]; OKUDAIRA, K. Koji[1]; KAHN, Antoine[2]; UENO, Nobuo[1]
([1]Chiba Univ.; [2]Princeton Univ.)

[*Phys. Rev. B* **70**, 085304 (6 pages) (2004)]

The effect of an interface dipole layer on the energy level alignment at organic-conductor interfaces is studied on a copper phthalocyanine (CuPc) monolayer/electric dipole layer/graphite system *via* ultraviolet photoemission spectroscopy (UPS) and metastable atom electron spectroscopy (MAES). An oriented monolayer of the OTi-phthalocyanine molecule (OTiPc), which has an electric dipole moment, is grown on graphite to yield a well-defined dipole layer with the vacuum side negatively charged. The CuPc monolayer is sequentially deposited on the dipole layer kept at 123 K. This weakly interacting system made of a very thin organic layer on top of a very thin dipole layer is in thermodynamic equilibrium. The UPS data from the system grown with and without the interface dipole layer show that the binding energy of the highest occupied state of the CuPc monolayer decreases when the dipole layer is inserted. The binding energy shift is in excellent agreement with the increase in vacuum level energy of the graphite substrate upon deposition of the dipole layer. The results show that the Fermi level of the CuPc shifts toward the valence states when the interface dipole layer is inserted.

IX-W-2 HOMO-Band Fine Structure of OTi- and Pb-Phthalocyanine Ultrathin Films: Effects of the Electric Dipole Layer

YAMANE, Hiroyuki[1]; HONDA, Hiroyuki[1]; FUKAGAWA, Hirohiko[1]; OHYAMA, Mitsuharu[1]; HINUMA, Yoyo[1]; KERA, Satoshi; OKUDAIRA, K. Koji[1]; UENO, Nobuo[1]
([1]Chiba Univ.)

[*J. Electron Spectrosc.* **137-140**, 223–227 (2004)]

Ultraviolet photoelectron spectra were measured for titanyl- and lead-phthalocyanine ultrathin films prepared on graphite in order to study effects of the electric dipole layer on the organic energy levels. Each of these molecules has an electric dipole perpendicular to the molecular plane, and hence a well-defined electric dipole layer could be intentionally prepared by using oriented monolayer of these molecules. For as-grown films the observed highest occupied molecular orbital (HOMO) band consists of many peaks that could be assigned to different molecular orientations/aggregations. For well-oriented monolayer films obtained by annealing the as-grown films, we observed a very sharp HOMO band with two satellites for both molecules as for copper phthalocyanine. Difference of binding energy of HOMO bands between the oriented monolayer and the doublelayer in which molecular dipoles are cancelled was found to agree with the vacuum level shift for both molecules, leading to important conclusions that (1) the molecular energy level with respect to the substrate Fermi level is changed when the molecule is in the dipole-layer and (2) the binding-energy shift corresponds with the vacuum level shift.

IX-W-3 Photoelectron Fine Structures of Uppermost Valence Band for Well-Characterized ClAl-Phthalocyanine Ultrathin Film: UPS and MAES Study

KERA, Satoshi; YAMANE, Hiroyuki[1]; HONDA, Hiroyuki[1]; FUKAGAWA, Hirohiko[1]; OKUDAIRA, K. Koji[1]; UENO, Nobuo[1]
([1]Chiba Univ.)

[*Surf. Sci.* **566-568**, 571–578 (2004)]

Metastable atom electron spectroscopy was used to characterize monolayer formation of chloroaluminum phthalocyanine (ClAlPc) prepared on graphite. For as-grown film, molecules form island structure of staggered doublelayers on the substrate. By annealing the film, molecules diffuse to form a uniform monolayer where all the molecules are oriented flat with Cl atom directed to the vacuum. After the confirmation of the oriented monolayer formation, high-resolution ultraviolet photoelectron spectra were measured to study

effects of the molecular orientation on the energy levels. ClAlPc has an electric dipole perpendicular to the molecular plane, hence a well-defined electric dipole layer could be intentionally prepared by using the oriented monolayer. Difference of binding energies of HOMO bands between the oriented monolayer and the doublelayer was found to agree with the vacuum level shift, leading to a conclusion that the molecular energy level with respect to the substrate Fermi level is changed when the molecule is in the dipole-layer field.

IX-W-4 Study of Excited States of Fluorinated Copper Phthalocyanine by Inner Shell Excitation

OKUDAIRA, K. Koji[1]; SETOYAMA, Hiroyuki[1]; YAGI, Hideki[1]; MASE, Kazuhiko[2]; KERA, Satoshi; KAHN, Antoine[3]; UENO, Nobuo[1]
([1]Chiba Univ.; [2]AIST; [3]Princeton Univ.)

[*J. Electron Spectrosc.* **137-140**, 137–140 (2004)]

Near edge X-ray absorption fine structure (NEXAFS) spectra of hexadecafluoro copper phthalocyanine (FCuPc) films (thickness of 50 Å) on MoS_2 substrates were observed near the carbon (C) and fluorine (F) K-edges. From the analysis of the dependence of C and F K-edge NEXAFS spectra on the photon incidence angle (α), the average molecular tilt angle was determined to be 30°. The lowest and second lowest peaks in the F K-edge NEXAFS were assigned to the transition to σ^*. In the ion time-of-flight mass spectra of FCuPc excited by photons near the F K-edge, F^+, CF^+, and CF_3^+ ions were mainly observed. These results indicate that C–C bonds as well as C–F bonds are broken by the photon irradiation. From the analysis of the partial ion yield spectra of F^+ and CF^+ near the F K-edge, the lowest and second lowest peaks in the F K-edge NEXAFS spectra could be assigned to transitions to σ(C–F)* and σ(C–C)*, respectively.

IX-W-5 Simulation Study of Angle-Resolved Photoemission Spectra and Intramolecular Energy-Band Dispersion of a PTFE Oligomer Film

YOSHIMURA, Daisuke[1]; ISHII, Hisao[2]; OUCHI, Yukio[3]; MIYAMAE, Takayuki[4]; HASEGAWA, Shinji[5]; OKUDAIRA, K. Koji[6]; UENO, Nobuo[6]; SEKI, Kazuhiko[3]
([1]IMS and Nagoya Univ.; [2]Tohoku Univ.; [3]Nagoya Univ.; [4]AIST; [5]Fuji Xerox; [6]Chiba Univ.)

[*J. Chem. Phys.* **120**, 10753–10762 (2004)]

Theoretical simulations of the angle-resolved ultraviolet photoemission spectra for the oligomer of poly (tetrafluoroethylene) ($(CF_2)_n$; PTFE) was performed using the independent-atomic-center (IAC) approximation combined with *ab initio* molecular orbital (MO) calculations. Previously observed normal-emission spectra for the end-on oriented sample (with long-chain axis being perpendicular to the surface) showed the incident photon-energy ($h\nu$) dependence due to the intramolecular energy-band dispersion along the one-dimensional chain,[1)] and the present simulations successfully reproduced this $h\nu$-dependence of the observed spectra. We employed the experimentally observed helical structure for PTFE oligomers for the simulations. We also calculated the density of states (DOS) for the planar zigzag structure, and examined the changes in the electronic structure due to the difference in the molecular structure by comparing the DOS for the helical and planar zigzag structures. Only little change in the DOS was found between these structures, showing little change of the electronic structure between these conformations. We also evaluated the inner-potential V_0, which is the parameter defining the energy origin of the free-electron-like final state, and checked the validity of the value of –10 eV estimated in our previous study using the experimentally observed $h\nu$-dependence of the peak intensity.[1)] The estimation of V_0 was performed by pursuing the best agreement between the energy-band dispersion ($E = E(\boldsymbol{k})$) relation along the chain direction obtained from the simulated spectra and the experimentally deduced one. An excellent agreement in the topmost band was achieved when the assumed inner potential V_0 was set about zero. This value of V_0 is much different from the value of $V_0 = -10$ eV in the previous study, suggesting the invalidity of the previous assumption at the estimation of V_0 from the peak intensity variation with $h\nu$. Using the presently obtained V_0, we could derive more reliable $E = E(\boldsymbol{k})$ dispersion relation from the observed ARUPS spectra. The comparison of this newly derived relation gave good agreement with theoretically calculated $E = E(\boldsymbol{k})$ relations, in contrast to the poor agreement for the previous results with $V_0 = -10$ eV.

Reference

1) T. Miyamae, S. Hasegawa, D. Yoshimura, H. Ishii, N. Ueno and K. Seki, *J. Chem. Phys.* **112**, 3333–3338 (2000).

IX-X Effects of High Magnetic Field on Chemical and Physical Processes

We have studied the effects of high magnetic field on chemical reaction and physical processes of diamagnetic and paramagnetic materials to unravel the mechanisms of the interaction of matter and magnetic field and to develop unique methods controlling chemical and physical processes and improving chemical and physical properties of functional materials. Currently we are using a vertical superconducting magnet which can generate high magnetic fields (15 T, 1500 T^2/m) in a 40 ϕ bore tube. Last year, we have succeeded, for the first time, to induce 3-dimensional morphological chirality in zinc silicate membrane tube using a high magnetic field. This year, from *in situ* observation, we have verified the mechanism. The Lorentz force on ions induces remarkable convection of a solution in silicate garden reaction. Some other interesting effects of magnetic fields were also studied.

IX-X-1 3-Dimensional Morphological Chirality Induction in Silicate Garden Reaction Using a Magnetic Field

DUAN, Wenyong[1]; UECHI, Ichiro[1]; KITAMURA, Shu[2]; FUJIWARA, Yoshihisa[2]; TANIMOTO, Yoshifumi[1]
([1]IMS and Hiroshima Univ.; [2]Hiroshima Univ.)

We have reported that *three-dimensional morphological chirality* can be induced in silicate membrane tubes formed from the reaction of sodium silicate aqueous solution and zinc sulfate crystals by using vertical magnetic fields (5–15 T).[1)] In magnetic fields right-handed helical tubes grow along the inner surface of the vessel wall, whereas left-handed tubes grow along the outer surface of the glass rod placed in the vessel. In order to examine whether this new effect is generally observed in silicate garden reaction, we have studied many silicate garden reactions using different metal salt crystals. Morphological chirality is induced in membrane tubes prepared from magnesium chloride, copper sulfate, manganese sulfate, and iron sulfate crystals, indicating that this effect is common in silicate garden reaction. Paramagnetism of metal ion such as copper ion is unimportant for chirality induction, indicating that magnetic force cannot induce morphological chirality. Furthermore, in magnetic fields membrane tubes grown apart from the vessel wall are twisted to the opposite direction to those grown along the inner surface of the wall, as shown in Figure 1.

In order to verify the mechanism, *in situ* observation of the reaction using magnesium salt crystals was carried out in a bore tube of a magnet. At zero field, no convection of sodium silicate aqueous solution was observed regardless of magnesium chloride crystals. In the presence of 15 T vigorous convection was observed only when the crystals were added to the solution. It was shown that helical tubes near the vessel wall grow along the convection, whereas tubes apart the wall are twisted by the convection. It is now verified that Lorentz force on ions blowing out from the membrane tubes induces remarkable convection of the bulk solution.

Reference
1)I. Uechi, A. Katsuki, L. Dunin-Barkovskiy and Y. Tanimoto, *J. Phys. Chem. B* **108**, 2527–2530 (2004).

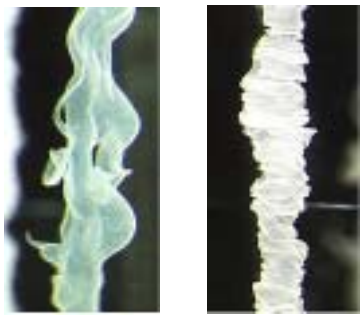

Figure 1. Photos of zinc silicate membrane tubes grown apart from a vessel wall at zero field (left) and 12 T (right). (Magnification; 175)

IX-X-2 *In Situ* Observation of the Effects of a High Magnetic Field on the Growth of Silver Dendrites

KATSUKI, Akio[1]; TANIMOTO, Yoshifumi
([1]Shinshu Univ.)

We have showed 3-dimensional morphology and chemical yields of silver dendrites generated by the liquid/solid redox reaction between silver ion and copper metal were remarkably affected by *vertical* high magnetic fields.[1)] In order to clarify the mechanisms, we have undertaken *in situ* observation of the silver dendrite formation reaction in 2-dimensional system. A thin plate of zinc metal (0.1 mm × 20 mm × 5 mm) was sandwiched with two plastic plates (2 mm × 20 mm × 55 mm), and silver nitrate aqueous solution was added to the space between two plates. At zero field, dendrites on the upper side of the metal plate grew steadily and no convection of the solution was observed. At 15 T, the top of dendrites underwent precession with bottom fixed. This unique phenomenon indicates that the solution near the dendrites undergoes convection due to the Lorentz force on the flow of ions. Because of concentration gradient of silver ions near the reactive zone of dendrites, silver ions move to dendrite surface and Lorentz force affects the flow of silver ions, leading to the convection of the solution near dendrites. Since dendrites are composed of many small crystals, they are not rigid but flexible. Circular convection of the solution near the dendrites induces precession of the flexible dendrites. This means that Lorentz force is very important for the reaction where concentration gradient of ions is induced during the reaction.

Reference

1) A. Katsuki, I. Uechi and Y. Tanimoto, *Bull. Chem. Soc. Jpn.* **77**, 275–279 (2004).

IX-X-3 Formation of Protein Crystals (Orthorhombic Lysozyme) in a Pseudo-Microgravity Environment Obtained by a Superconducting Magnet

YIN, D. C.[1]; WAKAYAMA, N. I.[2]; HARATA, K.[3]; FUJIWARA, Masao; KIYOSHI, T.[2]; WADA, H.[2]; HUANG, W. D.[4]; TANIMOTO, Yoshifumi
([1]NIMS and Northwestern Polytechnical Univ., China; [2]NIMS; [3]AIST; [4]Northwestern Polytechnical Univ., China)

[*J. Cryst. Growth* **270**, 184–191 (2004)]

As one of the best candidates for simulating the microgravity conditions in space, low gravity environments provided by applying an upward magnetic force has been considered to grow protein crystals. Since 2002, the stable and long-time durable microgravity generated by a superconducting magnet has been available for protein crystal growth. In this paper, for the first time, we grew protein crystals (orthorhombic lysozyme crystals) at pseudo- microgravity. The present study showed that pseudo-microgravity improves the crystal quality effectively and reproducibly. The application of strong magnetic field also improves the crystal quality. Further verification of the combined effects of microgravity and magnetic field itself may lead to a more general means to grow high quality protein crystals.

IX-X-4 Magnetic Field Effects upon Macroscopic Plastic Deformation of Diamagnetic Single Crystals Containing Paramagnetic Impurity

DUNIN-BARKOVSKIY, L. R.; MORGUNOV, R. B.[1]; TANIMOTO, Yoshifumi
([1]IMS and ISSIP, Chernogolovka)

It is known that macroscopic magnetoplastic effects in inorganic crystals containing paramagnetic impurity are mainly caused by spin-dependent solid reactions in the system of crystal structure defects. In spite of wide interest to the topic, there is so long a lack of understanding of the mechanisms of such effects. In this work we studied magnetic field effects on plastic deformation of NaCl:Eu single crystals. The crystals were annealed at 770 K and quenched to room temperature. Then they were deformed at room temperature in the absence and presence of a magnetic field (15 T). The field affects the shape of stress-strain diagram, in particular decreases the yield stress by approximately 100%, as shown in Figure 1. Besides, partial or complete suppression of the drop deformation (*i.e.*, Portevin-Le Chaterlier effect), caused by dynamic interaction between movable dislocations and atoms of dissolved impurity, was observed for the first time.

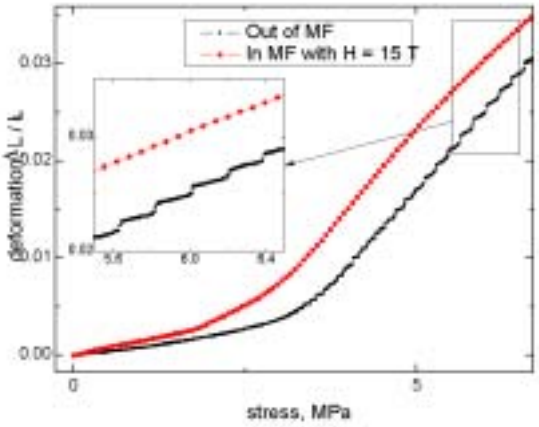

Figure 1. Magnetic field effects on stress-strain diagram of NaCl:Eu single crystal.

IX-X-5 Effect of Horizontal High Magnetic Field on the Movement of *E. coli*

TANIMOTO, Yoshifumi[1]; OGAWA, Seiji[2]; FUJITANI, Kiyomi[2]; FUJIWARA, Yoshihisa[2]; IZUMI, Shunsuke[2]; HIRATA, Toshifumi[2]
([1]IMS and Hiroshima Univ.; [2]Hiroshima Univ.)

[*Environ. Sci.* in press]

Effects of a high magnetic field gradient (8 T, *ca.* 400 T^2/m, horizontal) on the behavior of *E. coli* were examined. An *E. coli* suspended solution was injected in one end of a glass tube (5 mmϕ × 150 mm) filled with viscous medium containing sodium nitrate. They move along the tube axis because of chemotaxis to nitrate ion. The speeds for movement from a high (8 T) to a low field (1.5 T) and for the opposite movement are 1.35 and 0.49 cm/h, respectively; it is 0.65 cm/h at a zero field. It is found that the magnetic force hastens the downfield movement of *diamagnetic E. coli* and impedes the upfield movement.

IX-Y Theoretical and Computational Study on Gas Phase Reactions

1. Quantum chemical calculations are used to produce potential energy surface (PES) to do reaction dynamics simulations. We develop the methodology to generate PES efficiently and automatically using quantum chemical calculation results. The method does not need any derivative information in quantum chemical calculations.
2. We search a reasonable pathway to form H_2 and the other interstellar molecules *via* PAH related catalysts.
3. We also calculate (electronic) CD spectra to determine the absolute configuration of several chiral molecules in collaboration with experimentalists.

IX-Y-1 Aromatic Character of Annelated Dimethyldihydropyrenes

AIHARA, Jun-ichi[1]; ISHIDA, Toshimasa
([1]Shizuoka Univ.)

[*J. Phys. Org. Chem.* **17**, 393–398(2004)]

Aromaticity is one of the fascinating concepts in modern organic chemistry. It has been defined in structural, magnetic and energetic terms. Historically, many chemists have discussed aromaticity most conveniently in terms of ^{1}H chemical shifts. Mitchell and coworkers noted that ^{1}H chemical shifts of the internal methyl groups in dimethyldihydropyrene (DDP) and its annelated derivatives serve to assess the relative local aromaticities of the DDP nuclei. They recently estimated the order of aromaticity for DDP nuclei in annelated derivatives using nucleus-independent chemical shifts (NICS). We found that two graphtheoretically defined energetic quantities, percentage topological resonance energy (% TRE) and bond resonance energy (BRE), can be used to predict readily the relative aromaticities of these hydrocarbons and their DDP nuclei, respectively. Since these quantities are not dependent on the areas of individual rings, they are better suited for estimating the degree of aromaticity.

IX-Y-2 Possible Molecular Hydrogen Formation Mediated by the Inner and Outer Carbon Atoms of Typical PAH Cations

HIRAMA, Mutsumi[1]; ISHIDA, Toshimasa; AIHARA, Jun-ichi[1]
([1]Shizuoka Univ.)

[*Chem. Phys.* **305**, 307–316 (2004)]

We have been exploring the possibility of H_2 formation mediated by the radical cations of gaseous polycyclic aromatic hydrocarbons (PAHs). In this study, we estimated the catalytic ability of the inner carbon atoms of some typical PAH cations at the B3LYP/6-31G** level of theory and compared it with that of the outer carbon atoms. We presumed as before that H_2 is formed by way of two elementary reactions, the addition of an H atom to a PAH cation and the H abstraction from the resulting arenium ion by another H atom to yield H_2. We found that both reactions proceed without any activation energy. It follows that almost all carbon atoms of a PAH cation give sites for molecular hydrogen formation. Since there are large compact PAHs abundantly in space, the H_2 formation at the inner carbon atoms of such PAH cations can never be overlooked. Even if inner carbon atoms might be less reactive than peripheral ones, there are many inner carbon atoms in large compact PAH cations.

IX-Y-3 One-Pot Synthesis of Helical Aromatics: Stereoselectivity, Stability against Racemization, and Assignment of Absolute Configuration Assisted by Experimental and Theoretical Circular Dichroism

WATANABE, Masashi[1]; SUZUKI, Hiroshi[1]; TANAKA, Yasutaka; ISHIDA, Toshimasa; OSHIKAWA, Tatsuo[2]; TORII, Akiyoshi[3]
([1]Shizuoka Univ.; [2]Numazu College Tech.; [3]Saga Univ.)

[*J. Org. Chem.* in press]

Helical aromatics (**1**) were synthesized *via* one step in good quantity by solvent-free condensation of *N*,*N*'-*p*-phenylenediamine (**2**) and various carboxylic acids in the presence of Lewis acid. Microwave irradiation greatly facilitated the condensation reaction to furnish **1** with a 100% diastereo- and a 50% enantioselectivity, when a chiral carboxylic acid was utilized. **1f**, derived from 2-methylglutaric acid, was quite stable, no racemization taking place even at 200 °C. The assignment of the absolute configurations to the helical aromatics has been attempted by CD exciton chirality method and comparison of experimental and theoretical CD spectra calculated by time-dependent density functional theory.

IX-Y-4 A Local Interpolation Scheme Using No Derivatives in Potential Sampling: Application to OH + H_2 System

ISHIDA, Toshimasa; SCHATZ, George C.[1]
([1]Northwestern Univ.)

[in preparation]

We recently proposed a local interpolation scheme, in which interpolant moving least squares (IMLS) and the modified Shepard interpolation proposed by Collins are employed to describe potential energy surfaces. This IMLS/Shepard scheme is applicable to do potential interpolation with quantum chemical results for which analytical derivatives are not available. We applied the scheme to a four atomic system OH + H_2 → H_2O + H

reaction. As for the former system, we compared the results with those based on the modified Shepard interpolation using second order Taylor expansions. An analytical surface is used to define the potential function so that errors in the interpolation function may accurately be determined. We found that the energy and gradient errors in the present scheme is comparable to those in the modified Shepard scheme. Note that the present scheme does not utilize derivative and hessian information whereas the Shepard interpolation does. The accuracy in the IMLS/Shepard scheme is surprising, but can be explained by the more global nature of the interpolation.

IX-Y-5 Possible Interstellar Molecule Formations Mediated by Naphthalene Cation

HIRAMA, Mutsumi[1]; ISHIDA, Toshimasa; AIHARA, Jun-ichi[1]
([1]Shizuoka Univ.)

[in preparation]

We have studied the possibilities of interstellar molecule formation mediated by the radical cations in the gas phase. In this letter, we explored the catalytic role of a typical PAH cation, a naphthalene cation, at the both B3LYP/6-31G** and MP2/6-31G** levels of theory. We presumed that interstellar molecule is formed by way of two elementary reactions: the addition of an H atom to a PAH cation and the H abstraction from the resulting arenium ion by one interstellar molecular species to form another interstellar molecular species. It was found that the first reactions proceed with no activation energies. Refinement of the activation energies with both spin-projected and unrestricted MP2 procedures confirmed no or very small activation energies for the second reactions.

We employ the simplest PAH, a naphthalene, as molecular catalyst and consider that the naphthalenium ion is one of the key intermediates not only in the formation of molecular hydrogen but also in the formation of interstellar molecular species. We studied some formations of their species, *i.e.*, HCCH, CH_4, HCN, HNC, H_2O, NH_3, NH_2, CH_3, and CH_2. All of these species and these precursors have observed in space.

IX-Y-6 Molecular Rattles Using Excited States and Non-Adiabatic Transition

ISHIDA, Toshimasa; NANBU, Shinkoh; NAKAMURA, Hiroki

[in preparation]

Non-adiabatic phenomena play crucial roles in the molecular science, in particular, in the molecular material field. Nakamura and Nanbu proposed the idea for the molecular switching with aggressive use of the phenomena although the virtual system composed of an ideal one-dimensional finite periodic potential system was used. The key-phenomena in the idea are the complete reflection and complete transmission. Once we find the appropriate condition for those phenomena in the corresponding system, the molecular motion can be completely controlled without any exception.

We newly propose the application of our idea to the transmission of hydrogen atom through cyclic molecule. This may be regarded as a model of encapsulation by carbon nanotubes.

We explored lots of systems with theoretical calculations, and finally it is found that several model systems seem to be suitable. Two of them are (1) cyclopentadienyl radical (C_5H_5) + H reaction model and (2) C_9H_9 + alkaline atom system.

In these systems, we found complete transmission and reflection, which is based on two non-adiabatic transition of non-adiabatic tunneling type. We will discuss possible application to real systems.

IX-Y-7 Quantum Chemical Study of H_2 Formation Reaction *via* the Benzene Cation Catalyst

HIRAMA, Mutsumi[1]; AIHARA, Jun-ichi[1]; ISHIDA, Toshimasa
([1]Shizuoka Univ.)

[in preparation]

We have been exploring a possibility that polycyclic aromatic hydrocarbon (PAH) cations may catalyze the H_2 formation because PAHs are ubiquitous in interstellar space and are probably partly ionized by stellar UV radiation. Benzene is not a PAH, but is an aromatic hydrocarbon, so that it is expected to give similar energy profile to PAHs. Thus, we undertake to use benzene cations to investigate the effect of more sophisticated method for electron correlation on the energy profile of the H_2 formation reaction.

$C_6H_6^+ + H \rightarrow C_6H_7^+$
$C_6H_7^+ + H \rightarrow C_6H_6^+ + H_2$

We employed coupled cluster singles and doubles (CCSD) and its modification with the third order perturbation energy (CCSD(T)) as well as QCISD(T) at the MP2-optimized geometries to make comparison of the results with the B3LYP and MP2 ones to estimate higher correlation effects. In addition, use of both the B3LYP and MP2 results proposed by Turecek was valuated. CCSD, CCSD(T), and QCISD(T) calculations gave us activation energies between B3LYP and MP2 values. From these results, hybrid use of B3LYP and MP2 would be justified to estimate activation energies for larger PAH cation catalyst systems.

IX-Z Macromolecular Self-Assembly Opens the Way for Development of Novel Materials That Have Characteristics of Cellular Systems

Methods to integrate functional molecules into well-defined nano structures is a key for fabrication of future materials. Nano-integrated circuits may be afforded by elaborate arrangements of various molecular- and nano-devices. Self-assembly is a strong tool for integration of molecules into various nano structures. Self-assembly, however, tends to give polymorphism and structural defects in the assembled structures. Furthermore, functions of elaborate molecular systems should be sensitive to small structural damages and heat dissipation. For development of the future materials, thus, one should employ a self-assembly process that selectively affords a single, well-defined supramolecular structure to suppress polymorphism. It is also necessary that the formed device is repairable to be robust to damages and defects. We examine such a design strategy that has not yet been examined to date (Figure 1; see also Special Research Project (c)).

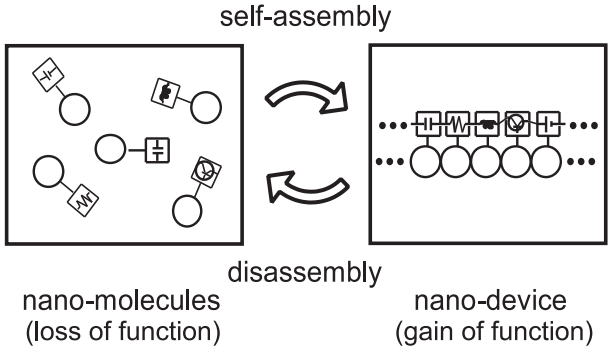

Figure 1. A concept of the nano-device that functions on-demand. The device does not function until on-demand self-assembly of nano functional blocks, and can easily be decomposed into the reusable components on demand.

IX-Z-1 Fabrication of Nano-Devices on the Principle of Cellular Supramolecular System

OBA, Toru; HANASAKI, Mitsuru[1]; SATO, Michihiro[1]; MINABE, Masahiro[1]
([1]Utsunomiya Univ.)

[*Photosynthesis: Fundamental Aspects to Global Perspectives* in press]

Development of molecular devices has attracted much attention in the field of electronics and photo-electronics. For global, sustainable development, molecular devices and nano-devices should be reusable, repairable, and bio-degradable, which has not been considered to date. We thus aimed at development of an artificial photosynthetic device as a prototype of the flexible (supra)molecular system that functioned on demand (Figure 1). We employed naturally occurring nano-tube, 'microtubule' (MT), to integrate functional molecules into a nano ordered structure. We prepared tubulins (Tubs), component proteins of MT, conjugated with a fluorophore for light-harvesting and with a photo-sensitizer-labeled hemoprotein for charge separation, respectively, and mixed them simply. Each time these functional blocks self-assembled to form MTs in the assembly/disassembly cycle, solar energy absorbed by the antenna fluorophore migrated to the sensitizer, leading to charge separation between the sensitizer and the heme. The nano-device can easily be decomposed into the components on demand, and the components can readily reassemble on demand to recover the function again.

IX-Z-2 Synthesis and Properties of Novel Cationic Chlorophyll Derivatives

OBA, Toru; TAKATOYA, Haruki[1]; TOBITA, Hiromi[1]; UGAJIN, Aya[1]; OGURA, Koji[1]; MINABE, Masahiro[1]
([1]Utsunomiya Univ.)

[*Photosynthesis: Fundamental Aspects to Global Perspectives* in press]

Not only metal nano particles but also biomolecules such as DNA, phospholipids, proteins and their supra-molecules have been studied for development of molecular devices. It is of much interest to conjugate chlorophylls (Chls), quite abundant photofunctional molecules in nature, with these biomolecules in water for fabrication of novel photofunctional materials such as artificial photosynthetic devices. Chl derivatives that carry cationic charges may be advantageous for interaction with anionic surfaces of the biomolecules and their supramolecules. The conjugation is, however, quite difficult, because, in general, Chls are insoluble in water, resulting in facile formation of higher aggregates. We prepared Chl derivatives that had cationic polymer moiety. Condensation of cationic polymer improved water-solubility, lowered the aggregation number, and enabled conjugation with proteins. The cationic, water-soluble Chl derivative is thus a useful tool for various investigations and applications.

IX-Z-3 Physicochemical Studies on the Molecular Mechanism of Photosynthesis

OBA, Toru; TAMIAKI, Hitoshi[1]
([1]Ritsumeikan Univ.)

[*Photosynthesis: Fundamental Aspects to Global Perspectives* in press]

Since chlorophylls (Chls) and bacteriochlorophylls (BChls) are highly asymmetric molecules, an external ligand can coordinate to the central Mg atom of (B)Chls from either of the two sides of the chlorin macrocycle. We found that the 'back' side (Figure 1) is favored for the ligand coordination, by survey of the highly resolved crystal structures of photosynthetic proteins and by theoretical calculations of model molecules. We have recently found that the 'back' type complex is also the major isomer in two newly resolved photosynthetic proteins. In light-harvesting complex II, 6 of 8 Chl *a* and 4 of 6 Chl *b* are the 'back'-type complexes, respectively. Among 28 ligand-identified Chls in the photosystem 2 core complex, 22 are the 'back' stereoisomers. Further calculations on the virtual chlorin molecules revealed the origin of the energy gap between the 'back' and the 'face' stereoisomers. We also discuss yet undetermined nomenclatures for the macrocycle faces of (B)Chls.

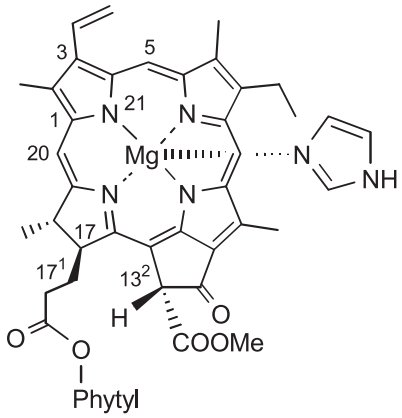

Figure 1. Molecular structure of the 'back' type chlorophyll *a*-imidazole complex.

Equipment Development Center

IX-AA Development of New Instrument

The technical staff of the Equipment Development Center is partly engaged in planning, researching, designing and constructing high technology experimental instruments in collaboration with the scientific staff. And these experimental instruments are incorporated with new manufacturing technology and new mechanical idea.

IX-AA-1 Development of a High-Precision Slit for Soft-X-Ray Emission Studies

MATSUSHITA, Koji[1]; YOSHIDA, Hisashi; SUZUI, Mitsukazu; HORIGOME, Toshio; HATSUI, Takaki; KOSUGI, Nobuhiro
([1]IMS and Nagoya Univ.)

An exit-slit system for the soft x-ray emission end station of the BL3U beamline has been developed. The slit comprises a set of two high-precision blades manufactured by using Electrolytic in-process dressing (ELID) grinding in collaboration with Nagoya University. The slit opening is adjustable from 5 to 100 micron by moving one of the blades in the direction perpendicular to the edge of the blades. The blade is connected to a piezo actuator *via* a solid metal flexure with a magnification of approximately 10. The blade (and the slit opening) is feedback controlled by a position stabilization system equipped with a capacitance-based sensor, which monitors the slit opening. The whole system has been constructed and is now under fine adjustment of the feedback control.

The slit system will be installed in August 2004, and be used in combination with the novel soft-x-ray emission spectrometer constructed by the department of vacuum UV photoscience.

IX-AA-2 Design and Fabrication of Undulator Beamline for STM Observations of Synchrotron Radiation Stimulated Reactions

MATSUSHITA, Koji[1]; SUZUI, Mitsukazu; NONOGAKI, Youichi; URISU, Tsuneo
([1]IMS and Nagoya Univ.)

The undulator beamline of BL7U at UVSOR was designed and fabricated for Chemical Dynamics Division in Department of Vacuum UV Photoscience. In the BL7U, the undulator radiation were focused by two Pt-coated cylindrical mirrors on the sample surface in the STM chamber set at end station of this beamline. The first mirror was located at 5100 mm downstream from the middle of the undulator. This mirror can move linearly by ±15 mm to adjust optical path. The second mirror was located at 2000 mm downstream from the first mirror. This mirror can move linearly by ±15 mm to the surface normal direction and rotates around both two axes of the vertical and horizontal directions by ±2°, to adjust the spot position on the sample surface.

The ideal design of the two rotating axes is that they are just on the mirror plane for easy beam positioning. However, horizontal rotating axis should be located far from mirror surface by the size of rotating mechanism, because rotating mechanism interfere the optical path. By using elastic hinges that have smaller size than ball bearings, we realized the small gap of ~4 mm between the mirror surface and the rotating axis in this system.

The beam positioning system and other beamline components have been constructed at UVSOR BL7U and used for synchrotron irradiation study.

UVSOR Facility

IX-BB Development of the UVSOR Light Source

IX-BB-1 Successful Commissioning of UVSOR-II

KATOH, Masahiro; HOSAKA, Masahito; MOCHIHASHI, Akira; YAMAZAKI, Jun-ichiro; HAYASHI, Kenji; HORI, Yo-ichiro[1]; HONDA, Toru[1]; HAGA, Kai-ichi[1]; TAKASHIMA, Yoshifumi[2]; KOSEKI, Tadashi[3]; KODA, Shigeru[4]; KITAMURA, Hideo[5]; HARA, Toru[5]; TANAKA, Takashi[5]
([1]KEK-PF; [2]Nagoya Univ.; [3]RIKEN; [4]Kyushuu Sync. L. R. C.; [5]RIKEN/SPring-8)

In 2003, UVSOR was successfully converted to a high brilliance synchrotron light source, UVSOR-II, which has eight straight sections and small emittance of 27 nm-rad. All the reconstruction works were completed within three months, from April to June 2003. The commissioning and the machine tuning were completed until the end of August. User experiments were started in September. The filling beam current is 350 mA. The light source is operated for 12 hours a day with an injection interval of 6 hours. Although a small beam emittance of 27 nm-rad was achieved in the machine studies, the light source is currently operated for users with a moderately small emittance of 60 nm-rad, which gives a longer beam lifetime. The low emittance operation for users will be started after the reinforcement of the RF accelerating system, which is planned in spring, 2005.

IX-BB-2 Commissioning of In-Vacuum Undulator for BL3U

MOCHIHASHI, Akira; KATOH, Masahiro; HOSAKA, Masahito; YAMAZAKI, Jun-ichiro; HAYASHI, Kenji; HORI, Yo-ichiro[1]; HONDA, Toru[1]; HAGA, Kai-ichi[1]; TAKASHIMA, Yoshifumi[2]; KOSEKI, Tadashi[3]; KITAMURA, Hideo[4]; HARA, Toru[4]; TANAKA, Takashi[4]
([1]KEK-PF; [2]Nagoya Univ.; [3]RIKEN; [4]RIKEN/SPring-8)

During the construction of UVSOR-II, an in-vacuum undulator was installed, whose period length was 38 mm and the number of the periods was 50. This undulator provides high brilliance soft X-rays to the newly constructed beam-line, BL3U. In the machine studies, it was confirmed that the storage ring could be operated with the small pole gap of 15 mm without reducing the beam lifetime. No beam instabilities, such as the resistive wall instability, were observed. The newly developed control system can correct the electron orbit shift due to the pole gap changes with a precision better than 10 microns. The users can change the pole gap and the photon energy at their experimental station anytime.

IX-BB-3 UVSOR Free Electron Laser

HOSAKA, Masahito; KATOH, Masahiro; MOCHIHASHI, Akira; YAMAZAKI, Jun-ichiro; HAYASHI, Kenji; TAKASHIMA, Yoshifumi[1]; HAMA, Hiroyuki[2]
([1]Nagoya Univ.; [2]Tohoku Univ.)

The upgrade of UVSOR increased the brightness of the electron beam. The improved quality of the beam is of great advantage to the storage ring FEL. We expect increase of the FEL gain by about one order with the present FEL system. In December, 2003, we have succeeded in oscillating the FEL for the first time after the upgrade. We confirmed the increase of the FEL gain. To improve the performance of the FEL further and deliver shorter wavelength laser to user, we are designing a new FEL system, which includes a new in-vacuum optical klystron type undulator optimized to lasing in the deep UV and VUV region.

IX-CC Researches by the Use of UVSOR

IX-CC-1 Autoionization Selectivity of Ne^+ Rydberg States Converging to $Ne^{2+}(^1S^e)$

HIKOSAKA, Yasumasa; AOTO, Tomohiro[1]; SHIGEMASA, Eiji; ITO, Kenji[1]
([1]KEK)

[*J. Phys. B* **37**, 2823 (2004)]

Indirect double photoionization processes of Ne have been studied in the photon energy range from 65.5 to 68.3 eV by using a threshold-photoelectron-photoelectron coincidence method, where intermediately-formed Ne^+ states have been defined by the detection of threshold photoelectrons and fast electrons from their autoionizing decay have been analyzed in coincidence. The present investigation revealed that each Ne^+ Rydberg series converging to $Ne^{2+}(^1S^e)$ shows notable selectivity in the autoionizing decay to the final Ne^{2+} states.

IX-CC-2 Dissociative Double Photoionisation of CO below the CO^{++} Threshold

HIKOSAKA, Yasumasa; ELAND, John[1]
([1]Phys. Theor. Chem. Laboratory)

[*Chem. Phys.* **299**, 147 (2004)]

Dissociative double photoionisation of CO below the adiabatic double ionisation threshold has been studied by the time-of-flight photoelectron-photoelectron coincidence (TOF-PEPECO) and the velocity imaging photoionisation coincidence (VIPCO) methods. By combining the results from the two methods which give complementary information, the double photoionisation process is identified to $CO + h\nu \rightarrow CO^{+}* + e^{-} \rightarrow C^{+}(^{2}P) + [O^{+}(^{2}D/^{2}P)]nl + e^{-} \rightarrow C^{+}(^{2}P) + O^{+}(^{4}S) + 2e^{-}$. The high energy resolution of the TOF-PEPECO spectrometer enables us to resolve individual fragment $[O^{+}(^{2}D/^{2}P)]nl$ states and also intermediate $CO^{+}*$ states. The angular correlations between electrons and ions, deduced from the VIPCO data, imply that the nuclear dissociation is faster or at least comparable in the time scale with molecular rotation, and that the second electron emission occurs after the C^{+} and O* atoms are far apart. A possible generic identification of the intermediate states is suggested.

IX-CC-3 Sub-Natural Linewidth Auger Electron Spectroscopy of the 2s Hole Decay in H_2S

HIKOSAKA, Yasumasa; LABLANQUIE, Pascal[1]; PENENT, Francis[2]; LAMBOURNE, Joe[2]; HALL, Richard[2]; AOTO, tomohiro[3,4]; ITO, kenji[3]
([1]Univ. Paris Sud; [2]Univ. Pierre Marie Curie; [3]Univ. Tsukuba; [4]KEK)

[*J. Electron Spectrosc. Relat. Phenom.* **137**, 287 (2004)]

Threshold photoelectron-Auger electron coincidence spectroscopy has been applied to the sulphur 2s region of H_2S, where the Auger electron spectrum is measured in coincidence with threshold electrons. Formation of $H_2S^{++}[(S2p)^{-1}(V)^{-1}]$ states *via* the $L_1L_{2,3}V$ Coster-Kronig transitions is observed above the S 2s photoionization threshold. Even below threshold, formation of these H_2S^{++} states is seen and is due to direct double ionization. A sub-natural linewidth regime is achieved with this coincidence method and three structures resulting from overlaps of the H_2S^{++} $[(S2p)^{-1}(V)^{-1}]$ states appear in the spectra. The three structures probably correspond to H_2S^{++} states with the $2b_1$, $5a_1$ and $2b_2$ holes.

IX-CC-4 Formation of Fluorescent and Metastable Fragments by Photoexcitation of Some Diatomic Molecules in the Vacuum Ultraviolet Region

HIKOSAKA, Yasumasa; LABLANQUIE, Pascal[1]; AHMAD, Muthanna[2]; PENENT, Francis[2]; ELAND, John[3]; HALL, Richard[2]
([1]Univ. Paris Sud; [2]Univ. Pierre Marie Curie; [3]Phys. Theor. Chem. Laboratory)

[*J. Phys. B* **37**, 283 (2004)]

The formation of fluorescent and metastable fragments from four diatomic molecules, *i.e.* O_2, N_2, NO and CO, has been investigated in the vacuum ultraviolet region. The neutral particles are detected by using a microchannel plate stack, where retarding electric potentials prevent charged particles from reaching the detector. Every diatomic molecule investigated here shows formation of fluorescent and metastable fragments in particular photon energy regions. Three Rydberg states of O_2 converging to $O_2^{+}(a^{4}\Pi_u)$ undergo both neutral dissociation processes forming fluorescent $[O^{+}(^{4}S)]3s\ ^{3}S_1$ and metastable $[O^{+}(^{4}S)]3s\ ^{5}S_2$, the yield curve for each fragment is determined. Direct and cascade formation of the fluorescent $[N^{+}(^{3}P)]3s\ ^{4}P$ fragment from N_2 are separated, and it is found that the dissociation of the 4sσ Rydberg state converging to $N_2^{+}(C^{2}\Sigma_u^{+})$ preferably produces $[N^{+}(^{3}P)]3p$ fragments, but not or weakly the $[N^{+}(^{3}P)]3s\ ^{4}P$ fragment. High-*n* Rydberg states converging to NO+($c^{3}\Pi$) and $CO^{+}(D^{2}\Pi)$ undergo neutral dissociation described by the core ion model, resulting in large peaks for neutral particle formation.

IX-CC-5 New Molecular Inner-Shell Spectroscopy for Probing Multiple Excitations

SHIGEMASA, Eiji; NAKAMURA, Eiken; GEJO, Tatsuo[1]
([1]Himeji Inst. Tech.)

[*AIP Conf. Proc.* **705**, 1118 (2004)]

A new experimental setup for probing multi-electron processes in molecular inner-shell ionization regions has been developed at the UVSOR facility, IMS. A zero-kinetic-energy electron (ZEKE) analyzer is composed of a lens system on the basis of the penetrating field technique and an electrostatic analyzer. Two identical ion detectors with regarding grids are utilized for detecting the fragment-ions emitted at 0 and 90 degrees relative to the electric vector of the light, which correspond to the symmetry-resolved photoabsorption spectra. The symmetry-resolved ZEKE spectra have been measured by scanning the photon energy with monitoring the intensity of the coincidence signals between the ZEKE electrons and fragment-ions. The results obtained using the new setup are reported.

IX-CC-6 Optical Conductivity of a Non-Fermi-Liquid Material $YbRh_2Si_2$

KIMURA, Shin-ichi; NISHI, Tatsuhiko[1]; SICHELSHMIDT, Joerg[2]; VOEVODIN, Vladimir[2]; FESTEL, Jung[2]; GEIBEL, Charls[2]; STEGLICH, Frank[2]
([1]GUAS; [2]Max-Planck-Inst. Chem. Phys. Stoffe, Germany)

[*J. Magn. Magn. Mater.* **272-276**, 36–37 (2004)]

The temperature-dependent electronic structure of a pronounced non-Fermi-liquid material $YbRh_2Si_2$ has been investigated by the optical conductivity measurement in the photon energy range of 10 meV–30 eV at several temperatures of 2.7–300 K: The optical conductivity spectrum as well as the electronic structure changes at two temperatures of 80 and 20 K: At 80 K;

the heavy quasiparticles develop and at 20 K; the non-Fermi liquid behavior appears in the optical conductivity spectra.

IX-CC-7 New Infrared and Terahertz Beamline BL6B at UVSOR

KIMURA, Shin-ichi; NAKAMURA, Eiken; YAMAZAKI, Jun-ichiro; KATOH, Masahiro; NISHI, Tatsuhiko[1]; OKAMURA, Hidekazu[2]; MATSUNAMI, Masaharu[2]; CHEN, Lin[2]; NANBA, Takao[2]
([1]GUAS; [2]Kobe Univ.)

[*AIP Conf. Proc.* **705**, 416–419 (2004)]

We have designed a new infrared beam line BL6B at UVSOR for infrared and terahertz spectroscopies including microspectroscopy with high brilliance and high flux. The beam line will be replaced in the spring of 2004 from the infrared beam line, BL6A1, at UVSOR. The beam line has a large acceptance angle of 215(H) × 80(V) mrad^2 and a so-called "magic mirror" is adopted to get the perfect focusing of the bending magnet radiation. The optics and expected performance (focus size, photon flux and brilliance) are reported.

IX-CC-8 Change of Electronic Structure Induced by Magnetic Transitions in CeBi

KIMURA, Shin-ichi; OKUNO, Mitsuru[1]; KITAZAWA, Hideaki[2]; ISHIYAMA, Fumihiko[3]; SAKAI, Osamu[4]
([1]Kobe Univ.; [2]Natl. Inst. Mater. Sci.; [3]NTT; [4]Tokyo Metropolitan Univ.)

[*J. Phys. Soc. Jpn.* **73**, 2041–2044 (2004)]

The temperature dependence of the electronic structure of CeBi arising from two types of antiferromagnetic transitions based on optical conductivity was observed. The optical conductivity spectrum continuously and discontinuously changes at 25 and 11 K, respectively. Between these temperatures, two peaks in the spectrum rapidly shift to the opposite energy sides as the temperature changes. Through a comparison with the band calculation as well as with the theoretical optical conductivity spectrum, this peak shift was explained by the energy shift of the Bi 6p band due to the mixing effect between the Ce 4f Γ_8 and Bi 6p states. The single-layer antiferromagnetic transition from the paramagnetic state was concluded to be of the second order. The marked changes in the optical conductivity spectrum at 11 K, however, indicated the change in the electronic structure was due to a first-order-like magnetic transition from a single-layer to a double-layer antiferromagnetic phase.

IX-CC-9 Para- to Antiferro-Magnetic Phase Transition of CeSb Studied by Ultrahigh-Resolution Angle-Resolved Photoemission Spectroscopy

ITO, Takahiro; KIMURA, Shin-ichi; KITAZAWA, Hideaki[1]
([1]Natl. Inst. Mater. Sci.)

Temperature-dependent angle-resolved photoemission spectroscopy has been performed on CeSb to study the origin of its complicated magnetic phase transition. In the paramagnetic phase ($T \geq 30$ K), we have found that the electronic structure near the Fermi level (E_F) consists of the hole-like Sb 5p band at the Γ point and the electron-like Ce 5d bands at the X point. With decreasing temperature across Néel temperature (T_N = 10 K), both the energy shift and the energy splitting of the bands appear along the ΓX high-symmetry line. While the energy shift of the bands is consistent with the pf mixing model, the energy splitting has not been expected in the model so far. On the other hand, by comparing with the recent calculation based on the pf+dp mixing model, we found a qualitative agreement between the experiment and the calculation. This result suggests the importance of the dp mixing effect to interpret the mechanism of the magnetic phase transition of CeSb.

IX-CC-10 Optical Study on *c-f* Hybridization States in Mixed-Valent Yb Compounds: Metallic $YbAl_3$ *vs* Semiconducting YbB_{12}

OKAMURA, Hidekazu[1]; MICHIZAWA, Takahiro[1]; MATSUNAMI, Masaharu[1]; NANBA, Takao[1]; KIMURA, Shin-ichi; EBIHARA, Takao[2]; IGA, Fumitoshi[3]; TAKABATAKE, Toshiro[3]
([1]Kobe Univ.; [2]Shizuoka Univ.; [3]Hiroshima Univ.)

[*J. Magn. Magn. Mater.* **272-276**, e51–e52 (2004)]

We have measured the optical conductivity spectra of YbB_{12} and $YbAl_3$; which are typical mixed-valent Yb compounds. The measured optical conductivity spectra in the mid-infrared region are quite similar for the two compounds, with a pronounced peak centered near 0.2 eV: This result demonstrates that the Kondo semiconductor YbB_{12} and the highly metallic $YbAl_3$ share very similar electronic structures near the Fermi level, in spite of their very different transport properties at low temperatures. This observation is discussed in terms of *c–f* hybridization states in these compounds.

IX-CC-11 The Origin of the Phase Separation in Partially Deuterated κ-$(ET)_2Cu[N(CN)_2]Br$ Studied by Infrared Magneto-Optical Imaging Spectroscopy

NISHI, Tatsuhiko[1]; KIMURA, Shin-ichi; TAKAHASHI, Toshiharu[2]; ITO, Takahiro; IM, Hojun; KWON, Yong-seung; MIYAGAWA, Kazuya[3]; TANIGUCHI, Hiromi[4]; KAWAMOTO, Atsushi[5]; KANODA, Kazushi[3]
([1]GUAS; [2]Kyoto Univ.; [3]Univ. Tokyo; [4]Saitama Univ.; [5]Hokkaido Univ.)

The direct observation of the phase separation between the metallic and insulating states of 75%-deuterated κ-$(ET)_2Cu[N(CN)_2]Br$ (d33) using infrared magneto-optical imaging spectroscopy is reported, as

well as the associated temperature, cooling rate, and magnetic field dependencies of the separation. The distribution of the center of spectral weight (<ω>) of d33 did not change under any of the conditions in which data were taken and was wider than that of the non-deuterated material. This result indicates that the inhomogenity of the sample itself is important as part of the origin of the metal - insulator phase separation.

IX-CC-12 Auger Electron Spectroscopy in Coincidence with Photoelectrons

ITO, Kenji; HIKOSAKA, Yasumasa; SHIGEMASA, Eiji

We have developed Auger-photoelectron coincidence spectroscopy, which involves measuring Auger electrons in coincidence with corresponding photoelectrons, to elucidate the decay dynamics of the inner-shell hole states followed by the production of doubly charged atomic and molecular ions. Two analyzers for the Auger electrons and photoelectrons have been installed in a vacuum chamber, and we have successfully obtained the first coincidence spectrum for OCS at BL4B in spring 2004. In our experiment, we measure threshold photoelectrons as photoelectrons to attain high detection efficiency. Tuning photon energy at the S 2s ionization threshold, the Auger electron spectra are recorded in coincidence with the threshold photoelectrons. We have observed the Auger lines associated with the formation of $OCS^{++}[(S\ 2p)^{-1}(V)^{-1}]$ states *via* the $L_1L_{2,3}V$ Coster-Kronig transitions, which are rather faster than usual Auger decay processes such as the *LVV* transitions. The corresponding Auger spectra measured in the ordinary way show broad structures due to the lifetime effect of the 2s hole states, however, at least five peaks can be observed in the coincidence spectra where the experimental resolution is restricted only by the instrumental resolution.